Ultrafast Dynamics of Excited States of Molecules and Clusters

by

Lauren Frances Heald

A Dissertation Presented in Partial Fulfillment
of the Requirements for the Degree
Doctor of Philosophy

Approved September 2022 by the
Graduate Supervisory Committee:

Scott G. Sayres, Chair
Dong-Kyun Seo
Vladimiro Mujica

ARIZONA STATE UNIVERSITY

December 2022

ABSTRACT

The movement of energy within a material is at the heart of numerous fundamental properties of chemistry and physics. Studying the process of photo-absorption in real time provides key insights into how energy is captured, stabilized, and dissipated within a material. The work presented in this thesis uses ultrafast time-of-flight mass spectrometry and computational modeling to observe and understand the properties of photo-excited states within molecules and clusters. Experimental results provide direct measurement of excited state lifetimes, while computational modeling provides a more thorough understanding of the movement of energy within an excited state.

Excited state dynamics in covalent molecules such as n-butyl bromide (C_4H_9Br), presented in Chapter 4, demonstrate the significance of IVR of photo-excited states. Exciting to the high energy Rydberg manifold leads to predissociation into fragments of various lengths and degrees of saturation but the predissociation process is disrupted by energy redistribution into hot vibrational states. Experimental lifetimes show that IVR occurs over rapidly (~ 600 fs) leaving less energy for bond dissociation. Additionally, a long-lived feature in the dynamics of $C_4H_9^+$ shows evidence of ion-pair formation – a known phenomenon which creates a stable A^+/B^- pair separated by several angstroms and occurring at energies lower than direct ionization. The results of this research show the dynamics of energy transfer into bond fragmentation, kinetic energy, and vibrational motion.

Metal-oxide clusters are unique materials which are representative of bulk materials but with quantized excited states instead of bands and as such can be used as

atomically precise analogs to semiconducting materials. Excited state lifetimes and theoretical descriptors of electron-hole interactions of titanium oxide clusters, presented in Chapter 5, shows the significance of structure and oxidation of charge-transfer materials. Modeling the excited states of the photo-generated electrons and holes provides a window into the dynamics of charge-transfer and electron-hole separation and recombination in bulk materials. Furthermore, changes in the oxidation of the cluster have a dramatic impact on the nature of excited states and overall cluster properties. Such changes are analogous to oxygen defects in bulk materials and are critical for understanding reaction chemistry at defect sites.

To my family and friends.

"No matter how to get there or where you end up, human beings have this miraculous gift of making that place their home."

- Creed Bratton, The Office

ACKNOWLEDGMENTS

There is no accomplishment that is achieved in a vacuum and my success is no different. There are so many people I owe this achievement to, many of whom will not be named specifically but generally I'd like to acknowledge all of my incredible family members, friends, and colleagues. More specifically, first and foremost, I'd like to acknowledge my wonderful, supportive, and loving family. My parents, Randy and Ellen, have been in my cheering section for the 28 years I have spent on earth and their support cannot be overstated. It is easy to be there to celebrate the good times, but my parents have stood the test of time and hardship by my side through the best of the best and hardest of the hard. I could not ask for more from my wonderful, inspiring, and loving parents. I could not have done this without you and everything I do from here on will also be because of the amazing example you have set and the endless love you have given. They have also raised a funny, intelligent, kind, and indescribably great son, my brother Spencer, who has been my best friend from the get-go. Spencer has always been someone who has encouraged and driven me to become my best self, just as I have tried to encourage him to do the same. Without the three of them, I would not be where I am today and for that I am eternally grateful. I also want to dedicate this to my grandma, Carol Heald, whom I lost during my PhD, and whom I know would be so proud of me. I wish I could share this with her, and she will never be forgotten.

I would also like to acknowledge all of the friends who have been by my side throughout this process. Over the years I have been lucky to meet such incredible people during my academic career. Jordyn Robare is the best friend I have ever had, and she has

been with me in this experience keeping me happy and stable and at home. Jordyn, you are an inspiration to me, and I know we will be friends for life. I would also like to acknowledge Edgar Reyes Cruz. We started our PhDs together and he was the first person to really make me feel comfortable. Finally, I would like to acknowledge John Vant, who has been accepting, kind, and has allowed me to be fully myself with from the first time I met him. These three are irreplaceable and I hope, more than anything, that I have been able to show them the support during their studies that they have shown me. I never expected to come to ASU and meet people who I know will be in my life forever. I cannot thank you all enough.

I would also like to acknowledge the entire Sayres lab. Jake Garcia and I started this journey as Scott's first students together and there is no one else I would've rather shared that experience with. Over the years, I have been lucky enough to have an advisor, Scott Sayres, who has given me endless support and tireless guidance. During my time in the group, I have also been able to oversee the undergraduate and graduate work of numerous people, many of whom have gone on to pursue their own educational aspirations. Their dedication and hard work has allowed me to accomplish all the work presented in this thesis.

This time in my life has been one of the most difficult periods, and it is only through the love and support of these and many other people that I have been able to get to where I am. There are not enough words available to fully explain the magnitude of their role in my life. More than anything, I'd like to say thank you to everyone who has been with me through this process. You are the reason I'm here.

TABLE OF CONTENTS

Page

CHAPTER Page

APPENDIX

LIST OF TABLES

LIST OF FIGURES

Figure Page

Figure Page

Figure Page

Figure Page

Figure Page

Figure Page

Figure Page

CHAPTER 1

INTRODUCTION

1.1 Molecular Dynamics in Real Time

At the heart of chemistry and physics is the behavior and dynamics of atoms and molecules in real time. The time scale of chemical systems varies by size and process: mechanical processes take milliseconds while electronic motion occurs within attoseconds (Figure 1.1). For example, one of the fastest molecular motion, the vibrational period of H_2, is 8 femtoseconds (fs) (1 fs = 10^{-15} seconds).[1] Larger molecules and clusters have much longer vibrational and geometric rearrangement time frames which can be estimated given the terminal velocity of atomic separation is ~ 0.01 Å fs^{-1}.[2] Thus, given the known motion of a vibrational bond, the lifetime can be estimated to tens to hundreds of fs. The advent of Femtochemistry is generally attributed to the work of Ahmed Zewail, winner of the 1999 Nobel Prize in Chemistry, who coined the term and defined it as the field of chemistry directly concerned with making and breaking of chemical bonds.[3] Since the pioneering work of Zewail and the development of ultrashort laser pulses, it is now possible to study molecular motions, such as vibrational motion, in real time. These studies have proven to be key to understanding fundamental molecular mechanisms such as bond formation, bond dissociation, charge carrier formation and relaxation, and structural deformation. Each of these processes can be initiated via photon absorption from a ground state (pump photon) into some electronically excited state. These states can then be probed with a second photon which enables collecting information about the molecular response to the pump beam (termed pump-probe

spectroscopy). These states then relax via numerous pathways inducing chemical change. Observing these processes through real time spectroscopy and understanding them using ab initio quantum mechanical modeling provides key insights into the chemical processes fundamental to nature and technology.

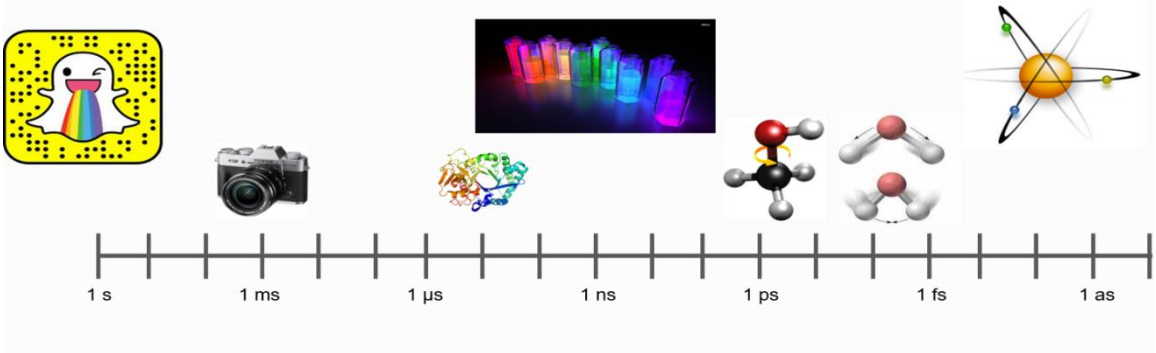

Figure 1.1 Pictorial Representation of Lifetimes of Key Chemical Processes. From Left to Right: Standard Imaging Mechanisms Occur over Seconds to Milliseconds; Protein Folding Occurs over Microseconds; Fluorescence and Phosphorescence Lasts over Nanoseconds; Bond Rotation Occurs over Picoseconds; Molecular Vibrations Have Periods of Femtosecond Duration; And Electronic Motion Occurs Within Attoseconds.

1.1.1 Interaction of Light and Matter

The research which comprises this thesis is focused on the fundamental nature of light and matter interaction. The use of ultrafast pump-probe spectroscopy allows for the observation of vibrational motion of molecules and clusters in real time as they respond to some perturbation. One such perturbation of interest is the light induced excitation of molecules from a ground state to an excited state. From an experimental perspective, perhaps the most fundamental equation of light-matter interactions is Beer's law which defines absorbance as

$$A = -\log\frac{I_0}{I} \tag{1.1}$$

where I_0 corresponds to the incoming intensity of light and I corresponds to the intensity after absorption from the sample. Another important principle in the preparation of an intermediate state from the absorption of light is the Franck-Condon (FC) Principle which states that, to a first approximation, an electronic transition occurs without changes of the molecular geometry, or that transitions occur vertically, without involving nuclear motion. Given this, the probability of vibrational transition from one energy level to another is directly correlated to the degree of overlap of the wavefunction of the vibrational levels.[4] From the FC principle, it is then possible to predict how vibrational energy levels are populated upon the absorption of a photon.

A second type of perturbation relevant to ultrafast light-matter interactions is photoionization. There are arguably three distinct types of photoionization: single (SPI) or multi-photon ionization (MPI), strong field ionization (SFI), and over-the-barrier ionization (Figure 1.2). Distinguishing these mechanisms can be thought of through the lens of the wave/particle duality of light. In the case of MPI, each photon is thought of as a discrete particle with a quantized energy and the rate (W_{MPI}) of ionization is directly proportional to the number of photons absorbed.

$$W_{MPI} = \sigma_N I^N \tag{1.2}$$

Here, σ_N is the ionization cross-section and I is the laser intensity raised to the number of photons, N.

In contrast to MPI and the concept of photons as particles, both SFI and over-the-barrier ionization are best understood when considering the wave nature of light. In each case, the electric field of the laser is strong enough to suppress the Coulomb barrier

holding the electron to the nucleus. In the case of over-the-barrier, the suppression is strong enough that there is no longer any effective Coulomb potential acting on the electron and ionization is spontaneous (i.e., instantaneous). In contrast, SFI is a probability-based mechanism which occurs when the Coulomb barrier is suppressed and the electron can tunnel away from the nucleus.

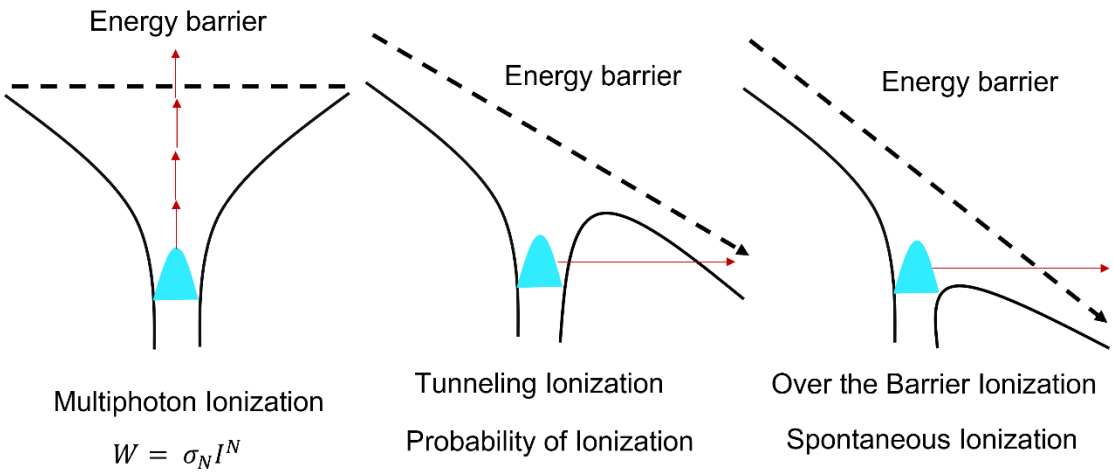

Figure 1.2 Representation of Types of Ionization and Their Interaction with the Energy Barrier Holding the Electron to the Nucleus.

In the 1964, Keldysh proposed a mathematical parameter (γ) for determining which type of ionization is occurring based on the intensity of the laser field and the ionization potential of the atom or molecule.[5] The Keldysh parameter is given by

$$\gamma = \frac{\omega}{F}\sqrt{2I_P} \tag{1.3}$$

where ω is the angular frequency of the laser, F is the amplitude of the electric field in atomic units, and I_P is the ionization potential of the system. Under the Keldysh approximation, when $\gamma >> 1$, MPI dominates and when $\gamma << 1$, SFI dominates. However, simply considering the ionization potential of an atom or molecule is not sufficient for understanding the mechanisms at work in SFI. Many theories have expanded on the

Keldysh theory including the work of Perelomov, Popov, and Terent'ev (PPT) who developed a quantitative method for predicting the rate of SFI for single atoms based on the Keldysh parameter.[6]

Following the work of PPT, Ammosov, Delone, and Krainov (ADK) expanded on the theory of tunneling ionization by incorporating the principal quantum numbers into the rate equation for modeling SFI. This theory is still heavily influenced by the ionization potential of the atom and the electric field of the laser, while taking into account the spatial overlap of the laser with the atomic orbital of interest.[7] The rate of tunneling ionization determined by ADK in a static electric field is given by

$$w_{ADK} = \frac{\kappa^2 [C_{n^* l} Q_{lm}]^2}{2^{|m|}(|m|)!} \left(\frac{2\kappa^3}{F}\right)^{2n^* - |m| - 1} e^{\frac{-2\kappa^3}{3F}} \tag{1.4}$$

where κ is equal $(2I_P)^{3/2}$, F is the intensity of the laser field, and $C_{n^* l}$ and Q_{lm} are coefficients related to the principal quantum numbers of the atomic orbital via

$$C_{n^* l} = \left(\frac{2e}{n^*}\right)^{n^*} \frac{1}{\sqrt{2\pi n^*}} \tag{1.5}$$

and

$$Q_{lm} = (-1)^{\frac{(m+|m|)}{2}} \sqrt{\frac{(2l+1)(l+|m|)!}{2(l-|m|)!}} \tag{1.6}$$

In these equations, l is the angular quantum number, m is its projection, n^* is the effective principal quantum number defined as Z/F_0 where Z is the charge after the electron departs, and e is a constant. In an intense laser field (> 10^{13} W/cm^2) the rate of tunneling occurs on the femtosecond to attosecond time scale demonstrating the need for ultrashort laser pulses (Figure 1.3).

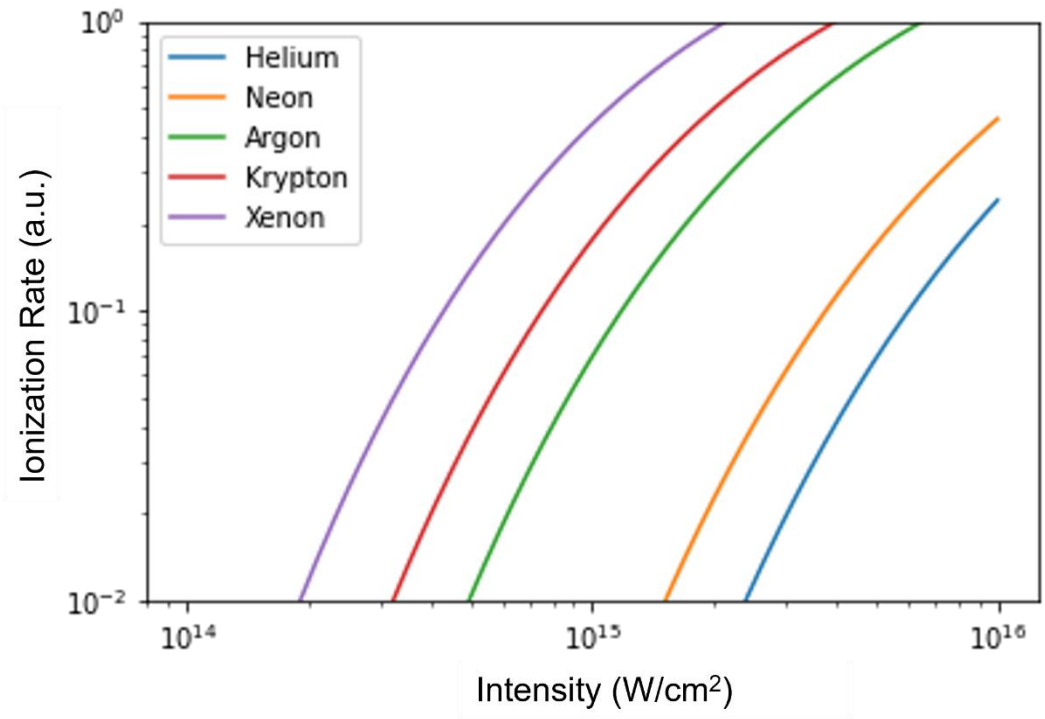

Figure 1.3 Ionization Rate of Nobel Gases in an Intense Electric Field as Determined by ADK. Note: 1 fs = 41 A.U.

From the ionization rate it is possible to also determine the probability of ionization based on the conditions of the laser. The probability depends on the rate as well as the pulse duration. The probability is calculated via

$$P = 1 - e^{\int_{-\infty}^{\infty} -W dt} \tag{1.7}$$

When assuming a square wave, the integral reduces to $W\tau$, where τ is the pulse duration of the laser. Rates and probabilities of tunneling ionization become particularly important when discussing the generation of high energy photons as described in Chapter 2.

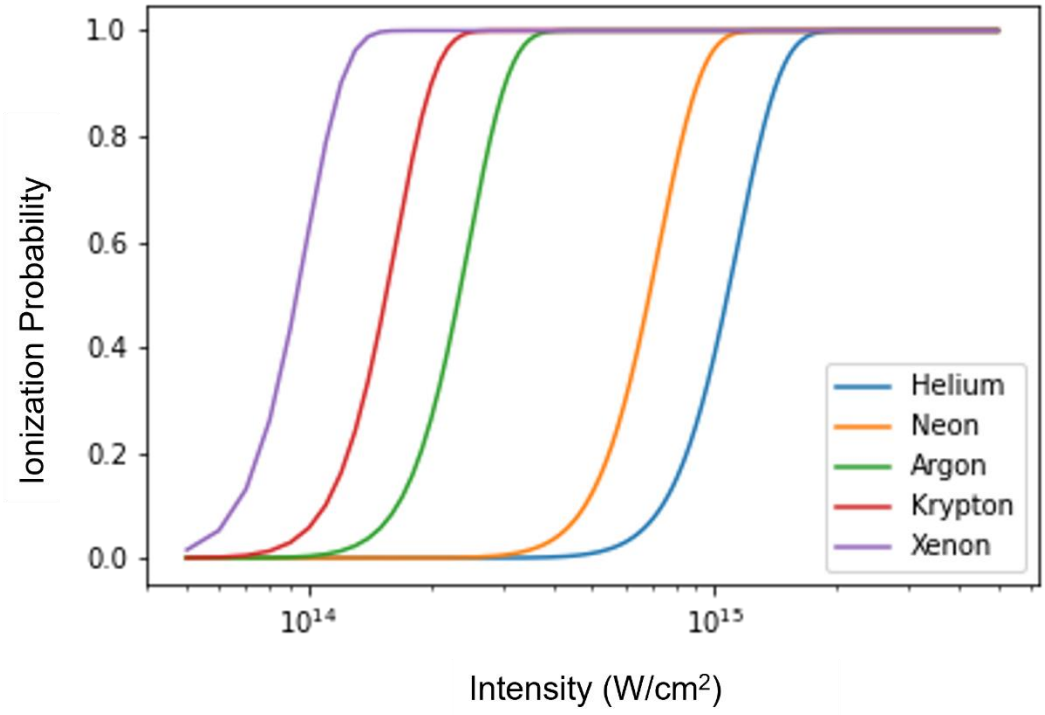

Figure 1.4 Ionization Probability Determined by ADK for Nobel Gases Using an 800 nm Laser with a 35 fs Pulse Duration.

Describing the dynamics of a photoexcited or photoionized system requires a detailed understanding of the nature of the light-matter interaction. This dissertation uses fundamental theories of light and matter to observe the evolution of a photoexcited molecule in the ultrafast regime.

1.1.2 Excited State Dynamics of Isolated Molecules

The research in this thesis focuses on observing and understanding the distribution, relaxation, and stabilization of energy absorbed via photoexcitation. The mechanisms involved in energy relaxation and redistribution are fundamental for a multitude of chemical and industrial processes critical for modern technology. Excited state dynamics of isolated molecules can be used as a window into photoinduced

unimolecular reactions which lead to bond dissociation and bond formation following energy absorption via laser excitation. An example of a photoinduced unimolecular process is given by

$$ABC \xrightarrow{h\upsilon} ABC^{*} \xrightarrow{\tau} [A \cdots BC]^{\ddagger *} \xrightarrow{\tau} A + BC \tag{1.8}$$

Here, general molecule *ABC* is excited with a photon of $E = h\upsilon$ to become *ABC** and over some lifetime (τ) the molecule undergoes dissociation. Femtosecond resolved spectroscopy allows for the direct observation of the transition state and the time scale of energy transfer into different degrees of freedom within the molecule. Within these unimolecular reactions, the reaction coordinate is considered the atomic separation of the involved species (i.e., $r_{A\text{-}B}$). The potential energy surface of the excited states with respect to internuclear distance can be modeled through *ab initio* software and used to further describe the photochemistry of importance. These potential energy surfaces can include dissociative, bound Rydberg wells, and ion-pair wells, each of which have their own equilibrium positions and reaction timescales (Figure 1.5).

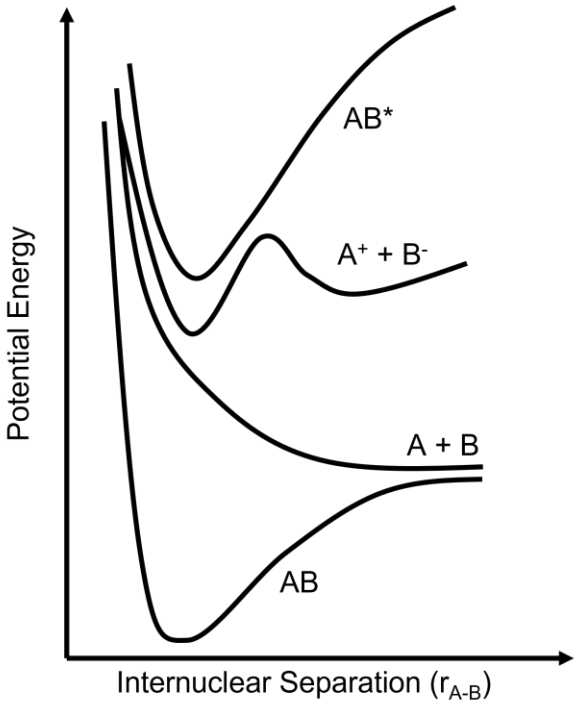

Figure 1.5 Example Potential Energy Surfaces of a Diatomic Molecule Showing a Dissociative State leading to A + B, an Ion-Pair State leading to $A^+ + B^-$, and a Bound Rydberg State leading to AB*.

With femtosecond resolution it is possible to observe the entire evolution of a photochemical process in which, at the onset of photoinduced excitation, or time zero, photon energy is transferred to the molecule via an ultrafast laser pulse. This energy is absorbed vertically (without molecular motion), and this proceeds through a variety of relaxation pathways relating to the potential energy surface of the excited state of the molecule. One key mechanism involved in excited state relaxation is intramolecular vibrational energy redistribution (IVR). This is the process through which vibrational energy of a single state is translated into vibrational energy of many states within the molecule. Within unimolecular chemistry (the dynamics of an isolated molecule), IVR is fundamental for understanding reaction pathways leading to both the breaking and

forming of chemical bonds. Mapping the energetic motion and distribution in excited states can be used to understand reaction mechanics in complex systems.

1.1.3 Excited State Dynamics of Metal Oxide Clusters

Evolving in size from single molecules to clusters changes the nature of excited states. Clusters are generally defined as a non-scalable regime where the addition or subtraction of a single atom can change the properties of the entire system. Clusters differ from bulk materials as their electrons belong to discrete molecular orbitals and not to energy bands which can be modeled with quantum mechanical computation.[9] Metal-oxide clusters are particularly interesting given their ability to act as atomically precise models of bulk semiconducting materials. The dynamics of the excited states can be studied with ultrafast spectroscopy and the properties of the clusters can be determined with atomic precision. Detailed analysis of the dynamics of photo-excited states of clusters provides insight into bulk properties of metal-oxide materials. The use of clusters as models for bulk properties such as defect sites sheds light on the chemistry relating to charge-carriers and overall reactivity of the bulk phase.

In metal-oxide clusters, changes in the overall oxidation of the cluster (accomplished through the addition or removal of a single oxygen atom) can dramatically change the properties of the cluster including geometry, excited state energies, and excited state dynamics. The effects of oxidation of metal-oxide clusters can be studied through the characteristics of the photoexcited state of the cluster. In these clusters, photoexcitation leads to increased electron density in a higher energy state and a reduction of electron density in the molecular ground state, thus creating an electron-hole

pair (Figure 1.6). The cluster then undergoes a molecular distortion to stabilize the electron and hole densities. This distortion, involving both charge redistribution and vibrational relaxation, can be interpreted in terms of quasi-particles, e.g. polarons and excitons, and is the result of the energetics of the electron, the hole, and the geometrical relaxation of the molecule. The relaxation and redistribution of the electron-hole pair directly determines the photochemistry of the molecule.

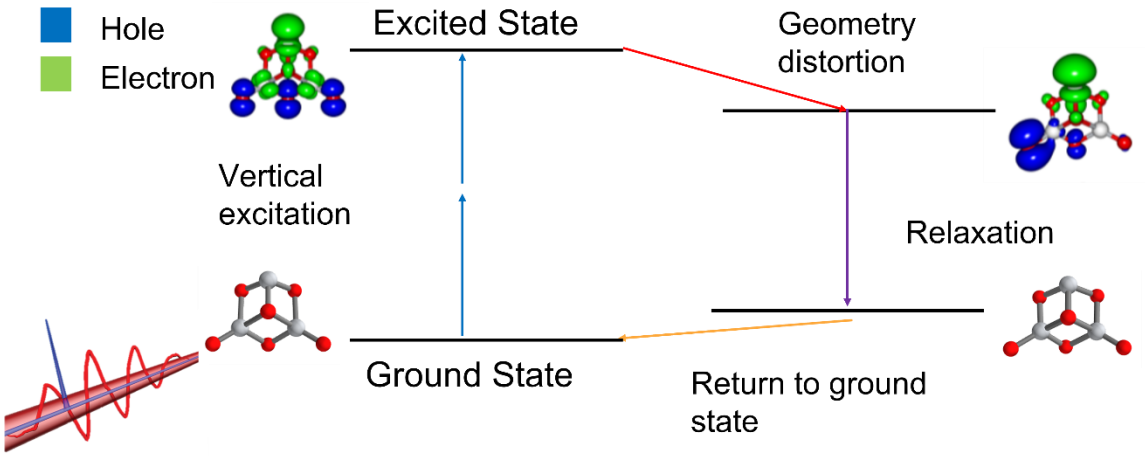

Figure 1.6 Basic Pathway of Excitation, Geometric Distortion, and Relaxation of a Photo-Excited Molecule. Here, Ti_3O_6 is Used as Prototypical Example. The Hole Density is Shown in Blue and the Electron Density is Shown in Green.

Reaction chemistry associated with photoexcitation is directly dependent on the lifetime of excited states as relaxation disrupts the molecule's ability to undergo energy transfer within and between systems. Studying the excited state dynamics of both molecules and clusters provides insights into unimolecular energy redistribution, bond fragmentation and formation, electron-hole recombination, and exciton and polaron formation.

1.2 Ultrafast Lasers and Instruments

For nearly 100 years, the theories of quantum mechanics have been accepted without the capabilities to observe in real time the motion of nuclei and electrons. The advent of chirped pulse amplification (CPA) for the generation of high power, fs laser pulses in the 1980s led to a revolution in ultrafast spectroscopy which continues to push the boundaries of time resolved experiments.[10,11] With few-femtosecond resolution it is possible to take spectra of molecules at individual points along their vibrational curves, where the nuclei are effectively frozen, and the electronic motion can be observed. At this timescale, it becomes possible to track key chemical processes such as chemical reactions, bond formations, and ionization. Using both time of flight mass spectroscopy and extreme ultraviolet (XUV) transient absorption spectroscopy, a full picture of the time-resolved motion of valence and core molecular orbitals can be studied.

1.2.1 Ultrafast Pump-Probe Spectroscopy

Numerous types of femtosecond spectroscopy exist for studying ultrafast processes, each with their own unique power and limitations. Popular methods include infrared (IR) spectroscopy, UV/Visible absorption spectroscopy, extreme ultraviolet (XUV) absorption spectroscopy, and hard X-ray diffraction spectroscopy. Figure 1.7 shows the different energy regions of the electromagnetic spectrum used in each of the previously listed techniques and the orbitals these techniques access. Research presented in this thesis uses time of flight mass spectrometry (TOF-MS) using UV and near-IR photons and XUV absorption spectroscopy. This dissertation will discuss the construction

and preliminary results of the XUV spectrometer as well as excited state dynamics determined using fs resolved TOF-MS.

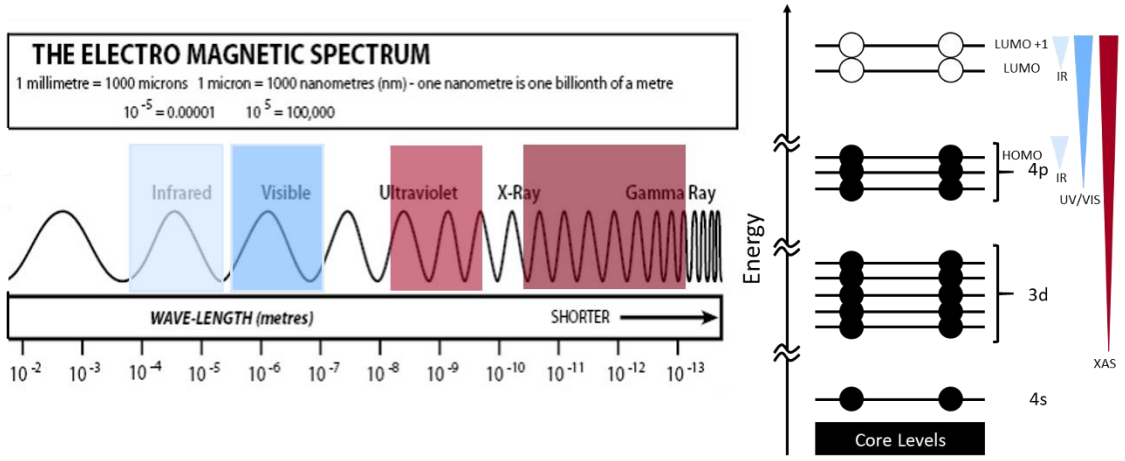

Figure 1.7 Correlation Between the Electromagnetic Spectrum and the Range of Probed Levels of an Atom or Molecule. Each Color Represents a Different Spectroscopic Technique with IR in Light Blue, UV/Visible in Darker Blue, XUV in Light Red, and X-Ray in Darker Red.

Pump-probe spectroscopy allows for the observation of the entire excited state evolution, from time zero (absorption of the pump photon), through some transition state, into a new product. This process can be observed in pump-probe spectroscopy as outlined in Figure 1.8 where the probe ionizes the excited molecule for detection in a mass spectrometer. The molecule can then undergo a variety of relaxation pathways including: internal conversion, defined as the electron transition between two excited states with the same spin; intersystem crossing, defined as the crossing between two excited states with different spins; IVR; and dissociation.

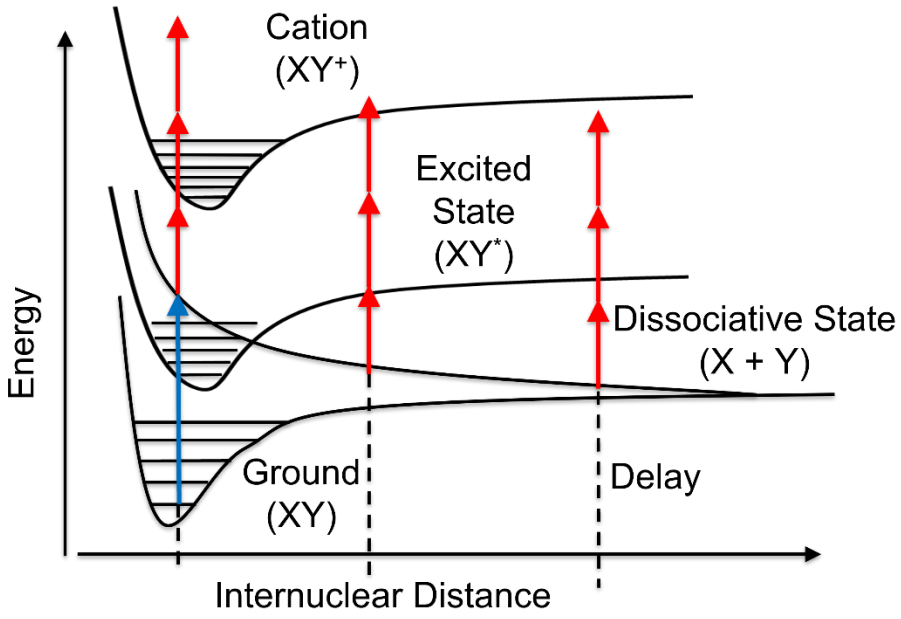

Figure 1.8 Schematic of the Pump-Probe Process for Tracking Excited State Dynamics.

Different types of ultrafast spectroscopy employ different detection mechanisms, but all are based on the idea of a pump initiated photochemical process which is observed with a probe interaction at various time delays.

1.3 Dissertation Overview

This introduction provides a brief overview of the relevant science and techniques relating to ultrafast chemistry. The following chapters will cover the work I conducted relating to the dynamics of the excited states of molecules and clusters. Chapter 2 covers the experimental details of both the construction and preliminary results of the XUV absorption spectrometer as well as the TOF-MS. Chapter 3 presents the theoretical methodology employed for modeling and understanding the excited states of molecules and clusters. Chapter 4 presents the results of Rydberg enabled dissociation of n-butyl bromide. It focuses on the dynamics of the A state direct dissociation of C-Br, the ion-

pair formation of $C_4H_9^+/Br^-$, and C-C and C-H fragmentation of the carbon backbone. Chapter 5 covers the work done on titanium oxide clusters including the relationship between the first excited states of the stoichiometric $(TiO_2)_n$ clusters and their lifetimes as well as the effect of oxidation on excited state properties of Ti_nO_{2n-x} (x = 1 and 2). Chapter 6 concludes the dissertation and offers future directions.

CHAPTER 2

EXPERIMENTAL METHODS

2.1 Introduction

Within this dissertation a variety of experimental techniques were developed and utilized for studying the femtosecond dynamics of molecules and clusters. The following chapter provides an in-depth discussion of the experimental techniques used during my research.

Section 2.2 provides an overview of the fundamentals of ultrafast lasers and optics. Laser pulses on the fs time scale and the experiments that use them requires precision in generation, characterization, and manipulation. First, it discusses the development of high-power, ultrafast laser systems. Following that, it introduces the methods employed for characterizing the pulse duration and beam shape, both of which are critical for the experiments conducted in this thesis. Regular optimization and characterization of the driving laser system is done to maintain ideal experimental conditions.

Section 2.3 covers the work conducted on the development and construction of an extreme ultraviolet (XUV) absorption spectrometer. Construction of this instrument required precision construction and design of a variety of components including multiple nonlinear optical manipulations for the compression of 35-fs pulses to < 10-fs pulses and generation of XUV photons. A mathematical description of the important nonlinear processes is given and preliminary results acquired by the instrument are presented as validation of the instruments condition.

Section 2.4 gives a brief overview of the time-of-flight mass spectrometer (TOF-MS) used for additional experimental analysis. A description of the instrument is given followed by a mathematical description of the methods used for experimental analysis. Both the XUV absorption spectrometer and the TOF-MS are used for studying ultrafast dynamics of molecules in the gas phase.

2.2 Fundamentals of Ultrafast Lasers and Optics

2.2.1 Chirped Pulse Amplification

In 2018 Strickland and Mourou were awarded the Noble Prize in physics for the invention of chirped pulse amplification for generating high power, femtosecond lasers.[10,11] This technology relies on a Ti:Sapphire laser to determine the pulse duration and the subsequent amplification using a high power nanosecond Nd:YAG pump laser. The output of the seed laser is ~ 500 mW of power with a center wavelength of 800 nm and a FWHM spectral bandwidth of ~60 nm. This short pulse is then stretched temporally using a system of grating passes before entering the amplifier. Stretching the pulse duration prevents any damage to optics and allows the beam to be amplified before being compressed through another series of grating passes. A representation of this process is presented in Figure 2.1.

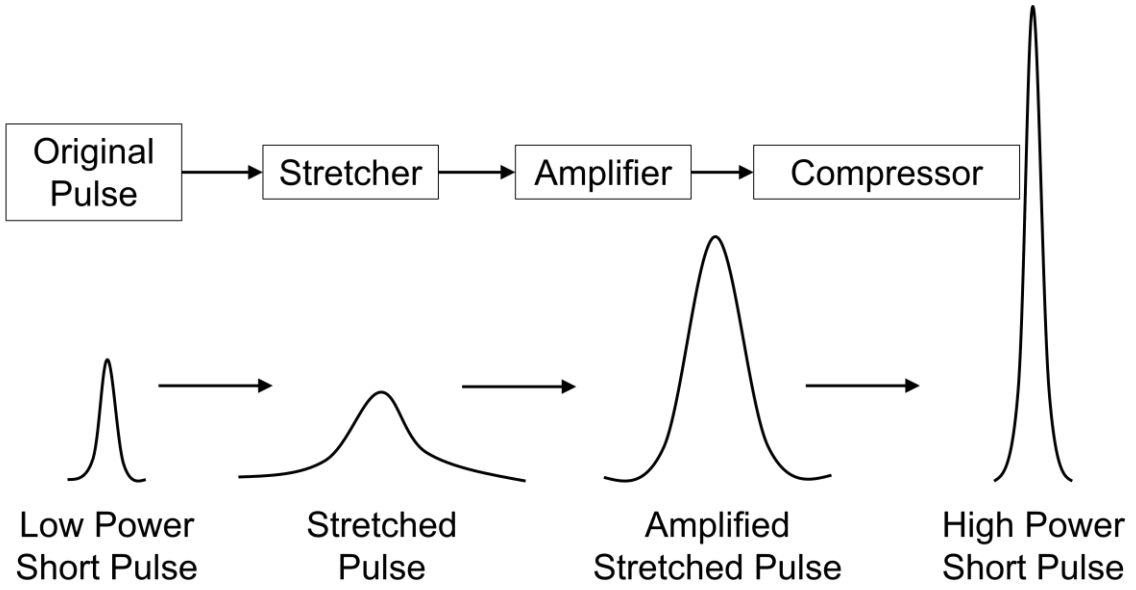

Figure 2.1 Step-wise Representation of the Generation and Amplification of Ultrashort Laser Pulses as Used in Chirped Pulse Amplification.

The driving laser for the work described herein is the Solstice Ace system made by Spectra-Physics. The system has an output of 7 mJ of energy and a repetition rate of 1 kHz (center wavelength 800 nm). Within the one box system, a Ti:Sapphire seed laser with an output of ~500 mW is amplified via chirped pulse amplification using a Nd:YAG pump laser. The interior optics and lasers are shown in Figure 2.2. The output of the Solstice Ace is used in all of the experiments presented within this thesis.

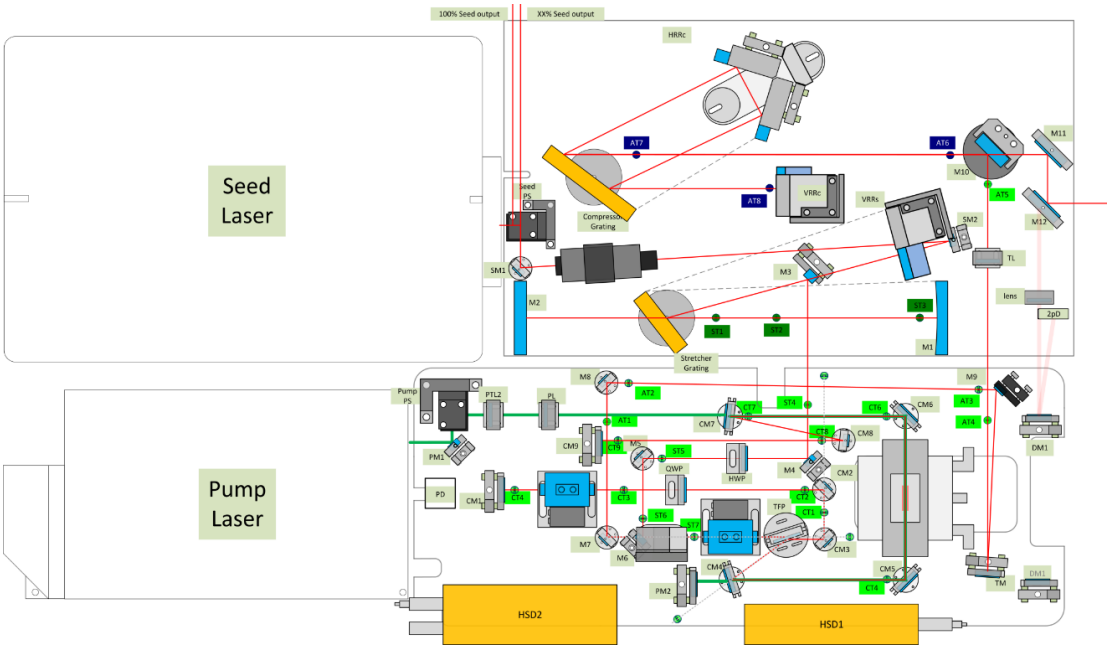

Figure 2.2 Optical Layout of the Solstice Ace Laser System Used in All Experiments.

2.2.2 Beam and Pulse Characterization

Optimization of the instrument depends heavily on the shape and pulse duration of the laser beam. Characterization of these parameters are done regularly to ensure proper beam profiles and pulses. Gaussian beam equations are used for determining the size of the laser beam at each point along the focal path. At the focus, the beam waist (w_F) is found using

$$w_F = \frac{f\lambda_0 M^2}{\pi w_L}, \tag{2.1}$$

where f is the focal length of the lens, λ_0 is the center wavelength of the beam, and w_L is the radius of the collimated beam at the focal lens. For a perfect Gaussian mode beam, the beam mode factor (M) is equal to 1.00 and any deviation in the mode leads to $M > 1$. The beam size at any point along the focal path can be determined using

$$w_z = w_F\left[1 + \left(\frac{\lambda_0 z}{\pi w_F^2}\right)\right]^{1/2}, \tag{2.2}$$

where z is the distance from the focal lens along the beam path. A plot of beam waist and distance from the focusing optic is shown in Figure 2.3.

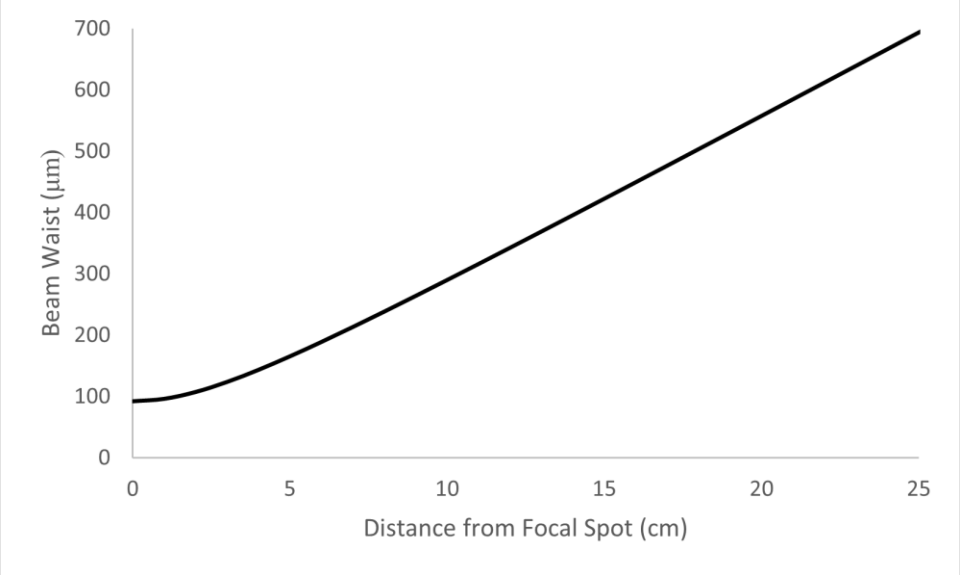

Figure 2.3 Plot of Beam Waist Versus Distance from the Focusing Optic for a 2.0 m Lens and a 1.1 cm Initial Diameter. The Minimum Beam Waist is 92.6 μm.

The maximum intensity of the beam at any point is found via

$$I_z = \frac{2P_L}{\pi w_z^2 \tau}, \tag{2.3}$$

where P_L is the average power of the laser in joules and τ is the pulse width. A plot of intensity versus beam waist is given in Figure 2.4 and shows the exponential relationship, highlighting the importance of beam waist characterization.

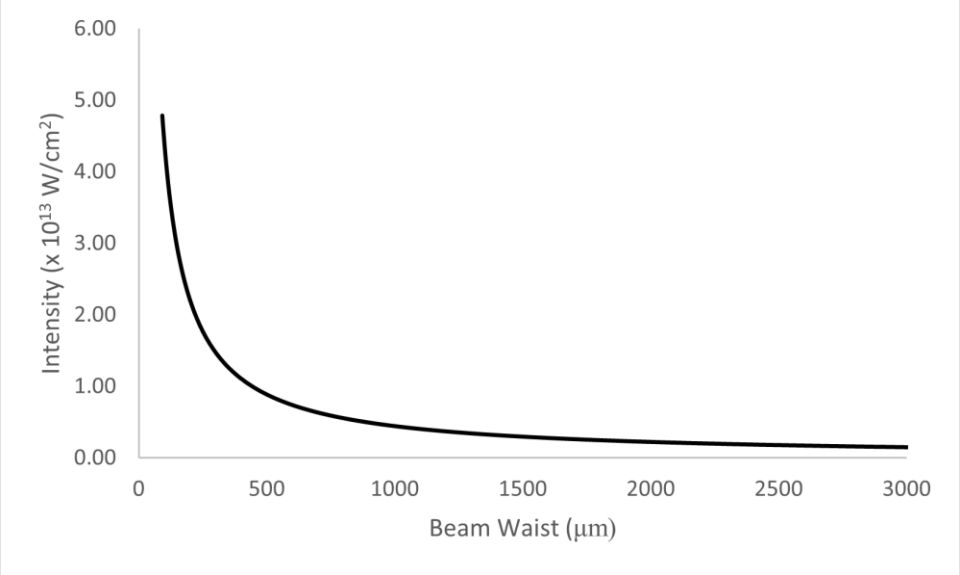

Figure 2.4 Plot of Intensity with Respect to Beam Waist for a 2.0 m Lens, a 35.0 fs Pulse, an Average Power of 1.8 W, and an Initial Waist of 1.1 cm.

Diagnosis of the beam profile can be done using multiple methods. The easiest and most routine way of checking the beam profile is to use a deconstructed webcam paired with a short focal lens (~ 5 cm). Using a very weak, highly filtered, beam focused on to the webcam charge-coupled device (CCD), it is possible to observe the shape of the beam profile at the focus (Figure 2.5). Multiple webcams are positioned along critical points of the XUV instrument for rapid determination of beam shape.

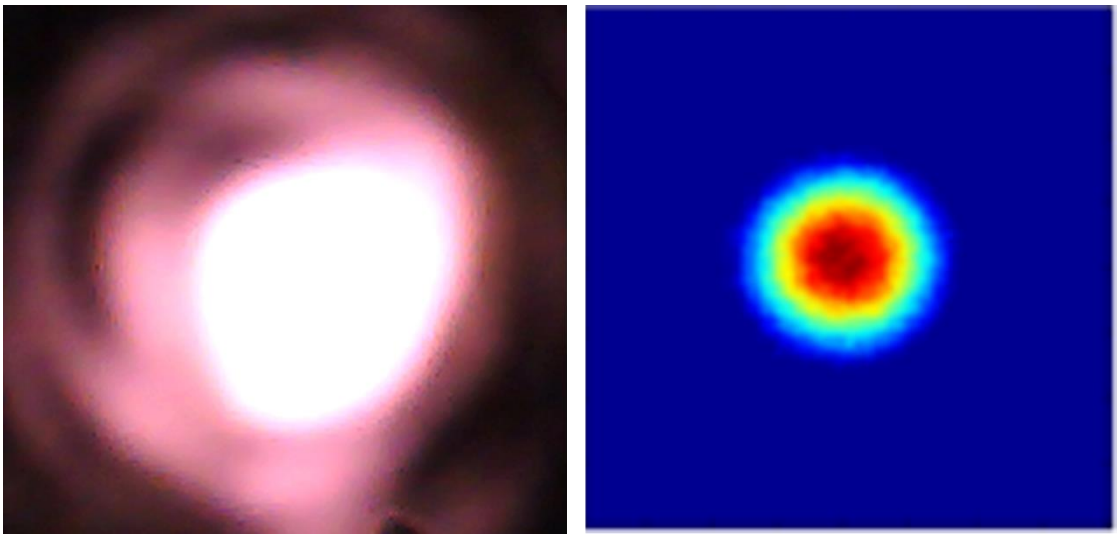

Figure 2.5 Webcam Images of Focused Gaussian Laser Beam with Raw Image on the Right and Intensity Image on the Left.

If the pixel size on the CCD is known, it is possible to calculate the beam diameter from the webcam. However, a more precise way is to determine the beam waist (radius) from a knife edge scan. Determination of the beam size using a knife edge scan is done by setting up a power meter and a knife edge on a micrometer manual delay stage. The relationship between the power and the knife edge position is related via an Error Function (erf) following

$$P_x = \frac{P_L}{2}\left[1 - erf\left(\frac{2^{1/2}x}{w_x}\right)\right], \tag{2.4}$$

where P_x is the power at a position x along the beam waist and w_x is the beam waist at point x. Fitting the data to this equation provides the beam waist at the point of the knife edge in the z direction. An example of a knife edge scan done near the focal spot of a 50 cm lens is shown below in Figure 2.6.

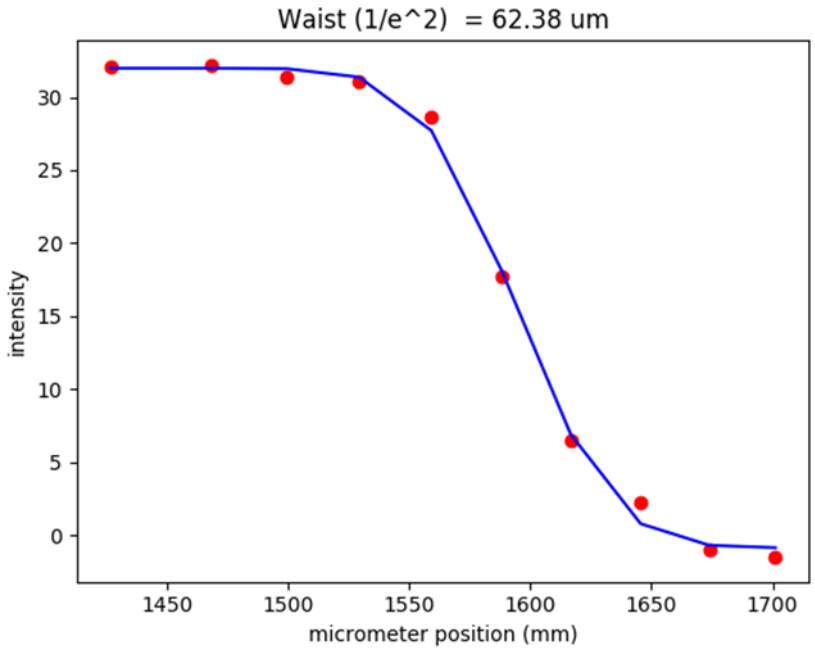

Figure 2.6 Results of a Knife Edge Beam Waist Measurement at 50 cm Away From a 50 cm Focusing Lens.

Pulse duration is regularly measured using both intensity and interferometric autocorrelators. The 35-fs pulse produced by the Solstice Ace is measured using a Single Shot Autocorrelator (SSA) from Spectra-Physics. Pulses less than 35-fs measured using a Femtometer from Spectra-Physics. Both instruments are based on a Michelson interferometer shown in Figure 2.7. It is important to note that the SSA is an intensity autocorrelator and is spatially measured. This is similar to the Michelson interferometer used in the Femtometer, but the beams are not colinear and there is no moving part to cause interference.

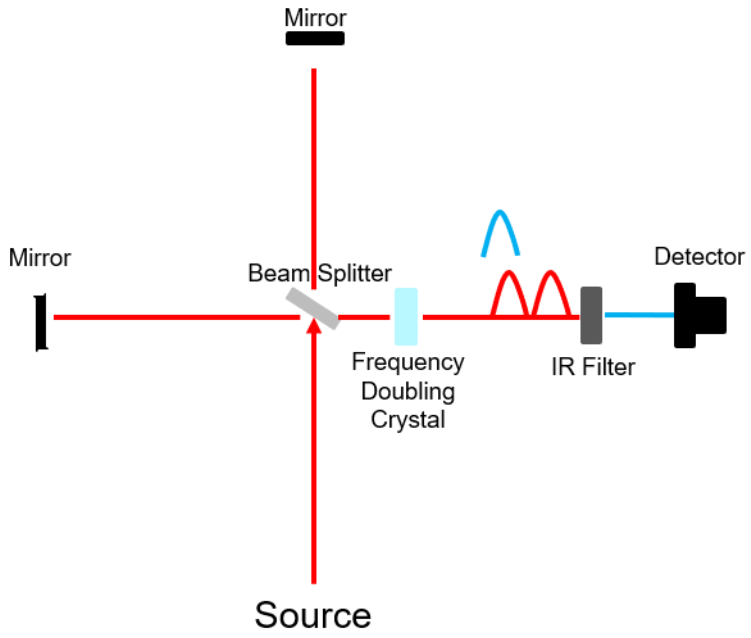

Figure 2.7 Layout of a Michelson Interferometer. The Incoming Beam is Split and One Path has a Moveable Mirror Which Causes an Oscillation in the 400 nm (Second Harmonic) Beam with Respect to the Mirror Position.

In these interferometers, the incoming beam is split along two paths. One path has a variable delay arm which can be adjusted either manually or automatically. The two beams are then recombined on a frequency doubling crystal to produce a 400 nm output. This output is then monitored using a detector and has the delay varies, the resulting power on the detector varies and the pulse width can be extracted. Autocorrelators are critical for measuring pulses with ultrashort time scales where an electronic apparatus, such as a fast photodiode, is limited to pulses longer than 100 ps. A trace of the output pulse of the Solstice Ace is shown in Figure 2.8 and was collected using the Femtometer.

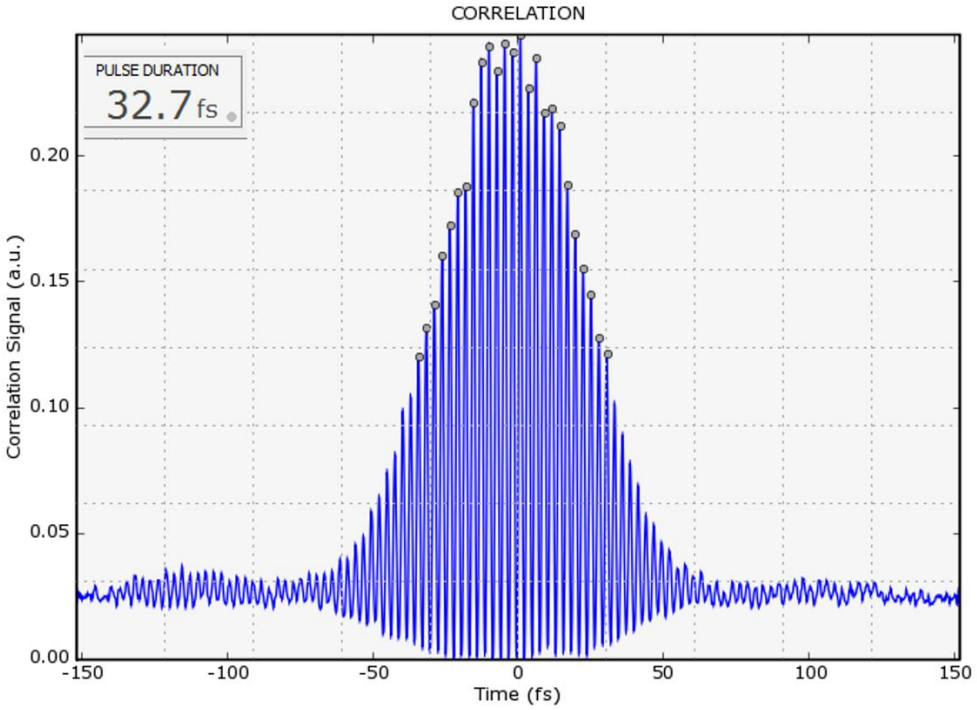

Figure 2.8 Autocorrelation Trace of a Sub-35 fs Pulse Collected Using the Femtometer.

2.3 Development of XUV Spectrometer

Construction of the femtosecond XUV absorption spectrometer began in January of 2017. The designs for the spectrometer were based on previously published specifications. Instrument consists of a high harmonic generation (HHG) source, a focusing Toroidal mirror, a sample cell, a flatfield grating, and a CCD camera. Each optic in the instrument has an optimal position based on the focusing parameters of the laser and the optic. Additionally, each optic from the HHG source onwards must be kept under high vacuum (10^{-7} Torr) as a medium such as air would hinder the propagation of the XUV light. Each chamber is connected to a roughing pump and a turbo pump. The vacuum chambers were designed and modified to fit the required beam path based on the optics. Figure 2.9 shows the optimal beam path and optics placements for the instrument.

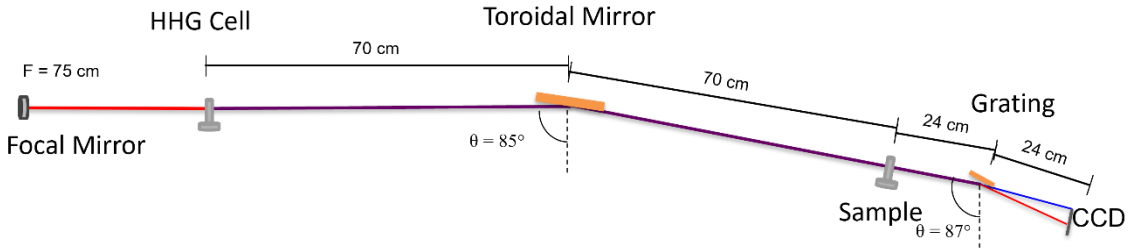

Figure 2.9 Optical Path of the XUV Absorption Spectrometer from the Entering Focal Mirror to the CCD Camera. Each Optic has an Optimal Position and Relative Grazing Angle Which Dictates the Optical Layout.

Details of the instrumental alignment, optimization, and use will be outlined in the following sections. Optimization of the instrument requires diagnostics of multiple beam parameters including pulse duration, beam shape, focusing, and chirp. The XUV instrument was paired with a hollow core fiber (HCF) and chirped mirrors for pulse compression. This technique allows for pulse length compression from 35 fs to < 10 fs pulses. A full layout of the optics before the instrument is shown in Figure 2.10 and will be described in further detail in the following sections.

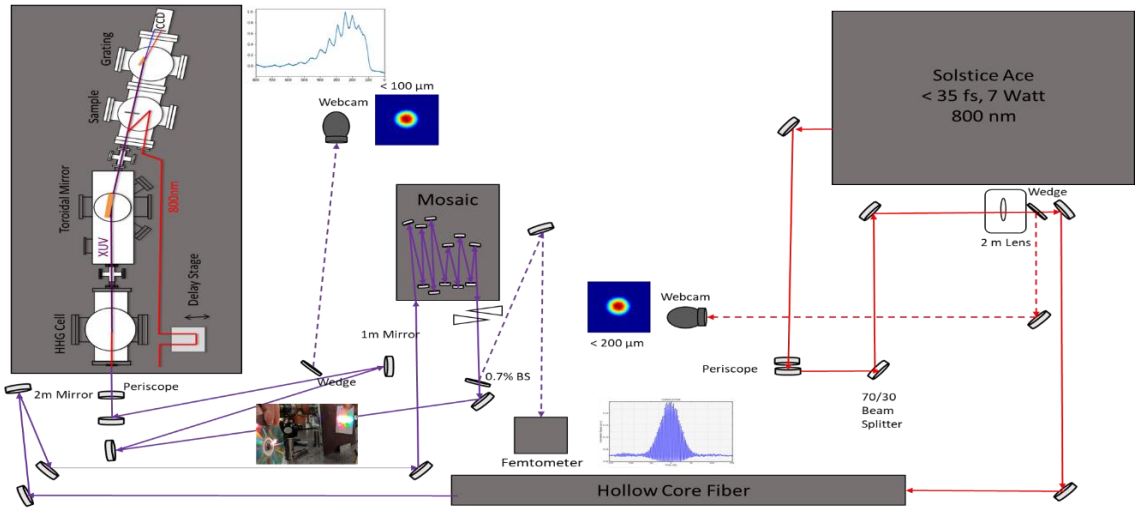

Figure 2.10 Optical Layout of the Full Laser and Instrument Used for the XUV Spectrometer.

2.3.1 Instrumental Design

The key components of the XUV spectrometer are depicted in Figure 2.10 and will be described briefly here. Throughout the instrument, custom mounts, flanges, and electronics were made to optimize the instrument and benefit the ease of use. The incoming ~10 fs beam is focused using a 75 cm focal mirror producing a minimum beam waist of 34.7 μm. The focal mirror is on an adjustable delay to allow for phase matching (optimization) of the focal spot with respect to the HHG source. The HHG source sits centrally in the first chamber and different pathlengths of the source are used interchangeably for difference experiments. The HHG source is mounted on a motorized 2” stage in both the x and y directions. This stage is controlled externally using an Arduino and python code to allow for precise alignment of the source to the beam.

As soon as XUV light is generated, any interaction with a medium will distort the beam, thus the instrument is kept under high vacuum following the focal mirror. A balancing act must be achieved between the internal pressure of the HHG source and the external vacuum of the chamber. During experiments, the HHG pressure is kept between 30 and 100 Torr while maintaining a vacuum pressure of $< 1 \times 10^{-4}$ Torr. The HHG source has a sub millimeter hole for the incoming laser beam which was drilled with the high intensity beam. Over time the hole widens with use. This is counteracted by resealing the hole with shrink wrap tubing then redrilling with the laser.

The process of phase matching describes the optimization of several variables for the production of XUV light. Parameters such as focal position, gas pressure, laser power, and relative chirp all affect the production of high harmonic light. Daily

optimization of phase matching is done before conducting experiments to tune the intensity and wavelength of the generated photons.

Following the HHG source, the non-upconverted 800 nm light is blocked by a 0.6 μm aluminum filter mounted on a motorized stage for ease of use. The Al filter allows transmission of XUV light between 20 and 72 eV but filters away lower energy light leaving only the XUV photons for the experiment. Behind the Al filter is the toroidal mirror which the XUV light hits at a 12° glancing angle and is refocused at the sample cell. Alignment of the toroidal mirror drastically affects the beam astigmatism of the XUV light and a push/pull mirror is mounted after the toroidal mirror for quick adjustment. The XUV beam is refocused into the sample chamber which is designed and mounted in a similar fashion as the XUV source. For preliminary results, the samples were in the liquid phase and heated to achieve a sufficient vapor pressure for 5-15 Torr backing pressure in the chamber. Like the HHG source, the sample source is mounted on a motorized x/y stage which is adjusted to the beam path using a webcam and a push/pull mirror.

For time resolved experiments, the beam is split before the 75 cm focal mirror and directed outside the instrument to an automated delay stage with resolution capable of attosecond step sizes. The pump beam is then directed into the sample chamber via a window and recombined into the sample at a small relative angle to the XUV beam. The motorized Al foil mount allows for simultaneous alignment of the pump 800 nm beam and the probe XUV beam onto the sample cell. With minor adjustments, it is possible to study solid state thin films in the XUV spectrometer.

After the sample cell, the 800 nm probe is blocked with a second Al foil before the grating and detector chamber. The CCD camera is sensitive to even the smallest amount of light, so the grating chamber is separated from the sample chamber with a thick aluminum plate to minimize ambient light from windows or the pump laser beam. A flat-field spherical variable-line-space (SVLS) grating is used to diffract and focus the XUV photons on to the CCD camera. The design of the grating allows for specific separation and focusing such that different photon energies are diffracted and focused uniquely with respect to each other. A detailed description of the toroidal mirror and grating can be found in the literature[12] and determination of diffraction distance and focal distance for each photon energy can be found via the following equations. First, the standard grating equation is given by

$$m\lambda = d[\sin\alpha - \sin\beta], \tag{2.5}$$

where α and β are the incident and 1st order diffraction angles, respectively, m is the diffraction order, and d is the groove spacing of the grating. For a spherical variable-line-space grating, the distance of diffraction and focus can be found using

$$\frac{\cos^2\alpha}{p} + \frac{\cos^2\beta}{q} - \frac{\cos\alpha + \cos\beta}{R} + 2(\sin\alpha + \sin\beta)\frac{b^2}{R} = 0, \tag{2.6}$$

where p and q are the incoming and outgoing arms of the XUV beam and R is the radius of the grating (Figure 2.11).[12]

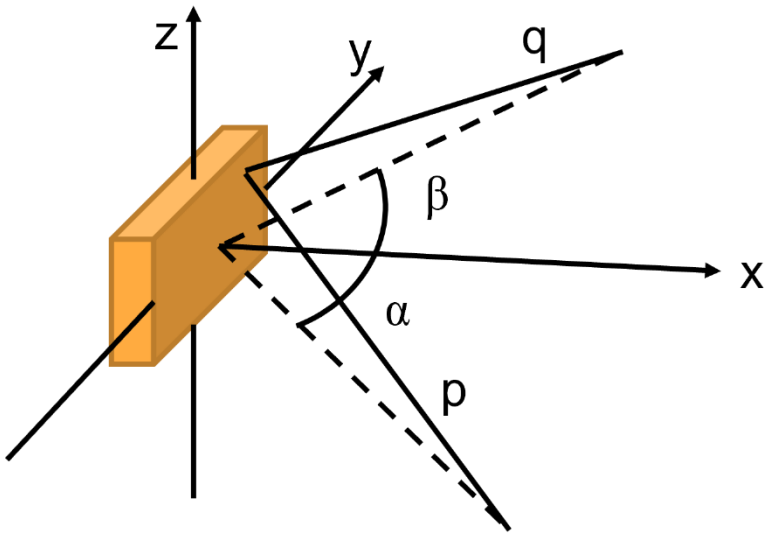

Figure 2.11 Optical Layout and Parameters of the Flat-Field Spherical Variable-Line-Space Grating Used in the XUV Spectrometer.

Solving for the x and y positions of the XUV photons on the CCD camera can be found via

$$x = q\cos\beta\,, \tag{2.7}$$

and

$$y = -q\sin\beta\,, \tag{2.8}$$

Figure 2.12 shows the diffraction and focal distance of the XUV photons relative to their energy.[12]

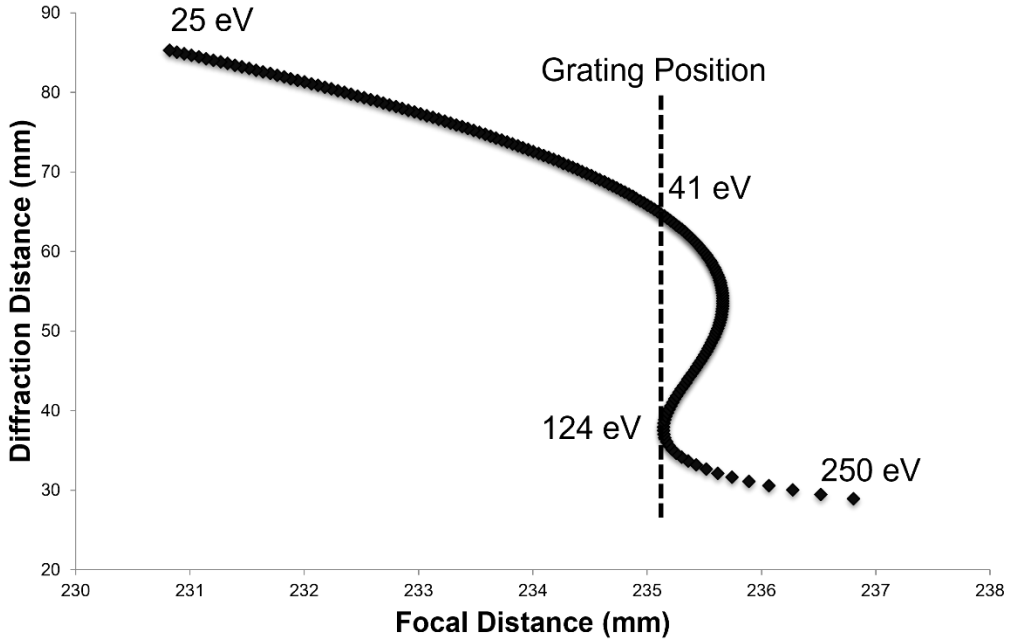

Figure 2.12 Focal and Diffraction Distance of the XUV Beam by the Flat-Field SVLS Grating.

Development of the XUV spectrometer also required the development of numerous programs dedicated to collecting and processing data. Both the CCD and the delay stage can be operated via Labview and can work simultaneously to collect time resolved data. Additionally, Labview can be used to do preliminary data processing such as background subtraction and averaging. However, most of the data processing code was developed in Python and written from scratch to be used specifically for XUV analysis. The key components of the program are the ability to average, normalize, and run statistics on large sets of data rapidly. Features have been added to reduce the instrumental error inherent in this type of spectroscopy. Analysis of the samples requires the application of Beer's Law as absorption occurs at low intensities. As such, the optical density of the sample is given by

$$OD = -\log_{10}\frac{I_{Sample}}{I_0}, \tag{2.9}$$

where I_{Sample} is the XUV intensity after absorption from the sample and I_0 is the XUV intensity without a sample present. Noise reduction as a data processing tool is critical for studying time dynamics when changes in optical density are on the order of 1%.

2.3.2 High Harmonic Generation

High harmonic generation (HHG) is the process of generating high order harmonics of a laser field through a non-linear interaction with a medium, most often a Noble gas. This phenomenon was first demonstrated experimentally in 1977 by Burnette et al. but was not explained theoretically until 1993 when Corkum provided the semi-classical "Three Step Model" of HHG.[13] The model describes the interaction of an electron and the intense, oscillating electric field of a focused laser beam. At high intensities (~10^{14} W/cm^2), the electric field of the laser suppresses the Coulomb potential that binds an electron to its nucleus and the electron can then tunnel away from the nucleus (step 1). With the reversal of the electric field, the now free electron is driven back to the nucleus (step 2). The collision of the electron and the nucleus emits a high energy photon (step 3). This process is outlined pictorially in Figure 2.13.

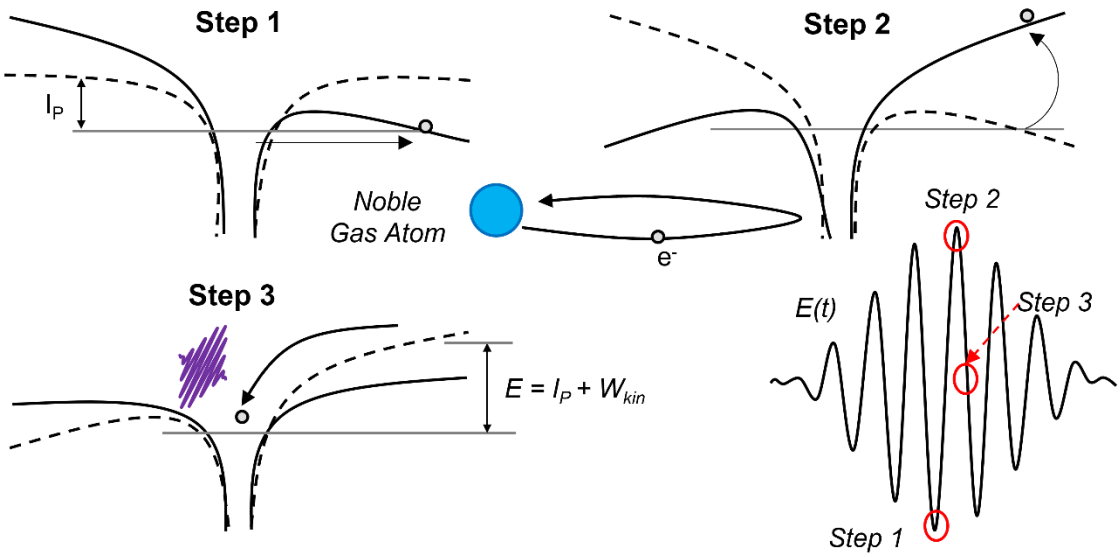

Figure 2.13 Pictorial Representation of the Three-Step-Model of High Harmonic Generation. Step 1 Shows the Bending of the Potential Well and Electron Tunneling Away from the Nucleus. Step 2 Shows the Reversal of the Potential Well with the Reversal of the Electric Field of the Laser. Step 3 Shows the Return and Recombination of the Ejected Electron which Generates a High Energy Photon.

Noble gases are often used for HHG given their high electron binding energy. The energy of the high order photon generated by the interaction of a high intensity pulse and the XUV photons generated by a Noble gas can be quantitatively estimated using the semiclassical model of HHG. This process can be described mathematically in terms of the electric field of the laser, *E(t)*

$$E(t) = E_0\, cos[\omega_0 t + \varphi(t)]\,, \tag{2.10}$$

with ω_0 being the fundamental frequency of the driving laser, φ is the phase of the electric field at time, *t*, and time is normalized to the laser period, T_0, and angular frequency $\omega_0 = 2\pi/T_0$. The effective binding potential of a valence electron is given by

$$V_{Coulomb}(\vec{r}) = \frac{-e^2}{4\pi\epsilon_0 \vec{r}}. \tag{2.11}$$

Additionally, the Coulomb potential is described in terms of the charge of the electron, *e*, the position vector of the electron, $\vec{r}$, and the electric permittivity in vacuum, ϵ_0. At the instant of interaction, the potential of the electric field, V_{EF}, is linear with respect to $\overrightarrow{E_t}$ via

$$V_{EF}(\vec{r},t) = e\vec{E}(t)\vec{r}, \tag{2.12}$$

and the effective potential, V_{eff} then becomes

$$V_{eff}(\vec{r},t) = V_{EF}(\vec{r},t) + V_{Coulomb}(\vec{r}) = e\overrightarrow{E_t}\vec{r}\frac{-e^2}{4\pi\epsilon_0\vec{r}}. \tag{2.13}$$

Treating the electron classically in step 3, the average kinetic energy ($\overline{W_{kin}}$) of the electron as determined from Newton's equations of motion is given by

$$\overline{W_{kin}} = U_p = \frac{E_0^2 e^2}{4m_e\omega^2}. \tag{2.14}$$

As long as the intensity of the laser is sufficiently high, recombination can occur at many phases of the laser pulse. Averaging over the phases give the photon energy in terms of the pondermotive potential (U_P) which is exclusively dependent on the properties of the driving laser and is given by

$$U_p = 9.3 \times 10^{-14} I_L \lambda_0^2. \tag{2.15}$$

The maximum kinetic energy gained by a given driving laser occurs when p = 17° and give a cutoff energy of

$$E_{cutoff} = I_P + 3.17U_P. \tag{2.16}$$

As an example, Ar (I_P = 15.78 eV) in a laser field with a peak intensity of 3 x 10^{14} W/cm^2 can produce XUV photons with energies up to 72 eV.

The "Three Step Model" predicts the emission of a high energy photon every half cycle of the of the laser period ($\frac{\tau}{2}$) and the Fourier transform of the frequency of the XUV

emission shows an interference pattern with a photon energy spacing of $2\hbar\omega_L$, resulting in the production of only odd-order harmonics [$\omega_{XUV} = (2n + 1)\omega_L$]. Reducing the number of cycles in the laser pulse thus reduces the interference of the XUV bursts and allows for the generation of a continuum of energy. For a 35-fs pulse, there are approximately 13.5 optical cycles. However, using the hollow core fiber method of pulse compression (described in the following subsection) leads to the generation of a sub-10 fs pulse with less than 4 optical cycles within the pulse packet. The shortest observed pulse entering the XUV instrument was found to be 8 fs. An example of discrete and broadened XUV light is shown in Figure 2.14.

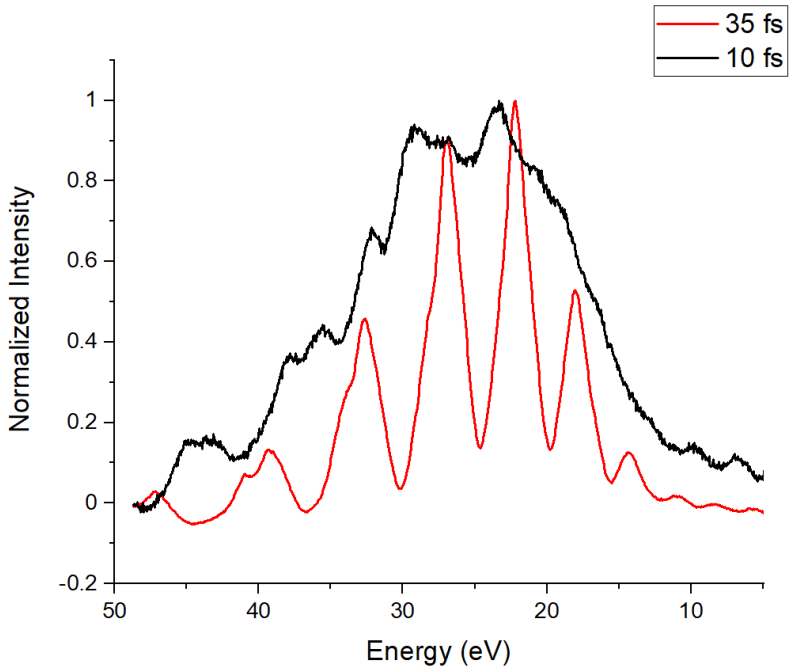

Figure 2.14 XUV Photons Generated with a 35 fs Pulse (Red) and a 10 fs Pulse (Black) Demonstrating the Broadening Effect of Shortened Pulses.

2.3.3 Spectral Broadening and Pulse Compression

The fastest commercially available laser system is limited to the spectral bandwidth of a Ti:Sapphire crystal (~20 fs). Thus, to achieve few-femtosecond pulses

this research uses a hollow core fiber (HCF) set up for spectral broadening and pulse compression. A mathematical and experimental description of this process is outlined in the following sections. Considering the Heisenberg uncertainty principle, it can be seen that the pulse duration is limited by the spectral bandwidth of the laser. This limitation for a Gaussian pulse is given by

$$\Delta\upsilon\Delta\tau = \frac{4\ln 2}{2\pi} \approx 0.44. \tag{2.17}$$

In this case, 0.44 is known as the time-bandwidth product. Converting from $\Delta\upsilon$ to $\Delta\lambda$ for simplicity can be done using the following relationship:

$$\Delta\lambda = \Delta\upsilon\frac{\lambda_0^2}{c}, \tag{2.18}$$

where λ_0 is the center wavelength and c is the speed of light. For a Ti:Sapphire laser with a full-width half-maximum (FWHM) bandwidth of 60 nm, the pulse duration is limited to approximately 25 fs. In order to further compress the pulse temporally, the spectral bandwidth must increase. This spectral broadening can be achieved through a nonlinear process called self-phase modulation (SPM) and can be achieved through the hollow core fiber technique. When a high intensity laser pulse interacts with a medium with a nonlinear index of refraction over a distance L, the frequencies at the lower end of the spectrum are reduced further and the frequencies at the upper end are increased thus leading to an overall increase in the FWHM of the bandwidth. The bandwidths of the output of a HCF setup with different Ne gas pressures is shown in Figure 2.15. A full mathematical account of this process is given below.

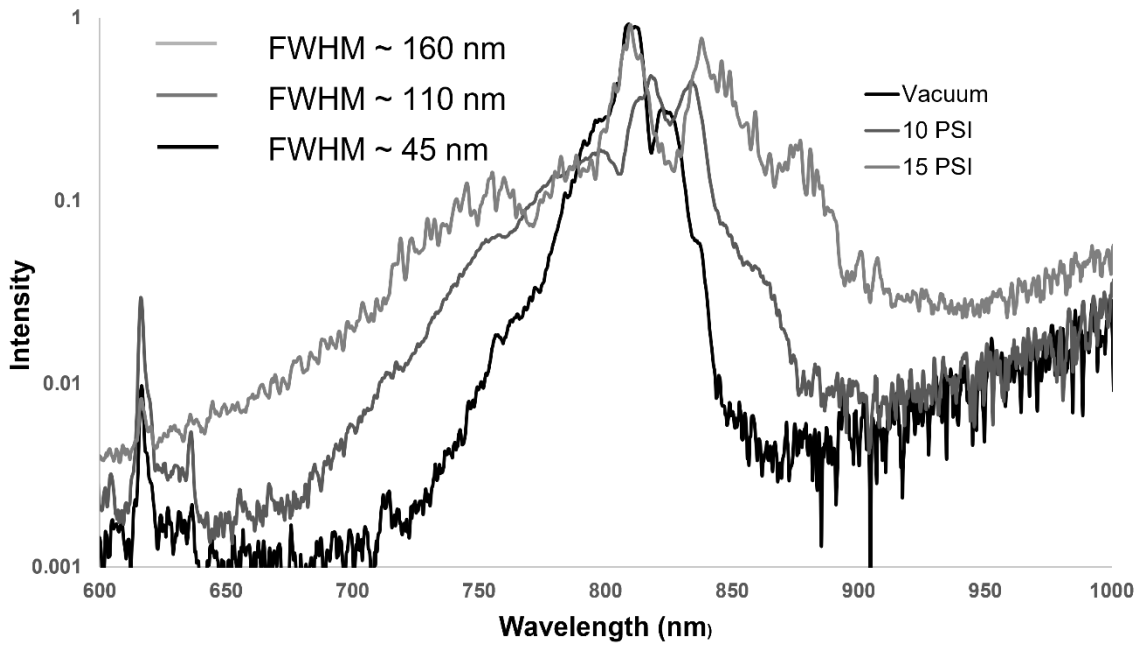

Figure 2.15 Spectral Broadening Induced by Coupling with the Hollow Core Fiber with Varying Ne Gas Pressures.

A Gaussian beam can be represented by the following equations. First, the intensity profile in terms of time is given by

$$I_L(t) = I_0 e^{4\ln 2\frac{t^2}{\tau^2}}, \tag{2.19}$$

where I_0 is the peak intensity and it is given in terms of the peak field amplitude E_0 by

$$I_0 = \frac{1}{2}\epsilon_0 c E_0^2. \tag{2.20}$$

Here, ϵ_0 is the permittivity of light and E_0 is the peak electric field amplitude. The refractive index of a medium with a Kerr nonlinearity is written as

$$n(t) = n_0 + n_2 I(t), \tag{2.21}$$

where n_0 is the field-free nonperturbed refractive index of the medium, n_2 is the nonlinear refractive index at the frequency ω (values obtained from literature), and $I(t)$ is the laser

radiation intensity. Determination of the magnitude of the nonlinear phase shift caused by the optical Kerr effect for a given medium over a length (L) is determined via

$$\phi_{nl}(t) = -\frac{2\pi}{\lambda_0} n_2 I(t) L. \tag{2.22}$$

This equation leads to the conclusion that the intensity dependence of the refractive index is related to the field intensity of the laser pulse and the time dependence of the nonlinear phase shift. In nonlinear dispersive media, the up and down shifts in the frequency introduces new frequency components leading to spectral broadening. This allows for the generation of shorter pulse. From this, the time dependent frequency variation is given by

$$\Delta\omega(t) = \frac{d}{dt}\phi_{nl}(t) = \frac{2\pi}{\lambda} n_2 L \frac{d}{dt} I_L(t), \tag{2.23}$$

and the maximum induced spectral broadening is then

$$\Delta\omega(t) = \frac{2\pi}{\lambda} n_2 L \frac{I_0}{\tau}, \tag{2.24}$$

where I_0 is the peak intensity of the laser pulse and τ is the FWHM of the pulse duration.

Coupling between the laser beam and the hollow core fiber drastically affects the degree of broadening and the mode of the outcoming beam. For a hollow core fiber of bore radius, a, the lowest loss mode is the EH_{11} mode which is linearly polarized. The intensity profile as a function of the radial component, r, is given by

$$I(r) = I_0 J_0^2 \left(2.405 \frac{r}{a}\right), \tag{2.25}$$

where J_0 is the zero-order Bessel function and a is the bore radius of the fiber. The real, β, propagation constant and the imaginary, $\alpha/2$, field attenuation coefficient for the EH_{11} mode are given by

$$\beta = \frac{2\pi}{\lambda_0}\left[1 - \frac{1}{2}\left(\frac{2.405\lambda_0}{2\pi a}\right)^2\right], \tag{2.26}$$

and

$$\frac{\alpha}{2} = \left(\frac{2.405}{2\pi}\right)^2 \frac{{\lambda_0}^2}{2a^3}\frac{v^2+1}{\sqrt{v^2-1}}, \tag{2.27}$$

where v is the ratio between the refractive indices of the external (fused silica) and internal (Noble gas) media. This can be estimated to a value of approximately 1.5. For Gaussian pulses and in the absence of dispersion the maximum broadening, $\delta\omega_{max}$ with a fiber of length L is given by

$$\delta\omega_{max} = 0.86\gamma P_0 z_{eff}\frac{1}{\tau}, \tag{2.28}$$

where P_0 is the peak power and z_{eff} is defined as

$$z_{eff} = \frac{1 - e^{-\alpha L}}{\alpha}, \tag{2.29}$$

and the nonlinear coefficient γ_{nl} is

$$\gamma_{nl} = \frac{n_2\omega_0}{c\pi a}, \tag{2.30}$$

where ω_0 is the center angular frequency of the laser. In order for ideal coupling, the focused beam cannot have any astigmatism and the ratio between bore radius and beam diameter is given by

$$\frac{w_0}{a} = 0.64, \tag{2.31}$$

where a is the bore radius of the fiber. The hollow core fibers used for pulse compression vary in length from 100 to 10 cm and the degree of frequency broadening is directly dependent on the length of the fiber. Fibers were purchased from Fredrick & Dimmock

Inc. and have a variety of bore radii ranging from 150 μm to 500 μm. The broadened spectrum obtained through SFM in a HCF is shown visually in Figure 2.16.

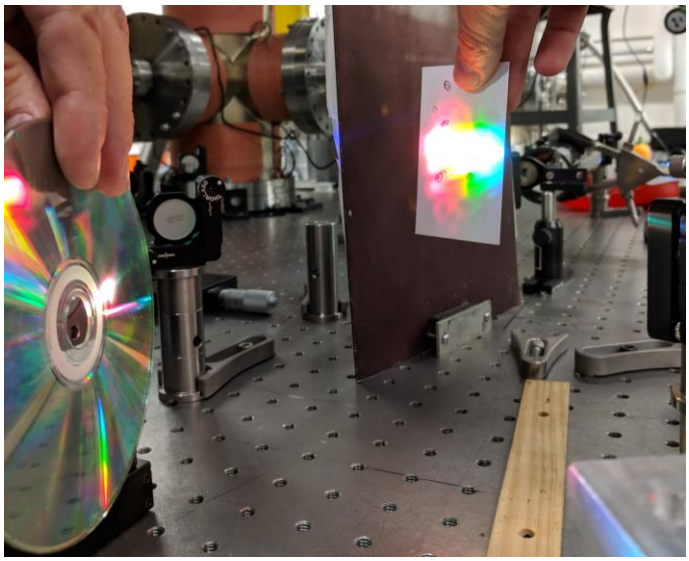

Figure 2.16 Visual of the Spectral Range Achieved via SFM in the Hollow Core Fiber with Ne Gas.

The spectrally broadened output from the HCF must be recompressed temporally using a series of chirped mirrors. The chirped mirror compression box (MOSAIC) is commercially available from FemtoOptics. Chirped mirrors recompress different wavelengths temporally by reducing their group delay as different wavelengths penetrate the optic to different depths. The resulting compressed pulse is measured using the Femtometer and the results are shown in Figure 2.17.

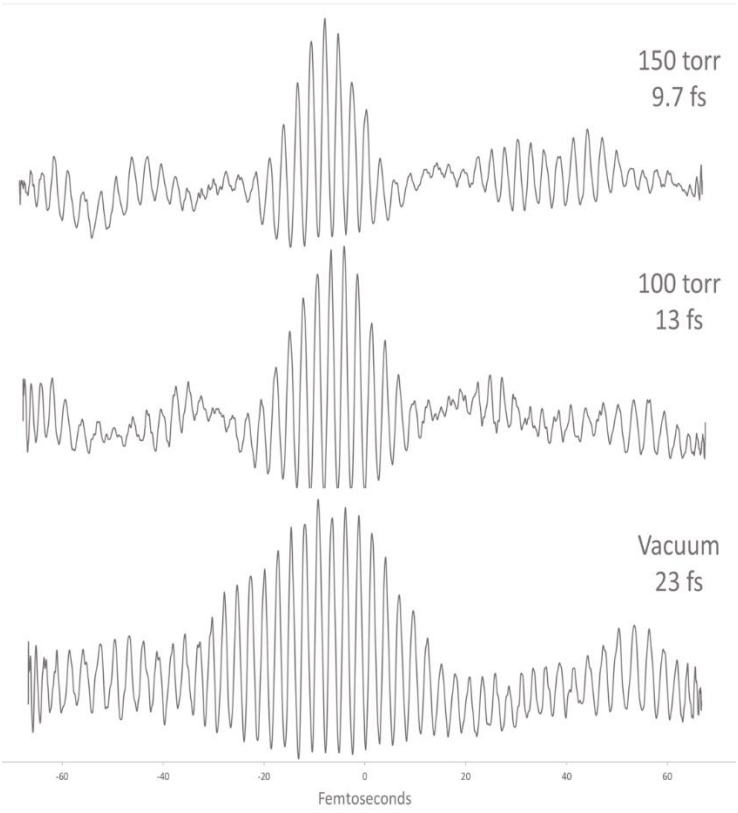

Figure 2.17 Pulse Compression from 23 fs to Sub-10 fs Pulse Using the Hollow Core Fiber with Different Pressures of Ne Gas.

2.3.4 Instrument Validation

Static XUV absorption spectra were collected as a means of testing the instrument with argon and brominated alkanes in the gas phase. Argon was used initially as a test of HCF broadening and XUV absorption calibration. However, Ar has a wide absorption edge at 40 eV which is not precise enough for a full calibration. The results, however, show the absorption edge and the effect associated with HCF broadening. Further, it functioned as a test molecule for data processing development. Shown below (Figure 2.18) is a simulated absorbance spectrum of Ar gas at 30 Torr from 10-100 eV generated from the Center for X-Ray Optics.[14]

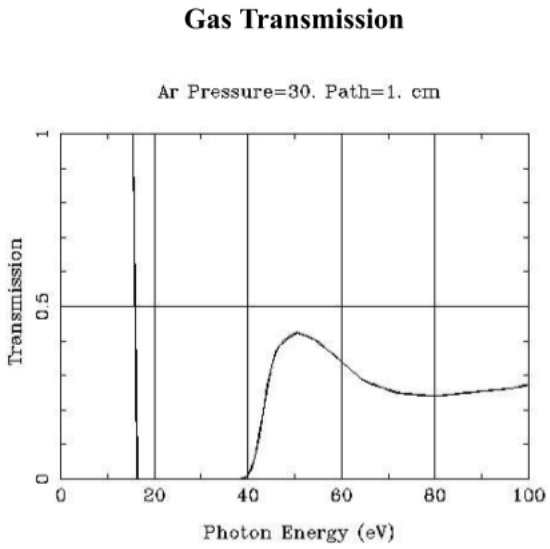

Figure 2.18 Calculated XUV Absorption of Ar Gas as Obtained from CXRO.

Using Ar in the HHG cell it is possible to generate harmonics with energies between 25-50 eV with little difficulty beyond ideal phase matching. The following plot (Figure 2.19) shows the absorption of an Ar sample for harmonics below 40 eV in energy. The left is with discrete odd harmonics generated with the 35-fs pulse and the right is with a continuum generated following pulse compression in the HCF with 10-psi Ne. As can be seen, the Ar sample blocks the harmonics lower than 40 eV in energy. Additionally, broadening of the HCF shows promise for an energy continuum.

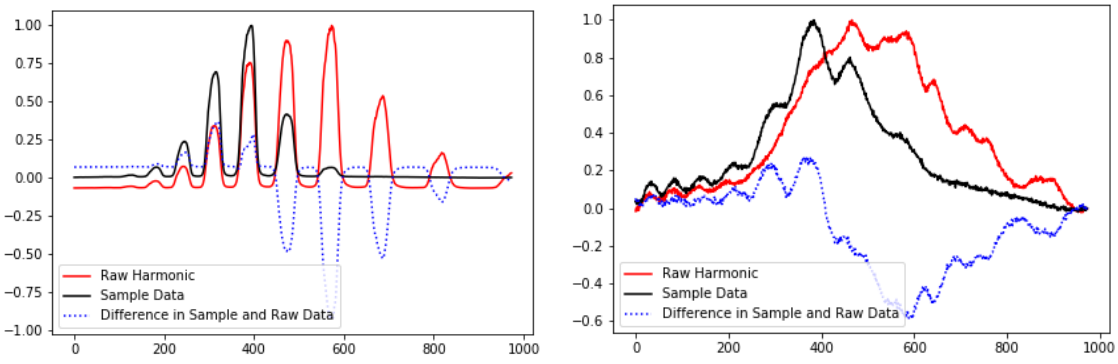

Figure 2.19 XUV Absorption of Ar Gas with Discrete and Broad XUV energies.

The next test was performed on 1,2-Dibromoethane (Figure 2.20). This molecule is a liquid at room temperature and has a vapor pressure of 54.0 Torr at 55 °C. In XUV studies, Br is used as a marker given its characteristic d-shell absorption around ~70 eV. In these studies, the high harmonics are generated with 50-70 Torr Ne and the sample cell contains ~ 5 Torr 1,2-Dibromoethane.

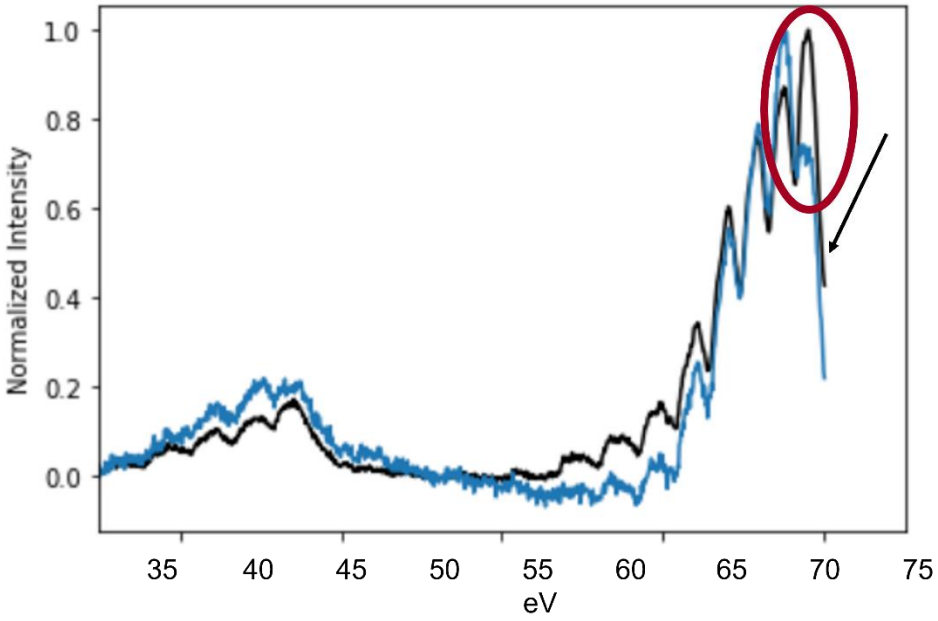

Figure 2.20 Absorbance of the D-Shell Electrons in 1,2-Dibromoethane. The Black Line Shows XUV Signal Without Sample Present and The Blue Line Shows XUV Throughput from the Sample.

2.4 Time of Flight Mass Spectrometry

A home-built Wiley-McLaren[15] type time-of-flight mass spectrometer (TOF-MS) is used to study the valence to excited state dynamics in both molecules and clusters. Full details of the instrument were published previously by other group members.[16] The TOF-MS is driven by the femtosecond laser using a 400 nm pump/800 nm probe set-up. The incoming 800-nm beam is frequency doubled with a frequency doubling KDP crystal and

the resulting 400-nm output was split with a dichroic optic into 400-nm and 800-nm beam paths. The 800-nm probe beam is steered onto a programmable motorized delay stage so that the relative position of the 400-nm pump beam and the probe beam can be manipulated with >1-fs resolution. The combined 800/400-nm beams are overlapped on a dichroic mirror and the overlapped beams are focused into the instrument with a 50-cm lens with intensities up to 10^{15} W/cm^2. Calibration of the TOF-MS was done previously. A diagram of the instrument is shown in Figure 2.21.

2.4.1Instrumental Layout

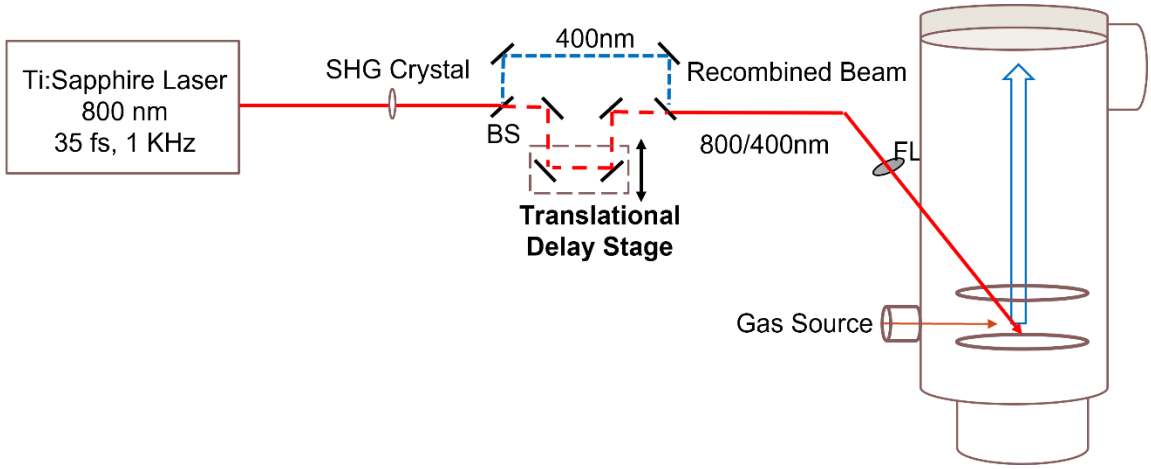

Figure 2.21 Instrumental Layout of TOF-MS Starting with the Solstice Ace Laser System Followed by the Second Harmonic Generation Source and Translational Delay Stage into the TOF-MS Assembly.

The TOF-MS consists of high voltage TOF grids (~4 keV), Einzel lenses for directing charged species, a 1.5-meter-long field-free region, and a chevron-type microchannel plate (MCP). All components are synchronized to the fs laser via a DG535 pulse generator. Voltage on the Einzel lenses and MCPs were adjusted for optimized signal-to-noise ratios. The instrument response function from full-width half-max (FWHM) of a gaussian trace of O_2.

2.4.2 Data Collection and Fitting Functions

Time resolved mass spectra collected on small molecules in the gas phase were acquired while maintaining a chamber pressure of 10^{-6} Torr. Mass spectra were recorded using 400 nm (3.1 eV) pump pulse and ionized with an 800 nm (1.55 eV) probe pulse. The 400 nm pump intensity is tuned to the excited state energies of the system being studied and the 800 nm probe pulse is kept below threshold for ionization such that no signal is observed with just the probe beam. Following dissociation, the probe pulse ionizes the fragment with the lowest binding energy and that fragment is recorded in the mass spectra. Transients were found for each ion by integrating over the ion peak in an averaged mass spectrum at each delay position. The transients were then fit with a combination of fitting functions including the FWHM of a Gaussian distribution as described previously[17–19]

$$f(x) = a\ exp\left[-\frac{(x-c)^2}{2\sigma^2}\right], \tag{2.32}$$

where a is the scalar intensity, c is the center of the function, and σ is the temporal standard deviation as defined by

$$\sigma = \frac{FWHM}{2(2\ln 2)^{1/2}}. \tag{2.33}$$

A summation of multiple transient components including a fast growth (τ_g) followed by a slow decay (τ_d), a fast decay (τ_1), and a constant intensity plateau. An example of a transient with these components is shown in Figure 2.22.

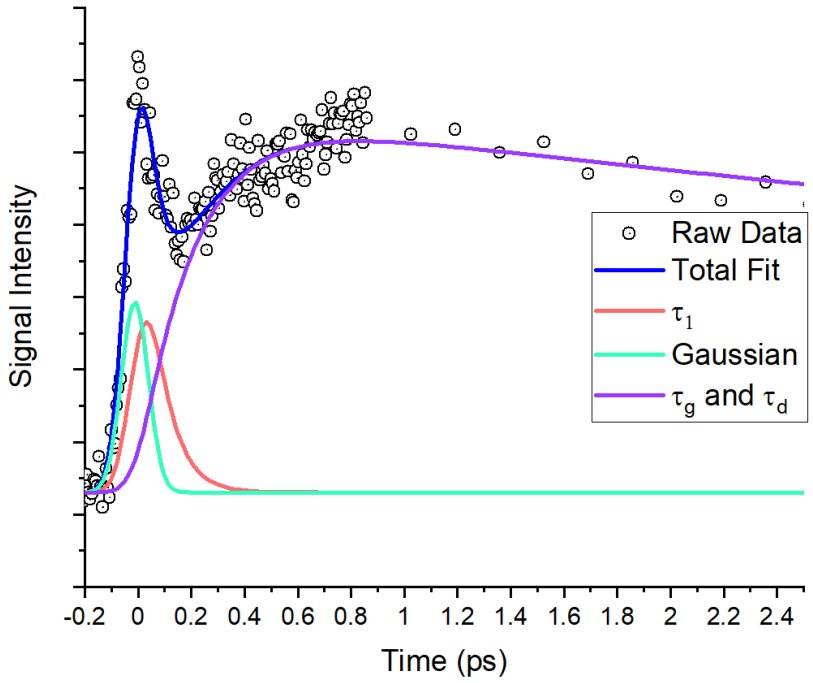

Figure 2.22 Example Fit Showing Multiple Fitting Functions Including a Gaussian (Teal), a Fast Decay (τ1) (Red), a Fast Growth and Slow Decay (τg and τd) (Purple), and the Total Fit (Blue).

Each component is comprised of an exponential decay convoluted to the Gaussian function as given below.

$$I(t,\tau) = a\left[1 - erf\left\{\frac{\sigma}{2\tau} - \frac{t-c}{\sigma}\right\}\right] exp\left\{\left(\frac{\sigma}{2\tau}\right)^2 - \frac{t-c}{\tau}\right\}, \tag{2.34}$$

where $I(t,\tau)$ is the signal intensity of each particular function, a is the amplitude of the fit, t is the time position of the pump-probe delay, τ is the time constant, and c is the center of the Gaussian. In cases where the peaks contain a plateau, the following function is added to the total fit:

$$\lim_{\tau\to\infty} I(t,\tau) = I_p(t) = a\left[1 - erf\left\{-\frac{t-c}{\sigma}\right\}\right]. \tag{2.35}$$

The total fit is found via the summation of all components. In the case of the example fit in Figure 2.22, the total fit in terms of the fast decay, $I_1(t, \tau_1)$, the fast growth, $I_g(t, \tau_g)$, the slow decay, $I_d(t, \tau_d)$, and the plateau, $I_p(t)$, is given by

$$I = y + c_1[I_1(t, \tau_1)] + c_{gd}\left[I_d(t, \tau_d) - I_g(t, \tau_g)\right] + c_p\left[I_p(t)\right], \tag{2.36}$$

where c represents the intensity of each component and τ is the time constant of each component.

2.4.3 Correlation and Covariance Analysis

Often, it is instructive to compare the behavior of multiple peaks within the mass spectrum at once. Covariance analysis, defined as the deviation in two measurements of two distinct species, is used to compare the behavior of one measurement with another via a shot-by-shot changes in the data. This type of comparison allows for the determination of connectedness between two species, in this case the transients of different ions. The covariance between ions, x and y, can be found using

$$C(x, y) = \frac{1}{N}\sum_{i=1}^{N} X_i(x) \cdot Y_i(y) - \left[\frac{1}{N}\sum_{i=1}^{N} X_i(x)\right]\left[\frac{1}{N}\sum_{i=1}^{N} Y_i(y)\right], \tag{2.37}$$

where $X_i(x)$ and $Y_i(y)$ represent intensities of some delay position i for two species x and y. Normalizing this value with respect to the standard deviations of each measurement gives the correlation of the two data sets on a scale of -1 to 1 with -1 being anticorrelated, 0 being no correlation, and 1 being positively correlated. This value, commonly known as the Pearson's correlation coefficient, is found via

$$\rho(x, y) = \frac{C(x, y)}{\sqrt{C(x, x) \cdot C(y, y)}}. \tag{2.38}$$

Here, $C(x, x)$ and $C(y, y)$ are the variances of each species. Results of correlation mapping gives insight into the relationship between transients of different species within a pump-probe experiment.

CHAPTER 3

COMPUTATIONAL METHODS

3.1 Introduction

Experimental research on ultrafast excited states requires an in-depth understanding of their properties. In addition to experimental observation, calculations of molecular properties based on quantum mechanics can shed light on key physical and chemical properties. Such calculations can be done based on numerous approximations and approaches and the choice of methodology depends on the system and properties in question. Within the research presented in this thesis, all computational calculations are based on *ab initio* calculations: those which depend only on quantum mechanics and do use experimental data as parameters. A variety of software packages exist for determining properties of atoms and molecules based on *ab initio* calculations, but the research herein uses Gaussian16. This software is capable of determining a variety of chemical properties such as molecular energies, molecular structures, thermodynamic properties, bond energies, transition states, molecular orbitals, excited states, potential energy surfaces, and much more. This chapter describes the ways in which Gaussian16 was used to glean information on the molecular properties of the molecules of interest and how its outputs were used to develop more rigorous models regarding excited state properties. The majority of the focus will be on how Gaussian16 calculations can be used to understand the energetic properties of molecules, the excited states and their potential energy surfaces, and the topological descriptors of electrons and holes generated via photoexcitation.

3.2 Historical Development of Computational Quantum Chemistry

The fundamental equation of all of quantum mechanics is that of the Schrödinger equation, in which all possible quantum mechanical information is held. The time-independent Schrödinger equation is given as

$$\hat{H}\Psi = E\Psi \tag{3.1}$$

where $\hat{H}$ is the Hamiltonian operator which is acting on the wave-function Ψ to yield the total energy E. For a single particle in three dimensions the Schrödinger equation can be written as

$$\frac{-\hbar^2}{2m}\nabla^2\Psi(r) + V(r)\Psi(r) = E\Psi(r) \tag{3.2}$$

Where V(r) is the potential energy of the particle, and $\frac{-\hbar^2}{2m}\nabla^2$ represents the kinetic energy operator. The ultimate goal of computational quantum chemistry involves solving, or at least approximating, the solution to the Schrödinger equation. However, given the complexity of the wave-function, which for an N electron system with M nuclei, depends on 3N electron spatial coordinates, N spin coordinates, and 3M nuclear spatial coordinates, the Schrödinger equation can only be solved exactly for simple systems, like hydrogen like atoms. Thus, it becomes the goal of computational quantum chemistry to employ a variety of approximations for modeling more complex systems.[20]

3.2.1 Approximations to the Schrödinger Equation

One of the most significant approximations employed in *ab initio* calculations is the Born-Oppenheimer approximation (BOA) which allows for the independent treatment of electrons and nuclei given the comparatively large masses of nuclei relative to electrons.[20] Within the BOA, the electrons are considered to move in the field of fixed

nuclei. A major consequence of fixed nuclei results in the kinetic energy is zero and nucleus-nucleus repulsion is a constant term.[21] Implementation of the BOA allows for the Schrödinger equation to be rewritten with two terms within the Hamiltonian as

$$\left(\hat{H}_{el} + \hat{V}_{nuc}\right)\Psi = E_{el}\Psi \tag{3.3}$$

The electronic Hamiltonian can be expressed in terms of the electron kinetic energy, $\hat{T}$, the electron-nuclear potential energy, $\hat{V}_{nuc-e}$, and the electron-electron potential energy, $\hat{V}_{e-e}$ where, in atomic units,

$$\hat{H}_{el} = \hat{T} + \hat{V}_{nuc-e} + \hat{V}_{e-e} = \frac{-1}{2}\sum_{i=1}^{N}\nabla_i^2 + \sum_{i=1}^{N}\sum_{A=1}^{M}\frac{Z_A}{r_{iA}} + \sum_{i=1}^{N}\sum_{j>1}^{N}\frac{1}{r_{ij}} \tag{3.4}$$

In the above equation, *i* and *j* include all *N* electrons and *A* corresponds to the individual identities of each nucleus *M*. Even within the BOA, solving the Schrödinger equation still remains impossible for all but the simplest of systems. Thus, it becomes critical to employ a systematic method for approximating the lowest total energy of a given system.

3.2.2 Basis Sets

A useful manner for approximating the BOA Schrödinger equation is the construction of basis sets, or a system of equations which can be used to construct functions of interested (such as a wavefunction) through a linear combination of basis functions.[22] If a basis set is complete (i.e., infinite) the exact wavefunction can be written exactly. However, in the absence of an infinite basis set, finite systems of equations are chosen to approximate the properties of interest. The energies of these approximate

solutions (E_ϕ) are determined to be either equal to or higher in energy than the exact solution (E_0): an important mathematical property of systems possessing a ground state, that is termed the variational principle.

There are many types of basis functions, e.g. Slater-type orbitals and Gaussian-type orbitals (GTOs).[21] Within this dissertation, only calculations based on Gaussian-type orbitals are used. Numerous basis sets have been developed and each has its strengths and weaknesses. Each basis set provides a scaling (contraction) coefficient and an orbital exponent for orbital construction. Generalized Gaussian primitives can only approximate the lowest shell for each angular quantum number (i.e., 1s, 2p, 3d, 4f, etc). The generalized Gaussian primitive, $g(\alpha, r)$, can be expressed in terms of principal quantum numbers (n, l, and m) with respect to radial and angular functions as

$$g(\alpha, r) = R_l(r)Y_{lm}(\theta, \phi) = N_g r^{n-1} e^{-\alpha r^2} Y_{lm}(\theta, \phi), \tag{3.5}$$

where α is a positive orbital exponent which is given by the Gaussian16 program, r is the radius of the orbital found by $r = \sqrt{x^2 + y^2 + z^2}$, $R_l(r)$ is a radial component which can be written in terms of a normalization coefficient N_g and the principal quantum number, and $Y_{lm}(\theta,\phi)$ are spherical harmonics used for reconstructing molecular orbital density. N_g can be determined from the follow equation

$$N_g = \left[\frac{2^{2n+\frac{3}{2}}}{(2n-1)!!\,\pi^{\frac{1}{2}}}\right]^{1/2} \alpha^{\frac{(2n+1)}{4}}. \tag{3.6}$$

Spherical harmonics are a functions based on the principal quantum number of atomic orbitals and can be expressed through

$$Y_{lm}(\theta, \phi) = N e^{im\phi} P_{lm}(\cos\theta), \tag{3.7}$$

where,

$$N = \sqrt{\frac{(2l+1)(l-m)!}{4\pi\,(l+m)!}}, \tag{3.8}$$

and $P_{lm}(cos\theta)$ is an associated Legendre function of $cos\theta$.

As Gaussian type functions do not represent electron density accurately, multiple gaussian primitives can be used to construct more accurate, contracted gaussian type orbitals (CGTOs), as a linear combination of individual gaussian primitives following[21]

$$\chi = \sum C_d g(\alpha, r)\,. \tag{3.9}$$

Here, C_d is the contraction coefficient for each gaussian primitive defined by the basis set. These contractions give rise to a more precise atomic orbital (χ) which can be used to construct a full molecular orbital as a combination of atomic orbitals. A full description of a molecular orbital (ϕ_i) can be determined based on the CGTOs as a basis function and found as the summation of molecular orbital coefficients (c_i) and the basis functions (χ) as described by

$$\phi_i = \sum_{\mu=1}^{N} c_{\mu i}\chi_\mu. \tag{3.10}$$

The choice of basis set for a given calculation depends on the system and the parameters of interest. A more thorough discussion of specific basis sets will be addressed in Section 3.2.5.

3.2.3 Hartree Fock Theory

One of the most popular methods for approximating the solution to the Schrödinger equation is the Hartree-Fock (HF) method.[20] The basic approximation employed in the

HF method is to consider that the wavefunction, Ψ_h, for an N electron system, each with r_i degrees of freedom, is given by a single Slater Determinant and is given by

$$\Psi_h = \Phi_{SD} = \frac{1}{\sqrt{N!}} \begin{vmatrix} \phi_1(x_1) & \cdots & \phi_N(x_1) \\ \vdots & \ddots & \vdots \\ \phi_1(x_N) & \cdots & \phi_N(x_N) \end{vmatrix} \tag{3.11}$$

where ϕ_n is a single electron orbital composing a total molecular orbital, and x_i represents the combined product of the spatial and spin electron coordinates. Within this formalism, each orbital is calculated as a one-electron solution describing the motion of an electron in an average field determined by the nuclei and the other electrons in the system. Applying the Hartree-Fock approximation leads to a set of one-electron equations

$$f_i(r_1)\phi_i(r_1) = \varepsilon_i\phi_i(r_1) \tag{3.12}$$

where f_i is the one-electron Fock operator, ϕ_i is the eigenfunction, and ε_i is the eigenvalue of orbital of interest. The Fock operator is based on the kinetic energy of the electron, the nucleus-electron interaction, and the HF potential as shown in

$$f(r_1) = -\frac{1}{2}\nabla^2 - \sum_A^M \frac{Z_A}{r_{1A}} + v^{HF}(r_1) \tag{3.13}$$

The HF potential (v^{HF}) corresponds to the average field experienced by the electron in the orbital, ϕ_i, caused by the remaining electrons in the system. As HF theory only accounts for average electron-electron interactions the electron correlation energy (E_{corr}) can be determined with respect to the HF limit (E_{HF}) and the true energy of the system by

$$E_{corr} = E - E_{HF} \tag{3.14}$$

Applying the variational principle to the HF method involves generation of new orbitals in new fields with every iteration, the approach for minimizing the energy is referred to as the Self-Consistent Field (SCF) theory.[22]

3.2.4 Density Functional Theory and Time-Dependent Density Functional Theory

One method for more accurately determining molecular orbital properties is density functional theory (DFT), which is considered to be an expansion on HF theory which includes electron-electron correlations in the calculations.[21] The fundamental model for DFT was first established by Hohenberg and Kohn (HK).[23] Their theorem states that the ground state electronic energy is completely described by the electron density of the system. The benefit of this can be seen with respect to the wavefunction of an N electron system. While the complexity of the wavefunction increases exponentially with the number of electrons, the electron density remains dependent on only on 3 spatial coordinates for a given spin density, regardless of the total number of electrons. The mathematical proof that the electron density can completely determine the energy of the system is based on three ideas: 1) The integral of the density defines the number of electrons. 2) The nuclei positions can be determined by the cusps of the electron density. 3)The intensity of the cusps defines the nucleic charge. 4) The potential energy determines the electronic density.

With these ideas in mind, the goal of DFT methods is to determine functions which connect energy with electron density.[21] One of the most important translations of DFT theory is the Kohn-Sham (KS) self-consistent field (SCF) methodology. The concept posed by Kohn and Sham in 1965 was that the kinetic energy contribution could be

approximately expressed as a sum of one-electron terms corresponding to non-interaction electrons, which lead to a simplified definition of the exchange and correlation energy.[24] The Hamiltonian is then described as a sum of one-electron operators given as an eigenvalue equation as

$$\left(-\frac{1}{2}\nabla^2 + v_s(r)\right)\phi_i(r) = \varepsilon_i\phi_i(r) \tag{3.15}$$

where $v_s(r)$ is the effective potential in terms of the electron density ($\rho(r)$) and the electron exchange-correlation (XC) potential ($v_{XC}(r)$) defined as

$$v_s(r) = \left[\int \frac{\rho(r')}{|r-r'|}dr' + v_{XC}(r) - \sum_A^M \frac{Z_A}{|r-r_A|}\right] \tag{3.16}$$

The XC potential contains the information required for approximating the unknown XC energy of the system.[21] The XC potential is the only approximation used within KS DFT and the method for approximating this is determined based on the system of interest. Such methods are described in Section 3.2.5. Similar to HF-SCF, calculations using KS-SCF are solved iteratively at each molecular geometry and increases in total energy for a given geometry are rejected while decreases are returned into the calculation until a minimum energy value is reached.

Despite the benefits of DFT over HF, the calculations are limited as they are time-independent in nature. Extension of DFT can be done to include time-dependent properties such as the interaction of a molecule with an external electric field. Such expansion allows for the determination of excited states. This formalism is referred to as time-dependent DFT or TD-DFT. This methodology is based on the HK theorem of time-independent DFT and is based on the Runge-Gross (RG) theorem.[25] This theorem states

that for a given initial wavefunction, there is a unique interaction between the time-dependent external potential and the time-dependent electron density of the system. Employing this theorem leads to the time-dependent KS analogue of Schrödinger equation following

$$\left(-\frac{1}{2}\nabla^2 + v_s(\rho)\right)\phi_i(r,t) = i\frac{\partial}{\partial t}\phi_i(r,t) \qquad (3.17)$$

and v_s is again related to the XC potential of the system but also includes the external potential of the time-dependent field. Use of TD-DFT for determining excited states has direct applications for a variety of spectroscopies including UV/VIS. A useful approximation to TD-DFT, known as the Tamm-Dancoff approximation (TDA) is employed for the research in this thesis. TDA restricts excitations to only transitions between occupied and virtual orbitals and ignores de-excitation transitions.[26] TDA has been shown to be particularly useful for systems with strong coupling between the ground state and first excited state.[27]

3.2.5 Choice of Methods and Basis Sets

As mentioned previously, the only approximation employed in DFT is the approximation of the XC energy and XC potential. Many methods for approximating v_{XC} have been proposed over the years and the most basic is the Local Density Approximation (LDA) which assumes the density is in the field of a uniform electron gas. Following the development of LDA was that of the Generalized Gradient Approximation (GGA) which includes the first derivative of the density as a variable which allows for a more realistic description of a non-uniform electron density.[21] Later it was suggested that a more effective approach would be to include the HF-like exchange

thus creating a hybrid functional which includes fractions of different XC approximations including LDA, GGA, and HF. Perhaps the most commonly used hybrid functional is the "Beck, 3-parameter, Lee-Yang-Parr" or B3LYP method.[21,28–30] As a hybrid exchange functional, it incorporates simpler functional with different degrees of contribution. It also splits the contributions of the XC potential into exchange functions and correlation functions as shown in

$$E_{XC}^{B3LYP} = (1-a)E_X^{LDA} + aE_X^{HF} + b\Delta E_X^{GGA} + (1-c)E_C^{LDA} + E_C^{LYP} \qquad (3.18)$$

Here, the parameters a, b, and c are 0.20, 0.72, and 0.81 for B3LYP specifically.[21]

One error associated with hybrid functionals like B3LYP, especially when using TD-DFT to describe charge transfer, is the inaccurate analysis of long-range interactions. A fix to this is to separate the exchange functionals into short- and long-range parts. The earliest example of this is found in CAM-B3LYP, which is a range separated extension of B3LYP.[31]

Calculations done in this thesis primarily rely on the "Beck, 3-parameter, Lee-Yang-Parr" or B3LYP method, which is the most common of the hybrid exchange functional with the extended 6-311G (++) basis set. 6-311G (++) is a Pople style basis set of the form *k-nlmG*, where *k* dictates the number of primitive GTOs are used for representing the core orbitals and *nml* determines both how many functions are used for the valence orbitals and how many primitives are in each function. B3LYP is a computationally cheap method and can efficiently predict geometries, energies, and electron densities for simple molecules. For more complex systems, such as metal-oxide

clusters, the Coulomb-attenuation method of B3LYP, or CAM-B3LYP is used for its more advanced long-range connection.[31,32]

3.3 Methodology Using Gaussian16

Treatment of molecules within the Gaussian16 software follows the same procedure across each system of interest. First, ground state geometries are optimized and their energies and molecular orbitals are determined. Energetic properties are calculated based on the lowest energy structures of multiple optimizations including that of the neutral ground state, the cation and anion of the ground state structure, and molecular fragments. From these, it is possible to determine the ionization potentials (I_P), the electron affinities (E_a), atomic binding energies (E_b), and bond dissociation energies. A key point of distinction in these calculations comes when considering whether a process occurs vertically (no molecular motion), or adiabatically (involving molecular relaxation). When considering a vertical process, the molecular geometry is locked in its ground state structure and the energies of the ions and fragments are found without molecular motion (i.e., at the minimum electron configuration with respect to the parent species). In contrast, an adiabatic process allows for molecular rearrangement and thus the ions and fragments are optimized to find their lowest energy structure, and this is compared to the ground state structure of the parent molecule.

Both vertical and adiabatic calculations can be done with the following equations. The values for I_P and E_a were determined as the difference between the neutral and cation and anion configurations of the species at the ground state geometry. The binding energy

(E_b) of individual atoms for a particular species is calculated with respect to the energy of the remaining fragment after dissociation and the energy of the parent molecule.

$$E_b = \left(E_{fragment} + E_{atom}\right) - E_{\text{molecule}}. \tag{3.19}$$

Similarly, bond dissociation energies can be found with the energies of the intact molecule and the resulting fragments via

$$E_{bond} = \left(\sum E_{fragments}\right) - E_{molecule}. \tag{3.20}$$

These energetic calculations can shed light on the redistribution of excited state energy into different molecular pathways such as fragmentation and ionization.

Excited state information can be determined through the use of TD-DFT. Again, both vertical and adiabatically relaxed values are determined. To find the geometry of the first excited state, TD-DFT is used to optimize the structure to an energetic minimum with respect to the excited state of interest. Such calculation can be used to determine changes in energy and molecular orbital shapes after the molecule undergoes relaxation.

3.4 Extensions to computational methodology using Home-Built Python Program

The results provided by Gaussian16 were used in a home-built Python program for determining more specific parameters relevant to excited states and charge-transfer. Deconstructing the results of a Gaussian16 calculation allows for additional, more specific, calculations to be done. By taking the energy and molecular orbital information, more specific details of the excited states can be determined. The following describes the Python program and its capabilities for use with the output of Gaussian16 calculations.

3.4.1Molecular Orbital and Excited State Information

By using the formalism of GTOs and basis sets it is possible to reconstruct the molecular orbitals from the results of the Gaussian16 calculation. The home-built Python program reads in weighting values for each atomic orbital from the output of a Gaussian16 calculation and uses them reconstructions a system of spherical harmonics based on the equations presented in Section 0. Summing over the relative weights of each atomic orbital gives a complete molecular orbital. The ability to reconstruct molecular orbital within a home-built program allows for increased capabilities and flexibility for modeling excited states.

Calculation of excited states requires time-dependent density functional theory (TD-DFT), which is an advanced form of DFT, and the output of these calculations reports the energies and properties of excited states. For more complex systems with long-range charge-transfer characteristics, the Tamm-Dancoff approximation of TD-DFT is more accurate.[33] In complex molecules with many orbitals, the excited states are often linear combination of molecular orbitals. Gaussian16 output files provide a specific transition from an occupied orbital to an unoccupied orbital with a weighting parameter. If the excited state is made up of multiple transitions, the sum of these transitions and their weighting parameter is calculated.

3.4.2 Excited State Topology

Once the relevant structures have been optimized in an *ab initio* computational program and the molecular orbitals have been configured, it is possible to calculate a variety of topological parameters for evaluating molecular and cluster properties.

Electronic properties can be compared between the ground state and the excited state molecules following optimization. Such energetic descriptors of excited states include the optical gap (O_{gap}), the fundamental gap (F_{gap}), and the exciton binding energy (E_x). The O_{gap} is defined as the minimum photon absorption energy required to produce an excited electron−hole pair and is often less than the HOMO/LUMO gap given that excited states are formed from a combination of molecular orbitals. The F_{gap} is defined as the energy required to generate an excited electron and hole that do not interact:

$$F_{gap} = I_P - E_a, \tag{3.21}$$

and the E_x is the difference between F_{gap} and O_{gap} and is calculated as

$$E_x = I_P - E_a - O_{gap}. \tag{3.22}$$

Because photoexcitation involves contributions from many occupied and virtual orbitals, it is convenient to represent the distribution of the electron and hole as their transition densities. The transition densities for the electron and hole were determined using

$$\rho_e(\boldsymbol{r}) = \sum_{o,v} c_{o,v}^2 \varphi_v^2(\boldsymbol{r}), \tag{3.23}$$

where ρ_e is the electron transition density at point r, φ represents the spatial wave function of a molecular orbital, $c_{o,v}$ is the contribution coefficient for each pair as provided by the Gaussian16 excited state calculation, and the subscripts o and v stand for the occupied and virtual pairs involved in the excitation. The hole density, $\rho_h(\boldsymbol{r})$, is found similarly except using $\varphi_o(\boldsymbol{r})$. From the electron and hole densities it is possible to determine topological descriptors, such as d_{eh} (distance between centroid of the electron and hole densities),[34,35] σ (degree of delocalization of the RMS density of the electron and

the hole), and Λ (percent overlap of the electron and hole wave functions) as analytical tools. The centroid of the electron and the hole is found following

$$X_e = \int x\, \rho_e(r) dr, \tag{3.24}$$

where X_e is the centroid position for the x value of the electron. Similar equations are used for *y* and *z* coordinates. The d_{eh} is calculated via

$$d_{eh} = \sqrt{(d_x)^2 + \left(d_y\right)^2 + (d_z)^2}, \tag{3.25}$$

where $d_x = |X_e - X_h|$. The σ values for the electron and hole are

$$\sigma = \sqrt{\int (r - R)^2 \rho(r) dr}\,, \tag{3.26}$$

where *R* is the distance from the centroid value for the electron or hole. Large σ values indicate delocalized orbitals.[34] The Λ parameter, which quantifies the degree of overlap between the wave functions, is found

$$\Lambda = \frac{\sum_{o,v} c_{ov}^2 O_{ov}}{\sum_{o,v} C_{ov}^2}\,, \tag{3.27}$$

where O_{ov} is the overlap between each occupied virtual pair and is found following

$$O_{ov} = \int |\varphi_o||\varphi_v| dr\,. \tag{3.28}$$

The Λ parameter ranges between 0 and 1 to describe the percent overlap of the wave functions and is indicative of the degree of charge transfer of the excited state where a small Λ value indicates a long-range charge transfer excitation.[36,37]

These topological parameters are found using the home-built python program which uses the results of Gaussian16 calculations to provide further insight into the

behavior of electrons and holes in excited states. These calculations are particularly useful for modeling excited states in semiconducting materials such as metal-oxide clusters where excited states are determined by the electron donor and acceptor atoms within the molecule. This is demonstrated more thoroughly in Chapter 5.

3.4.3 Potential Energy Surfaces

Evaluation of excited state properties with respect to vibrational motion is critical for understanding relaxation dynamics within complex potential energy surfaces (PES). Such surfaces can be multi-dimensional with respect to numerous molecular qualities such as bond length, bond angle, and torsion angle. Simplified potential energy surfaces with only one degree of freedom, referred to as a potential energy curve, are calculated with respect to vibrational motion of a specific reaction coordinate, most often the internuclear distance between two atoms in a molecule. In these calculations, a two-dimensional curve is created for each excited state showing changes in energy with respect to the reaction coordinate.

When creating a PES for a reaction coordinate, the excited state information is calculated at a variety of points along a reaction coordinate. For example, if the reaction coordinate is chosen to be the bond distance between atoms A and B ($r_{A\text{-}B}$) in a polyatomic molecule, the ground state geometry is found for the molecule and then all other atomic coordinates are locked with respect to A and B except the distance between the two, essentially freezing the molecule and only varying the coordinate of interest. An array of data points along the reaction coordinate (internuclear separation) are used and at each point and, for each point, the relevant excited states are calculated. The energies of

each state are then returned and used to create a curve of energy versus internuclear separation. An example of the use of PES is given in Chapter 4.

3.5 Summary of Calculations

The following chapters include a variety of methods for modeling the geometry, energetic properties, and excited state characteristics of the species of interest. The types of calculations chosen were done with respect to the species of interest and the dynamics observed experimentally. In smaller molecules such as alkyl halides, the potential energy curves with respect to C-X bond provides insight into the relaxation dynamics of the excited states. In semiconducting species such as metal-oxide clusters, the interest is on the properties of the electron and hole generated via photoexcitation. As will be shown, the use of computational modeling is fundamental in understanding the excited state dynamics of molecular species and their relaxation dynamics.

CHAPTER 4

DETERMINATION OF RYDBERG LIFETIMES OF n-BUTYL BROMIDE

4.1 Introduction

The fragmentation of the C-X (X = Cl, Br, I) bond in alkyl halides has long been studied as a prototypical example of photodissociation.[38–47] Furthermore, photofragmentation of alkyl halides presents an atmospheric threat given the ozone depletion effect of halides.[48,49] Detailed investigation of alkyl halides ranges from experimental determination of dissociation energy, computational modeling of the potential energy curves of the C-X bond, and time resolved spectroscopy for determination of the timescale of dissociation. Most prior studies have focused on CH_3-X given its relative simplicity.[38,50–54] The dissociation is known to proceed via multiple channels including the lowest energy repulsive state (A state) which splits based on spin orbit coupling leading to X (J=3/2) and X* (J=1/2) fragments. In alkyl halides, Franck-Condon (FC) excitation to the A band requires ~6 eV, but the C-X dissociation energy is ~3 eV, leaving excess energy in the form of kinetic energy release of the fragments and residual energy within the photofragments which is distributed internally throughout the vibrational modes of the molecule through intramolecular vibrational energy redistribution (IVR). In methyl halides, the residual energy is primarily translated into vibrational modes of CH_3^+. As the carbon chain increases in length, the molecular degrees of freedom leading to a higher rate of vibrational redistribution of the excited state energy. Long alkyl structures inefficiently convert excess energy to the translational

motion of photofragments and therefore exhibit increased internal excitation with alkyl size.[55,56]

At energies higher than the A state exists a series of bound Rydberg states. Exciting to the 5s Rydberg states, in alkyl halides, leaves the molecule in the bound B and C states which undergo internal conversion into the repulsive A state on the order of ~1.5 ps.[52,56–62] In alkyl iodides, internal conversion to the A state depends on the length of the alkyl chain such that the intersection of the A and B states occurs closer to the Franck-Condon (FC) region leading to faster crossing times with increasing carbon chain length.[56] The A state dissociation times depend on the structure of the alkyl halide with branched isomers having shorter time scales for dissociation.

Another important mechanism in C-X bonding occurs via ion-pair formation from the 5p Rydberg state. Ion-pairs are bound states of the scheme A^+/B^- at a larger internuclear separation than the neutral AB species. Ion-pair formation has garnered significant attention for decades. In particular, alkyl halides are known to possess ion-pair states with dissociation energies below the adiabatic ionization energy of the molecule given the large electron affinity of halogens.[63] The ion-pair states exist at longer C-X bond distances and as such cannot be accessed directly through FC excitation. Instead, the potential energy curves of these molecules show a strong interaction between the Rydberg states and the ion-pair states indicating these states are populated via predissociation (i.e., dissociation from the Rydberg states) from the FC region into the ion-pair state.[59,64,65] Despite the significance of ion-pair formation dynamics, the direct observation of ion-pair formation via tunneling from Rydberg states is limited.

Femtosecond (fs) time-of-flight mass spectrometry was used to track the dynamics of the E and V states of HBr and DBr and determined the lifetime of ion-pair formation to be 10 ps.[66] However, dynamics of ion-pair formation in larger alkyl halides have only been studied indirectly and no lifetime have been measured.[52] Larger alkyl groups stabilize the ion-pair state[56], and it is predicted the bound E ($^1\Sigma^+$) Rydberg states have much longer lifetimes as relaxation either occurs by tunneling to the ion-pair state or relaxing through conical intersections.

Here, fs time-of-flight mass spectrometry enables us to track the photodissociation dynamics of n-C_4H_9Br via multiple fragmentation pathways, including the direct dissociation via the A band in 149 fs and ion-pair formation via predissociation from the 5p Rydberg states over 10.8 ps. Despite extensive research on the dissociation of C-X, little attention has been paid to the dissociation of C-C and C-H bonds leading to the formation of C=C and C≡C bonds. Fs laser irradiation of alkanes produced 1-D carbon chains (linear carbon chains)[67–70] and carbon nanoparticles[71] but little to no work has studied the dehydrogenation in real time. Herein we use bromobutane (n-butyl bromide) as a paradigm for understanding C-Br, C-H, and C-C scission as well as the formation of H_2 and C=C and C≡C bonds.

4.2 Methods

Transient dynamics were measured using a previously described[72] home-built Wiley-McLaren[73] type time-of-flight mass spectrometer (TOF-MS). A sequence of sub-35 fs laser pulses from a Ti:sapphire laser were employed to measure the excited state lifetimes of an effusive n-butyl bromide vapor sample, maintained at $1x10^{-6}$ Torr. Mass

spectra were recorded using 400 nm (3.1 eV) as a pump pulse and ionized with an 800 nm (1.55 eV) probe pulse. The 400 nm pump intensity is 5.6 x 10^{14} W/cm^2 and the 800 nm probe pulse intensity is 6.5 x 10^{13} W/cm^2. A 3-photon excitation with 400 nm (3.1 eV) pump beam accesses Rydberg states and the 800 nm probe beam samples the fragment population distribution as a function of time delay through strong-field ionization. Mass spectra were collected over 400 averages in time steps of 20 fs between –500 fs and +600 fs, and then with 100 fs timesteps to 50 ps. Transient signals were fit using a combination of exponential functions convoluted with a Gaussian function as described previously.[72] As the laser pulses separate in time, the ion signal intensity is proportional to the populations of the fragments in the excited states.

The lowest energy structures of n-C_4H_9Br and its fragments were optimized using density functional theory (DFT) and the B3LYP method with the 6-311G++ ([12s6p/5s4p] for C, [6s1p/4s1p] for H, and [16s14p5d/9s8p2d] for Br) basis set in the Gaussian 16 software package.[74] The ionization potentials (IPs) and minimum thermodynamic appearance energies were calculated. To capture the ion-pair state, it is necessary to go through a system of coupled equations to go beyond the one potential treatment. EOM-CCSD/6-311G++ calculations were performed to obtain the PES. The basis set is augmented with diffuse functions (++) for better treatment of Rydberg states. The remaining coordinates were frozen at the ground state geometry. The energies of the states along the C-Br PES represent an upper limit to their energies as movement along other coordinates may lower the energy. Note that spin-orbit coupling is neglected in these calculations and only singlet states are considered.

4.3 Results and Discussion

At temporal overlap, the largest ion signals are recorded (Figure 4.1) due to non-resonant excitation/ionization. The mass spectrum from fs laser ionization resembles the pattern produced from electron impact.[75] Photodissociation of n-butyl bromide (C_4H_9Br) (I_P = 10.17eV) leads to many fragments of various degrees of saturation and chain lengths. Photodissociation of n-butyl bromide (C_4H_9Br) involves three types of bonds (C-Br, C-C, and C-H). Intramolecular vibrational energy redistribution (IVR) is likely important in both the neutral and ionic states. Three photon excitation reaches the n → 5p Rydberg state where the dominant decay mechanism is predissociation to hot neutral fragments with C-C activated dissociations.[59] The largest signal in the mass spectrum corresponds to $C_4H_9^+$ (*m/z* = 59) (I_P = 7.78 eV). All ions that contain a Br atom, including the two peaks for the parent molecule at *m*/*z*=136 and 138, show the typical Br isotopic distribution ($^{79}Br/^{81}Br$:51%/49%). A relatively strong pump energy is required to clearly see the dynamics associated with Rydberg states. Under such experimental conditions, some of the parent molecules are ionized by the pump pulse alone, through the absorption of 4 x 400 nm photons, resulting in a background signal for the parent and fragment masses at all time delays. At positive time delays (when 400 nm pump precedes 800 nm probe), several of the larger ions decrease, while the intensity of the smaller fragments increases due to ion fragmentation by the probe pulse. No multiply charged ions were recorded with the laser intensities employed. The probe beam is kept below threshold intensity so that no signal is observed with just the 800 nm beam. Neither H nor H_2 are recorded, due to their high I_Ps of 13.6 and 15.5 eV, respectively.

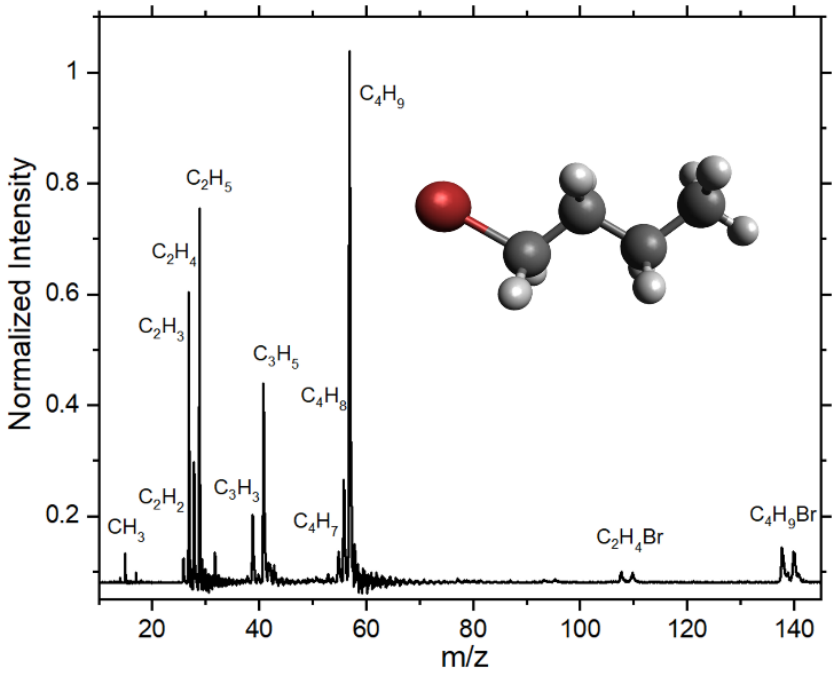

Figure 4.1 The Mass Spectrum of n-Butyl Bromide as Ionized at Temporal Overlap with Sub-35 fs 400 nm (5.6 x 10^{14} W/cm^2) and 800 nm (6.5 x 10^{13} W/cm^2) Laser Pulses.

The formal symmetry group of C_4H_9Br is C_s, but its excited states are similar to the well-known HBr because its Rydberg series arise from the Br lone pair orbitals which are relatively unaffected by the carbon chain, enabling a reasonably good interpretation of the electronic spectrum to be achieved by approximating it as a local diatomic $C_{\infty v}$ C-Br molecule (or C_{3v} as CH_3Br). The calculated PESs for the neutral ground X ($^1\Sigma^+$ for $C_{\infty v}$) and excited states corresponding to the C-Br bond coordinate are shown in Figure 4.2. Our calculations show that the A state ($^1\Pi^1$ for $C_{\infty v}$), arising from the valence excitation of an electron into the antibonding orbital ($\pi \rightarrow \sigma^*$), is purely dissociative for C-Br bond cleavage and is accessible with 2 x 400 nm photons. Two valence states are separated by the spin orbit splitting into the Br and Br* states. However, previous A state measurements demonstrated little difference between the lifetimes for the spin states.[51,55]

The s-Rydberg states reside around 7 eV, and have been previously described as B and C states ($^1\Pi$ for $C_{\infty v}$), which are $n\pi \rightarrow 5s\sigma$ Rydberg states. At higher energies, a dense distribution of p-Rydberg series appear, in agreement with literature results for similar molecules.[52,76] The $5p_{z\sigma}$ (or $5p_a$) and $5dz^2$ states lie higher in energy and are well separated from the $5p\pi$ (or $5p_e$) states. The D state ($^1\Pi$ for $C_{\infty v}$) is $\pi \rightarrow 5p\sigma$ Rydberg state. The Rydberg energies show little dependence on carbon chain length.[77] The Rydberg potentials closely follow the $C_4H_9Br^+$ PES as the bond is provided in both cases by the same pair of a_1 valence electrons and, therefore, have minima at slightly shortened distances compared to the neutral. The p-Rydberg states, arising from a $n\pi \rightarrow 5p\sigma$ and, $n\pi \rightarrow 5p\pi$ excitation, are expected to have unperturbed Rydberg character as no valence states of these symmetries are in the energy region under consideration.

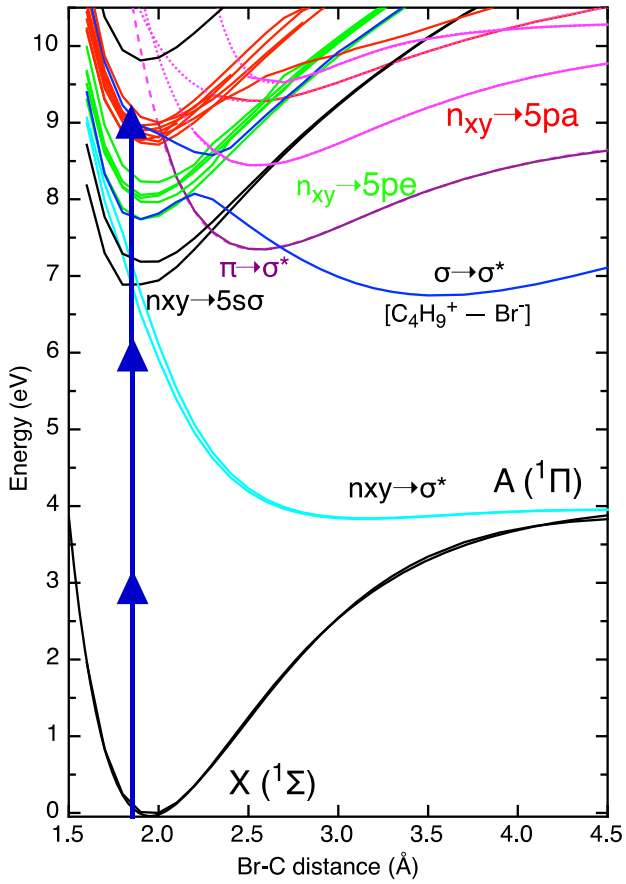

Figure 4.2 The Lowest 20 Potential Energy Surfaces Along the C-Br Bond Coordinate. The Pump Photon Energies are Shown as Vertical Blue Arrows.

Avoided crossings between the bound Rydberg and repulsive valence states of the same ($^1\Sigma$) symmetry give rise to a state with double-minimum PES, termed "ion-pair" or [$C_4H_9^+$ – Br^-] state. We examine the nature of the ion-pair state, created by the mixing of two electronic states (Figure 4.3). At short distances, the $n_z \rightarrow 5p\pi$ excitation corresponds to a Rydberg E ($^1\Sigma^+$) state of the n_z band ($\pi \rightarrow 5p\pi$) with a shallow minimum at ~1.9 Å and an electron configuration of $(\sigma)^2(\pi)^3(\sigma)^0 5p\pi$. As the distance increases, it transforms into a valence, or V, state ($^1\Sigma^+$) which is better described as a $\sigma \rightarrow \sigma^*$ transition having an electron configuration of $(\sigma)^1(\pi)^4(\sigma^*)^1$, effectively reducing the bonding order by 1 and

therefore lies at longer distances. The PES of the V state has a larger internuclear separation (R_{min} = 3.5 Å) than the Rydberg states associated with the X $^3\pi$ ground core of the molecular cation (e.g., the Rydberg states involved in this work). At longer distances, the PES develops a positive slope that represents the Coulomb attraction between ions. Therefore, the calculated (E/V $^1\Sigma^+$ state) contains two local minima, and closely resembles the PES calculated for methylbromide[52] and HBr.[78]

Ion-pair thresholds are typically high in the vacuum ultraviolet (VUV) spectrum and below the direct IP.[58,59,63–66,76,79–84] Since the dominant interaction for ion-pair states of halogen-containing molecules is Coulombic at large internuclear separations, these states are similar, having large equilibrium C-X internuclear separations (3.0-3.5 Å). The energy required to form the ion-pair is found via

$$E_{(A^+,B^-)} = D_0(AB^+) + IP(AB) - E_A(B), \quad (4.1)$$

where D_0 is the dissociation energy of the cation species, IP is for the parent molecule, and E_A is for the anion.[59] The energy for the ion-pair of [CH_3^+–Br^-] was found to be 9.5 eV and 8.15 eV for [$C_2H_5^+$–Br^-].[64,85] We calculate the ion-pair energy for n-butyl bromide to be 7.1 eV, consistent with the trend of ion-pair formation energy of alkyl halides decreasing with carbon chain length. It should be noted that none of the Rydberg states are dissociative, but all states above the s-Rydberg states contain sufficient energy to enable ion-pair formation. The energy of the ion-pair in HBr is calculated to be ~9.5 eV.[78]

Crossings between states are heavily dependent on the degree of electronic coupling between states. The strong coupling between the E and V states in n-butyl

bromide indicates the transition proceeds adiabatically given the large energetic separation (~0.6 eV) of the diabatic crossing and the adiabatic avoided crossing (Figure 4.3).

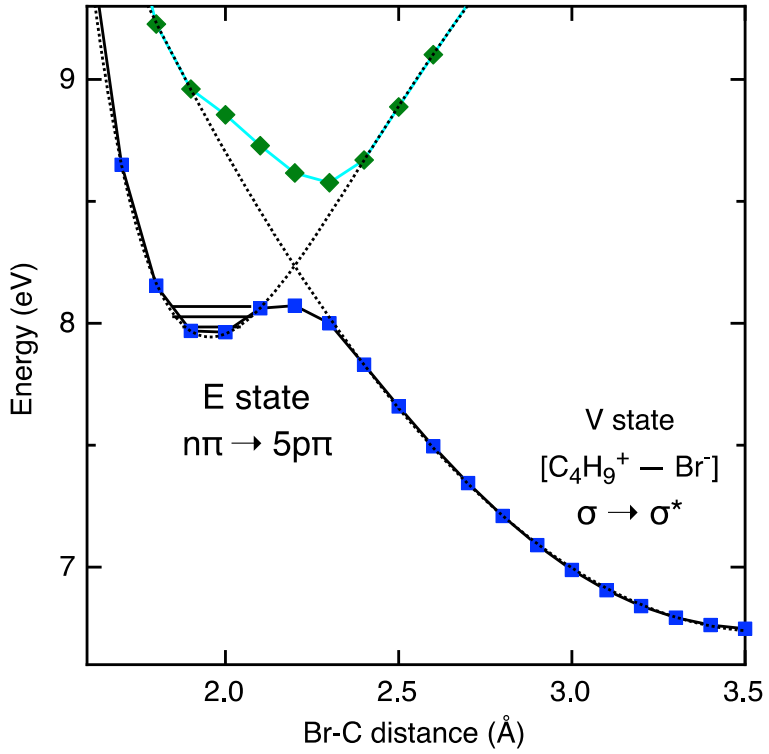

Figure 4.3 The Diabatic (Dotted) and Adiabatic (Solid) Potential Energy Curves of the 5p Rydberg States and the Ion-Pair States. A Morse Potential Fit was Used to Extrapolate the Data Points to Obtain the Diabatic States.

An additional $^1\Pi$ state is found with a minimum bond distance of 2.5 Å that corresponds to the non-bonding orbital of the carbon backbone [HOMO-3] being excited to the antibonding orbital [LUMO] and is therefore a $\pi \rightarrow \sigma^*$. This effectively nonbonding state has a minimum bond length between the Rydberg states (effectively bond order =1) and the ion pair state (effective bond order = 0). This state has not been explored previously as it cannot exist in HBr and is much higher in energy in smaller carbon

chains such as CH_3Br. However, this state could be important in VUV photodynamics of alkyl chains.

The parent molecule relaxes from FC-region into the Rydberg state within 10s fs, and then within 1 ps undergoes internal conversion (IC) and releases at least ~2.3 eV into vibrational energy. At short time delays, the probe beam interacts with the intact molecule in the Rydberg states, exciting it into a cation state. Proton dissociation and unsaturated hydrocarbon ions decay with lifetimes of ~600 fs, suggesting that they are ionized directly from the Rydberg states prior to IC. The cation state facilitates fragmentations at lower relative barriers and the deprotonation energies are smaller in the cation state.

4.3.1 C-Br Dissociation Pathways

4.3.1.1 Direct Dissociation from the A State

At positive time delays (400 nm precedes 800 nm), the intensities of the larger (lower energy) ions are decreased ($C_4H_9Br^+$, $C_4H_9^+$, and $C_4H_8^+$), while the intensity of the smaller (higher energy) fragments are increased due to fragmentation of the parent ion by the probe pulse. Therefore, each of the ions analyzed here contains a plateau function recorded in the transient data to represent signal with lifetimes longer than the 60 ps recorded in the experiment. For example, the $C_4H_9^+$ signal is observed at all times due to direct ionization and dissociation from the 400 nm beam. The $C_4H_9^+$ is reduced at positive times as the 800 nm beam further excites the ions into higher energy fragmentation channels. Negative time delays are not influenced because the 800 nm beam is not intense enough to cause ionization. The sub-ns transients occur on neutral excited states.

The dominant fragmentation pathway for n-butyl bromide is through the loss of the weakly bound Br atom. Several mechanisms contribute to this dissociation, including direct A state dissociation and ion-pair formation, but they operate on different timescales allowing each to be measured. Thus, the $C_4H_9^+$ and $C_4H_8^+$ transient signals serve as markers for the C-Br dissociation mechanisms (Figure 4.4). The complimentary fragment ion signals (Br and HBr) both display only weak Gaussian temporal signals due to differences in electronegativity. The transient signal recorded for $C_4H_9^+$ contains features that display several mechanisms. Dissociation via the A state occurs on the femtosecond timescale given the steep slope of the PES. The signal is affected in both positive and negative time due to resonance with the A state but presents in complimentary signals. In negative time delays (when the 800 nm beam arrives first), an increase in A state dissociation is accessed through rapid formation of C_4H_9 via direct dissociation by 800 nm and subsequently ionized by the 400 nm beam. The signal grows with a lifetime (τ_g) of 172 ± 16 fs (Figure 4.4) and remains constant for long time delays (beyond 60 ps). However, the $C_4H_9^+$ transient signal in the positive time delays (when 400 nm arrives first) decays with a lifetime (τ_d) of 149 ± 26 fs. This signal demonstrates that the probe beam can ionize the initially excited A state. Two photons from the 400 nm beam excite the A band and induce dissociation. If the 800 nm probe beam were sufficiently intense to ionize the dissociated C_4H_9, the $C_4H_9^+$ signal would rise and remain as a long-lived plateau, rather than decay with the lifetime of the A* state. Instead, the signal decreases and is attributed to the weak probe beam monitoring the changing IP of the neutral C_4H_9 fragment as it traverses along the PES for the A state. Thus, measurements of $C_4H_9^+$ from

two separate laser pulse sequences provide similar values for the lifetime of the A state and within error of one another. Average of the two measurements provides the A state lifetime of 160 fs, in agreement with similar alkyl halides.[55]

The parent molecule $C_4H_9Br^+$ transient only represents states which undergo ionization without dissociation. The $C_4H_9Br^+$ also decays with a lifetime of 161 ± 30 fs in the positive direction, demonstrating that the metastable A state can be directly ionized by the 400 nm probe beam prior to dissociation.

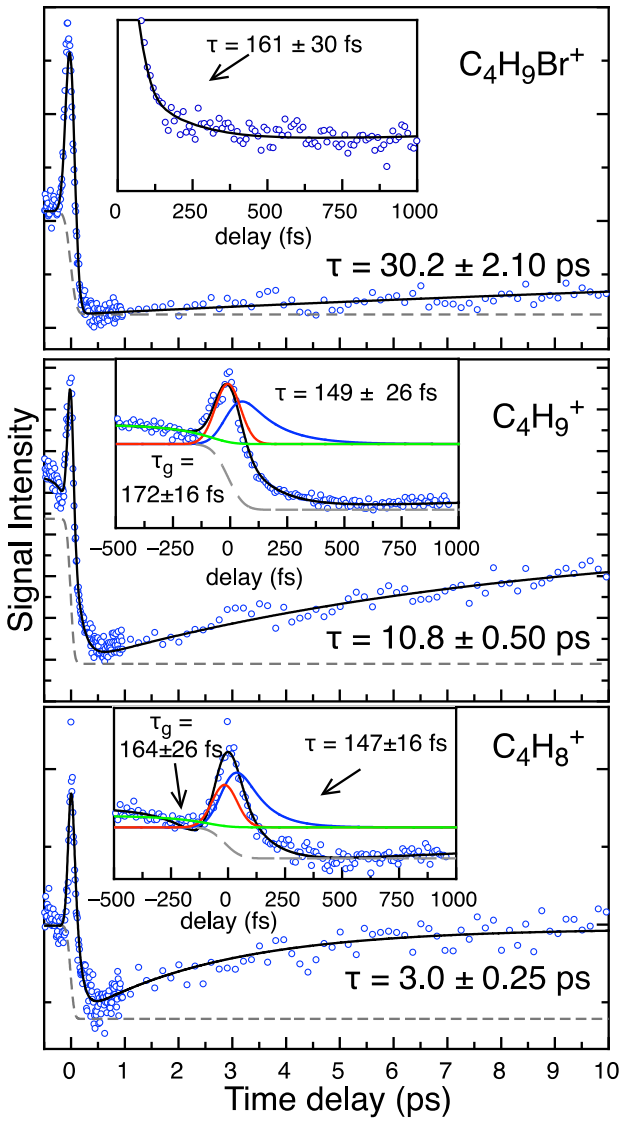

Figure 4.4 The Integrated Transient Signals for $C_4H_9Br^+$, $C_4H_9^+$, $C_4H_8^+$ Recorded at Laser Intensities of 5.6 x 10^{14} W/cm^2 for the Pump (400 nm) Pulse and 6.5 x 10^{13} W/cm^2 for the Probe (800 nm) Pulse Demonstrating the Slow (10s of ps) Ion-Pair Formation and the Faster (100s of fs) A State Dissociation. The Dashed Gray Plateau Function Represents the Long-Lived Signal Due to Cation Dissociation. The Insets Show a Truncated Temporal Window for Each Transient Signal Highlighting the Femtosecond Dynamics Associated with A State Dissociation. The Red Line Represents the Gaussian Function, Blue for Positive Decay and Green for Negative Growth Transients.

Dissociation of C-Br into Br and C_4H_9 (1-butyl) requires only 2.91 eV (shown in Figure 4.2 as 4 eV, but relaxation along the chain reduces the energy), but 2 x 400 nm

photons (6.2 eV) are required to access the A state, leaving 3.29 eV of excess energy that is distributed between kinetic energy and vibrational motion of the photofragments. Given the length of the butyl chain, a significant proportion of that energy is converted into vibrational motion along the C-C backbone. As the A state $C_4H_9Br^*$ relaxes, 3.29 eV (~2 probe photons) of energy is converted into kinetic energy, reducing the ionization efficiency of the probe beam. The $C_4H_9^+$ transient signal arises from the dissociative ionization of $C_4H_9Br^*$ molecule by the probe pulse directly on the A band prior to its decay. Once dissociated, the probe pulse is insufficient to ionize C_4H_9 (IP =7.78 eV).

$C_4H_8^+$ formation requires the removal of both H and Br and is facilitated by nuclear rearrangement. The β elimination of HBr cannot be captured by the PESs represented in Figure 4.2. The transient signal for $C_4H_8^+$ (IP = 5.81 eV) is similar to $C_4H_9^+$, with a growth in negative time delays ($\tau = 164 \pm 26$ fs) and a decay in the positive timescales ($\tau = 147 \pm 16$ fs). The like behavior both lifetimes and signal transient implies that $C_4H_8^+$ also arises from the A band. The $C_4H_8^+$signal has a similar decay lifetime and suggests it is also produced from A state dissociation. We calculated the reaction coordinates, specifically the release of HBr, to have an activation barrier of 2.18 eV and enthalpy of reaction of 0.60 eV. HBr formation through β-elimination induces a contraction and double bond formation along the C_1-C_2 coordinate resulting in a bond length for the transition state 1.41 Å, compared to the molecule's ground state distance of 1.52 Å. This bond further compresses forming the double C=C bond product of C_4H_8 (1-butene) with a bond length of 1.34 Å (Figure 4.5). This concerted pathway requires less energy than a sequential process involving the loss of Br with 2.91 eV followed by the

lowest energy proton (2^{nd}-C) removal which requires an additional 1.72 eV (not shown) and is therefore unlikely. Despite requiring a slower Br separation, the lower activation energy barrier enables this mechanism to be competitive and produce 20% that of direct dissociation. The flexible carbon chain absorbs some of the photoexcitation energy, slowing the A state dissociation and enabling this proposed β-elimination mechanism (Figure 4.5).

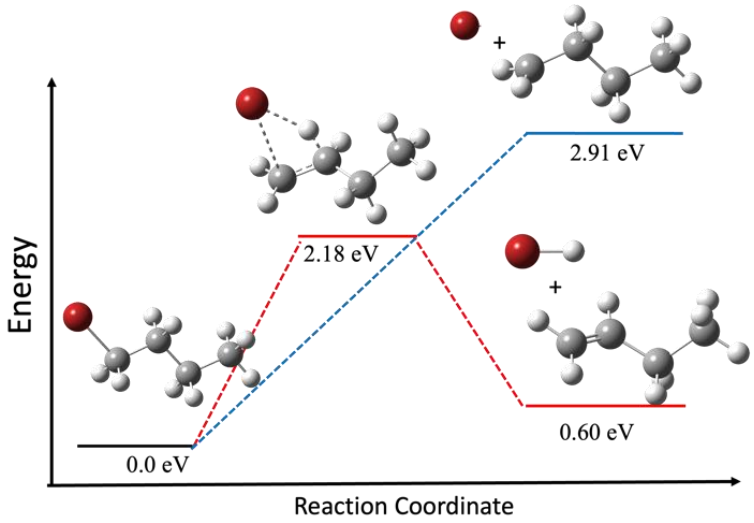

Figure 4.5 Reaction Coordinate Diagram Showing the Energies of the Direct Br Dissociation from the Parent Molecule and the Lower Energy Concerted β-Elimination Mechanism for HBr.

4.3.1.2Ion Pair Formation

Direct access to the ion-pair state is not feasible given the poor FC overlap with the ground state. Instead, access to the ion-pair state requires significant nuclear motion and is achieved via predissociation from the Rydberg states manifold. Absorption of 2 x 400 nm photons leads to direct dissociation on the A state on the femtosecond timescale as shown earlier. Upon absorption of 3 x 400 nm photons, C_4H_9Br is excited to the $5p_a$-Rydberg series in the FC region, as shown in Figure 4.2. Several states cross between the

$5p_a$ and $5p_e$ Rydberg states, including the higher adiabatic state formed from the avoided crossing between the ion-pair and Rydberg state. Predissociation into the V state may occur via tunneling from the E Rydberg state or through decay from the p_z Rydberg states. This state couples with the p_e Rydberg series having minima around 8 eV and enabling adiabatic conversion into the ion-pair state. Alternatively, tunneling between the E (R_{min} = 2.0 Å) to the V state (R_{min} = 3.6 Å) separates the molecule into the [A^+–Br^-] ion-pair. The shallow PES has a barrier is ~ 0.10 eV supports 3 vibrational energy levels (Figure 4.3) and enables tunneling to the ion-pair state on the 10s of ps timescale, similar to previous measurements of HBr.[78] The newly defined nonbonding PES crosses into the p_a Rydberg series. Movement along the carbon chain may enable the PESs to meet. Further relaxation from the V state to lower energy states is improbable because the repulsive walls have much shorter internuclear distances.

Evidence for the p-Rydberg mediated predissociation mechanism is provided by increases in the ion signals on the ps timescale. $C_4H_9^+$ gradually increases over 10.8 ± 0.17 ps (Figure 4.4) reflecting the relaxation from the initially prepared p-Rydberg state and formation of the ion-pair state. This ps timescale is far too slow to be attributed to the direct dissociation on the A state. It is also nearly an order of magnitude slower than suggested for internal conversion from the B/C (s-Rydberg) states (~ 1 ps) from measurements[56] of similar alkyl halides. Finally, as mentioned previously, the probe beam does not have sufficient energy to ionize a free C_4H_9 fragment on the A band, meaning the 10.8 ± 0.17 ps growth in $C_4H_9^+$ must be attributed to the neutral that lies higher in energy. Relaxation from the 5p Rydberg states to the dissociative A state is unlikely as

they do not overlap in energy. The [$C_4H_9^+$–Br^-] ion pair state lies 3 eV higher than the A state (assuming a frozen C chain) and has already undergone the charge transfer. Molecules that achieve the extended ion-pair state through charge transfer are stable, allowing the signal to demonstrate a long-lived plateau function in our experiments. The ion pair is subsequently separated by the 800 nm probe beam enabling $C_4H_9^+$ to be recorded. Thus, the 10.8 ± 0.17 ps growth is attributed to the formation of the ion pair through Rydberg state enabled predissociation. A similar timescale for ion-pair formation was recorded in HBr.[66,79]

Similarly, $C_4H_8^+$ also presents a ps growth indicating its formation following the relaxation of the p-Rydberg states. However, the C_4H_8 formation of is significantly faster, with a growth lifetime of 3.0 ± 0.25 ps compared to the ion-pair formation time of 10.8 ± 0.17 ps. The ps growth is an order of magnitude slower than the direct dissociation from the A state revealing that nuclear reorganization occurs. The β-elimination process can only occur while the Br remains nearby and therefore must occur faster than ion-pair formation, while the Br is within range to attract the proton. This rapid growth demonstrates that HBr elimination through β elimination occurs during the transition between the p-Rydberg state and predissociation into the ion-pair state. The $C_4H_8^+$ signal remains roughly 20% that of intensity of $C_4H_9^+$, demonstrating the relative branching ratio between direct ion pair formation and β-elimination of HBr.

Finally, there is evidence that a proportion of the molecules relax without undergoing ion-pair separation. As mentioned, the parent ion signal decreases in positive times, as absorption of the 800 nm probe beam induces dissociation of the cation signal

prepared by the 400 nm beam. However, in addition to the long plateau, the transient signal for $C_4H_9Br^+$ also grows with a lifetime of 30.2 ± 2.1 ps. The probe beam is unable to ionize out of the ground state, meaning that this signal must arise from an intact parent molecule that remains electronically excited. The electronic state also cannot be related to the A band as it is well established to be dissociative. It also is unlikely to reside in the s-Rydberg states, due to the propensity for internal conversion into the A band. Therefore, the minor 30.2 ± 2.1 ps growth in $C_4H_9Br^+$ is attributed to the small proportion of molecules that relax to the stable D-state by IVR. E ($^1\Sigma^+$) Rydberg state relaxation either occurs by tunneling to the ion-pair state or relaxing through conical intersections. This intact D-state formation is not efficient and instead a significant portion of the intact parent molecule transitions into the ion-pair state.

4.3.2 Rydberg Enabled C-C Dissociation

Adiabatic relaxation via IC produces vibrationally hot products that undergo secondary fragmentation before ionization by the probe pulse. Thus, the C_4 chain is sufficiently activated for multiple fragmentation pathways. The timescales for IC from the Rydberg state into backbone dissociative channels are recorded as growth lifetimes (τ_g) of the fragments. Excitation above 8 eV (p-Rydberg states) activates C-C stretching which enables additional fragmentation pathways that operate slower than the direct C-Br dissociation. Bond dissociation energies along the chain are similar, creating competition between several pathways that produce both smaller and less saturated hydrocarbons. The many degrees of freedom for the molecule enable competition between multiple fragmentation channels. This process is further emphasized by the electron and hole

densities for each excited state. The lower lying states are primarily centered on the Br and C_1 atoms and is defined by a transition from the two highest occupied orbitals to the two lowest unoccupied orbitals. However, beyond 8 eV, the entire molecule is involved in the excitation with significant electron and hole density along the entire backbone. Furthermore, these excited states are a more complicated linear combination of several orbitals beyond just the highest energy HOMOs and lowest energy LUMOs.

Calculation of the minimum energy of formation for each fragment was done using the optimized structures of each fragment as described in Chapter 3 and the energies are reported in the first column of Table 4.1. The bolded fragment is the ion being detected in the mass spectrum. As shown in the table, formation of unsaturated hydrocarbons requires the most energy for formation given the strength of C-H bonds. The table also lists the relative fragment intensity in the mass spectrum at temporal overlap. Although most energies correlate with the relative intensity (i.e., low energy leads to higher ion signal), some of the more unsaturated hydrocarbons break this pattern. These calculations and the non-linear relationship between signal intensity and energy of formation highlight the complexity of fragmentation pathways. Such pathways are not solely dependent on thermodynamics alone but are driven kinetically.

Table 4.1 Energy Required for the Creation of Cationic Fragments and Their Relative Intensities in the Mass Spectrum.

Fragmentation Pathway from C_4H_9Br	**Required Energy (eV)**	**Relative Intensity**
→ $\mathbf{C_4H_9^+}$ + Br	10.69	1.04
→ C_4H_9 + $\mathbf{Br^+}$	16.64	0.00
→ $\mathbf{C_4H_8^+}$ + HBr	10.02	0.269
→ C_4H_8 + $\mathbf{HBr^+}$	16.02	0.00

→ **$C_4H_7^+$** + H_2 + Br	11.06	0.137
→ **$C_3H_7^+$** + CH_2Br	11.66	0.110
→ C_3H_7 + **CH_2Br^+**	12.64	0.088
→ **$C_3H_5^+$ + HBr + CH_3**	11.75	0.440
→ **$C_3H_3^+$ + H_2 + HBr + CH_3**	14.55	0.203
→ **$C_2H_5^+$** + C_2H_4Br	11.69	0.756
→ C_2H_5 + **$C_2H_4Br^+$**	11.53	0.101
→ **$C_2H_4^+$ + C_2H_5 + Br**	14.13	0.299
→ **$C_2H_3^+$ + C_2H_5 + HBr**	13.53	0.604
→ **$C_2H_2^+$ + Br + H_2 + C_2H_5**	17.47	0.124
→ **CH_3^+** + C_3H_6Br	13.61	0.133
→ CH_3 + **$C_3H_6Br^+$**	13.46	0.00

All C-C bonds have a dissociation energy > 3 eV, with C_1-C_2 being the highest in energy (3.82 eV), followed by C_3-C_4 (3.72 eV), and the lowest being C_2-C_3 (3.35 eV) Dissociation of the highest energy bond, C_1-C_2, produces C_3H_7 and CH_2Br, which are both weak in the mass spectra, despite their relatively low energies of formation, suggesting this pathway has a low probability. $C_3H_7^+$ can only be formed through this mechanism. Although thermodynamically accessible, its reaction rate is small compared to other channels (hence kinetically limited).

Fragmentation along the C_2-C_3 bond (3.35 eV) produces C_2H_4Br (2-bromoethyl) and C_2H_5 (ethyl radical). $C_2H_5^+$ is intense in the mass spectrum while $C_2H_4Br^+$ is weak due to secondary dissociation of the Br atom from the neutral (0.37 eV). These ions contain similar I_P of 8.18 and 8.33 eV, and a combined residual energy of 5.65 eV.

The C_3-C_4 dissociation is common in butane,[86,87] producing CH_3 and C_3H_7. Here, this channel produces C_3H_6Br which is distinctly lacking in the mass spectra. The C_3-C_4 dissociation energy is 3.72 eV. Although C_3H_6Br is stable, $C_3H_6Br^+$ dissociates HBr

without barrier allowing $C_3H_5^+$ to serve as a marker of the intermediate along the pathway. The bromopropyl radical has a small barrier to ring formation (0.043 eV) and undergoes a concerted Br-elimination and ring-closure reaction to form cyclopropane within 7.8 ps (observed through the decay of $C_3H_5^+$) and shown in Figure 4.6. The final products are not ionized/recorded, but the reaction is followed through the growth and decay of the intermediate. The neutral 1- bromopropyl radical can undergo several reactions channels, but our calculations reveal that they have higher energy barriers and are therefore less favorable. Further, the 7.8 ps lifetime shows a relaxation process that is too slow to be attributed to proton removal Figure 4.7. The Br-roaming pathway leads to the β elimination pathway, which on the neutral bromopropyl radical requires a transition state of 2.27 eV which is the highest energy pathway and is unlikely. Thus, C_3H_5 is not an expected neutral product.

A similar ring closure mechanism and timescale of bromopropyl radical was previously proposed from dibromopropane, with remarkably similar ring closure lifetime.[46] The similar dynamics indicate that both molecules retain nearly identical vibrational energy following the primary dissociation. Thus, the primary dissociation removes the vibrational energy from the carbon backbone. In our case the molecule loses a CH_3, and in the previous experiment a Br atom was ejected. The primary dissociation is coherently ejected, keeping all the energy confined to one bond coordinate, and suggests that IVR doesn't occur in either molecule. The initial bond breaking from dibromopropane takes 2.86 eV and was pumped with ~8eV, leaving ~5 eV of energy. In our system, the pump is 9.3eV, and the C_3-C_4 fragmentation takes 3.72 eV, leaving a

nearly equal 5.58 eV residual energy to the products. Considering the CH_3 vs Br sibling product, we predict the lighter/floppier CH_3 fragment to retain more of the residual energy from the dissociation and therefore make a slower ring closure and therefore a longer lifetime in our system.

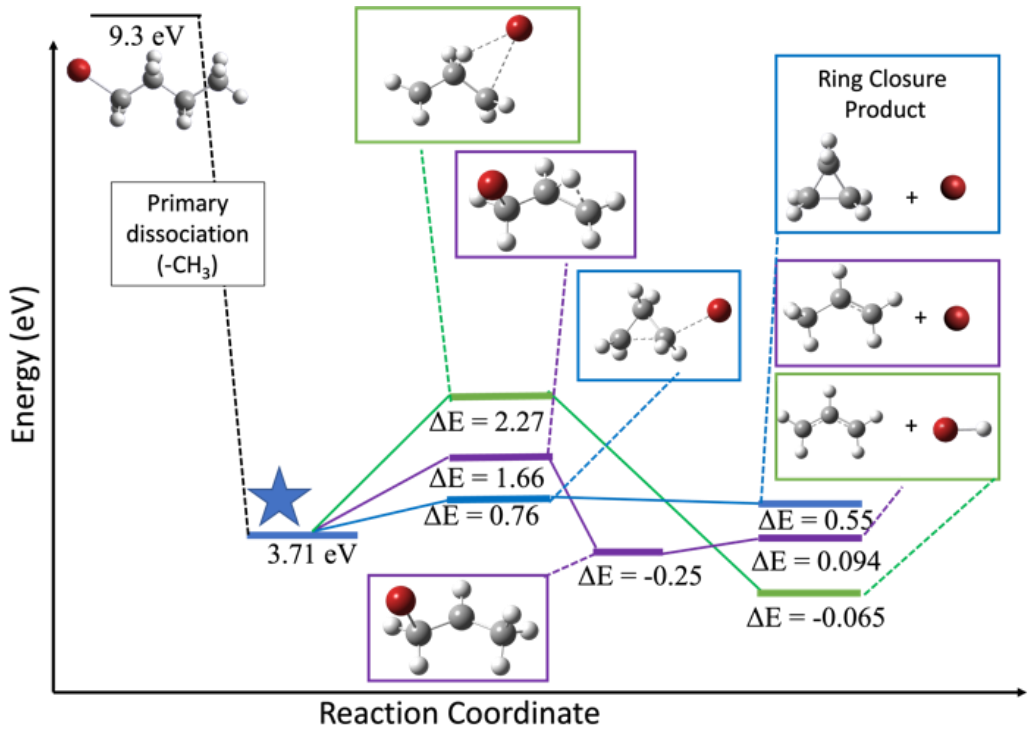

Figure 4.6 Transition States of the 1-Bromopropyl Radical into Multiple Products Including the Highly Stable Ring Closed Product. Here the Star Indicates the Intermediate State Accessed Through Excitation from the Pump Photons.

CH_3 (τ_1 = 600 fs) is not a prominent fragment but may form through direct C_3-C_4 fragmentation or through secondary hydrocarbon fragmentation. Its high I_P (9.8 eV) hinders observation. The sub-ps decay lifetime reveals that it appears from directly probing out of the Rydberg state rather than through IC, and therefore its lifetime is a metric of the lifetime of the Rydberg state.

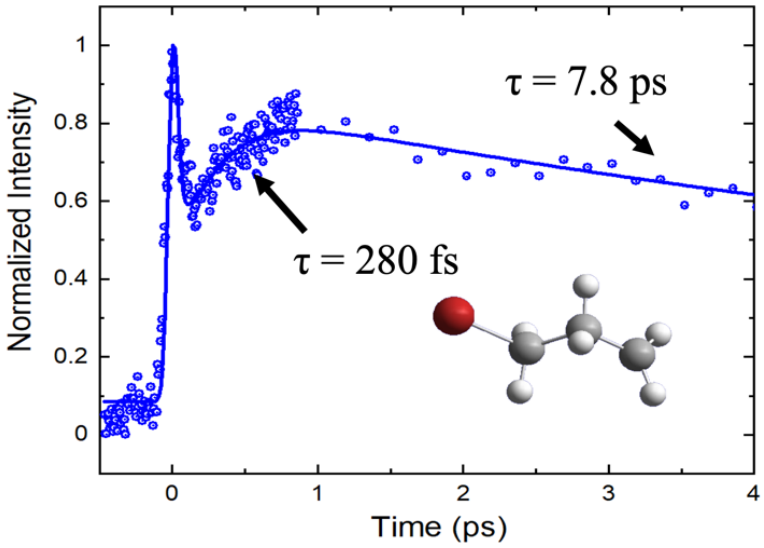

Figure 4.7 Transient of $C_3H_5^+$ Showing the Lifetime for Ring Closure.

4.3.3 β Elimination

Changes in intensity of the pump beam leads to a higher population of the molecules in the Rydberg manifold which have sufficient energy to undergo β elimination. The relative populations of the states leading to β elimination can be estimated through the κ value of the characteristic lifetime of each peak and is defined as the intensity at 600 fs vs the intensity at temporal overlap for each fragment and are reported in Table 4.2. The intensity at 600 fs is near the peak of the growth in saturated hydrocarbon fragments after IVR. The change in intensity between powers for each peak is similar across all fragments. At high laser intensities, the more saturated hydrocarbon fragments exhibit a growth which corresponds to a decay of the unsaturated hydrocarbon fragments. These lifetimes are similar across the propyl and ethyl fragment groups (Table 4.2) indicating β elimination only occurs before IVR. Significant population starts in the higher energy states producing H_2 which quickly (~600 fs) relax (Figure 4.8). The power

dependence confirms that the loss of H_2 occurs from the Rydberg state accessed at higher energies, and not the A state.

Table 4.2 Transients (τ) and Their κ Values for the Propyl and Ethyl Fragments at High and Low Laser Intensities. κ Values Represent the Weight of the Transient with Respect to the Non-Resonant Intensity at Time Zero.

Fragment	τ (fs)	High Power κ	Low Power κ
C_3H_7	585 ± 40	0.72	0.35
C_3H_5	663 ± 64	0.77	0.37
C_3H_3	625 ± 62	0.44	0.24
C_2H_5	593 ± 79	0.86	0.39
C_2H_4	604 ±181	0.57	0.32
C_2H_3	510 ± 98	0.45	0.27
C_2H_2	433 ± 168	0.43	0.24

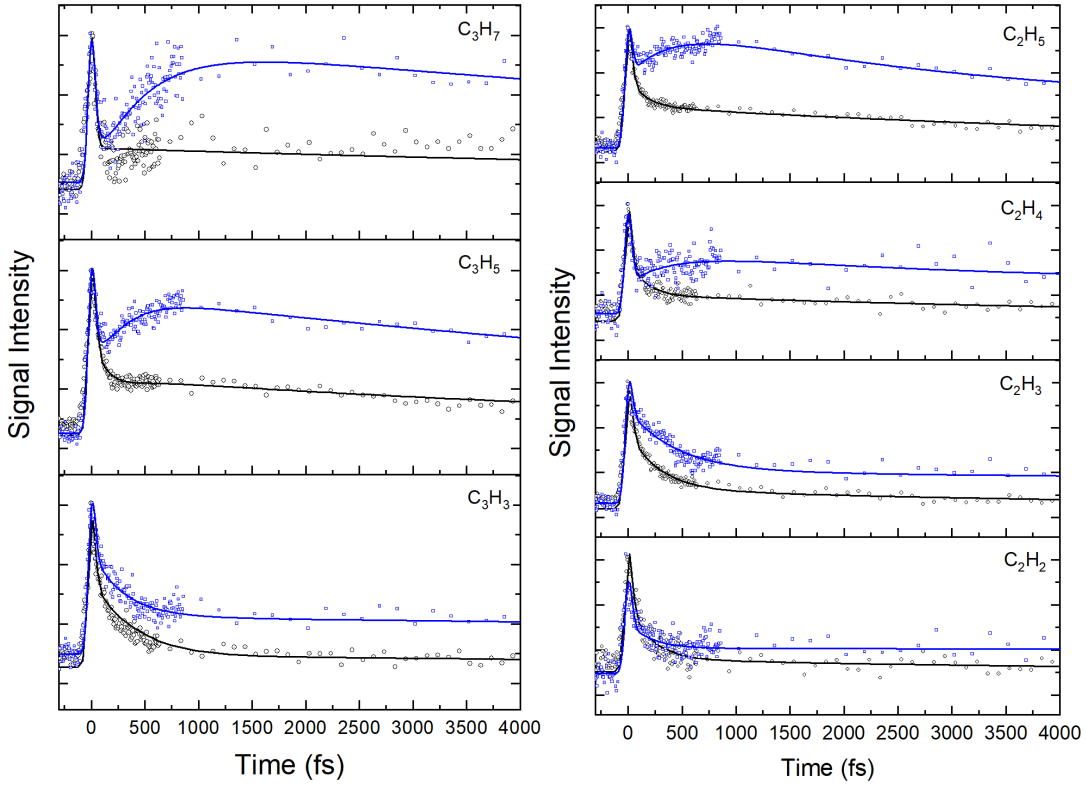

Figure 4.8 Transient Dynamics of the Ethyl (Left) and Propyl (Right) Fragments at High (Blue) and Low (Black) Laser Intensities. The Larger, More Saturated Fragments Show a Clear Growth Matching the Decay of the Smaller, More Unsaturated Hydrocarbons.

Correlation analysis of the hydrocarbon fragments also reveals this trend in fast β elimination before IVR and a growth in saturated hydrocarbons after IVR has occurred. The correlation maps shown in Figure 4.9 (high power) and Figure 4.10 (low power) were taken over a time delay from 100 fs to 600 fs to capture the dynamics associated with β elimination while also avoiding the non-resonant peak at temporal overlap. At low powers, the ethyl fragments are positively correlated with one another and anticorrelated with C_4H_9 and C_4H_9Br ($C_{x,y}$ = -0.75). At high power, the relationship changes such that C_2H_5 and C_2H_3 are anticorrelated revealing a relaxation from the unsaturated fragment to the saturated one. The growth in C_2H_5 (593 fs) closely follows the decay in C_2H_3 (510 fs). At high power, C_3H_5 and C_2H_5 ($C_{x,y}$ = 0.75), and C_3H_3 and C_2H_3 ($C_{x,y}$ = 0.75) are correlated to each other but anticorrelated to the different saturation counterparts ($C_{x,y}$ = 0.20). This result shows the difference in excited state lifetimes is dependent on type of bond cleavage with C-H happening at the highest energy and relaxing over the fastest time scale. C-C fragmentation occurs at lower energy and exists are an intermediate state with a much longer lifetime.

At low pump power, C_3H_5 and C_3H_3 are correlated with each other and anticorrelated with both C_4H_9 and C_4H_9Br. However, at high pump intensity, the τ_1 region of C_3H_5 and C_3H_3 are anti-correlated with one another, indicating a relaxation from the high-energy state producing C_3H_3 into the lower energy state responsible for C_3H_5. The rapid decay of $C_3H_3^+$ matches the growth of $C_3H_5^+$ which suggests the molecule loses the extra 0.5 eV associated with this dissociation. At high pump

intensities, the growth in C_3H_5 becomes more pronounced, making it clear that it is an intermediate in a multiple level relaxation mechanism.

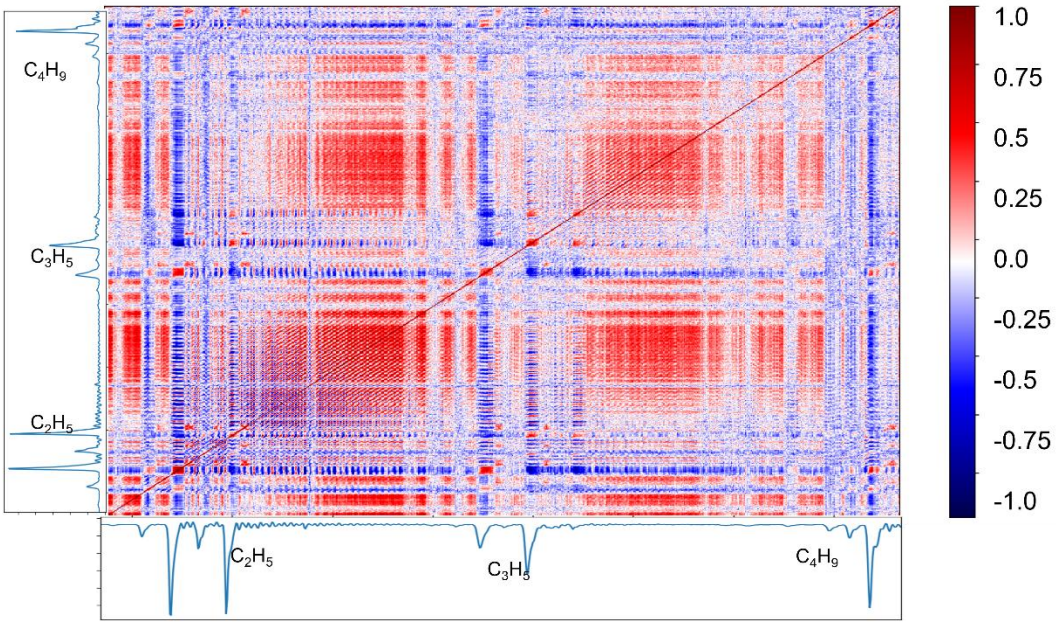

Figure 4.9 Correlation Map of the Hydrocarbon Fragments Taken at High Laser Intensities. Red Indicates Positive Correlation Between Fragment Transients While Blue Indicates Negative Correlation Between Fragment Transients.

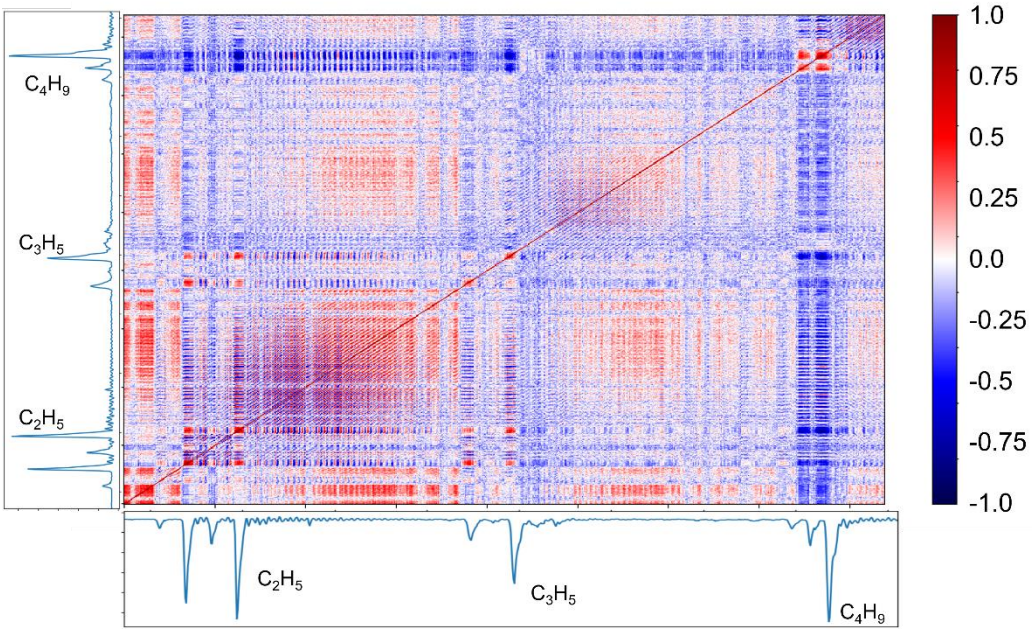

Figure 4.10 Correlation Map of the Hydrocarbon Fragments Taken at Low Laser Intensities. Red Indicates Positive Correlation Between Fragment Transients While Blue Indicates Negative Correlation Between Fragment Transients.

As can be seen from Table 4.1, the difference in energy of formation between saturated and unsaturated hydrocarbons is ~3 eV regardless of carbon chain length. Given that the lifetime of β elimination is consistent across chain length as well, it demonstrates the time required to dissipate 3 eV of energy into vibrational motion.

4.4 Conclusion

The photofragmentation of Br-butane and lifetimes of the Rydberg, V, and E excited states have been measured. Three distinct pathways relating to bond fragmentation (C-Br, C-C, and C-H) where C-Br occurs immediately upon excitation and this state persists for 30 ps. Dissociation of the A state requires 2 x 400 nm photons and has a lifetime of 160 fs. Three photon excitation puts the molecule in the bound 5p Rydberg state which is coupled to the ion-pair V state. Tunneling to the V state takes 10.8 ps. Predissociation from the E state leads to the formation of HBr and H_2 + Br and their

lifetimes are associated with the lifetimes of the Rydberg manifold. An unexplored π-σ* potential energy curve is found in the energetic neighborhood of the ion pair state. This state could be important in VUV photodynamics. Cracking of the carbon backbone occurs via dissociative states. Loss of H and formation of higher order C-C bonds occurs at high energy dissociative states which quickly relax into an intermediate state leading to saturated carbon backbone fragments.

CHAPTER 5

OXYGEN DEFICIENCIES IN TITANIUM OXIDE CLUSTERS AS MODELS FOR BULK DEFECTS

5.1 Introduction

Titanium oxides, especially titanium dioxide (TiO_2 or titania), are versatile materials that are widely used in industrial processes given their relative abundance and low toxicity.[88,89] Bulk titania has garnered significant attention for its role as an active n-type semiconductor in dye-sensitized solar cells,[90] as an environmental cleaning agent through photoreduction of organic pollutants,[91] as a catalyst in water splitting,[92] and as a prominent white pigment in industrial products.[93] Titanium oxides are the archetypal strongly correlated material, meaning their electronic properties are strongly connected to the local geometric structure. Photoexcitation produces an electron and hole pair (exciton) that is responsible for redox photocatalytic reactions. The charge carriers are often accompanied by lattice vibrations that are collectively known as polarons. Polaron formation and related self-trapped exciton formation have a strong impact on the photoactivity of titania.[94] Small polaron formation occurs spontaneously in perfect lattices and is enhanced near defect sites, which can trap mobile carriers at recombination centers, decrease their mobility, and affect the overall activity of the material.[94–96]

The most studied polymorphs of TiO_2 are anatase and rutile, which both have tetragonal crystal structures and contain Ti^{4+} coordinated to six O^{2-} ions.[88,89,97] In the bulk, the reactivity and catalytic properties are driven by changes in the phase, size, and defect concentration. Despite its wide usage, the photoapplication of TiO_2 is limited by its large bandgap of 3.0 eV for the rutile structure and 3.2 eV for the anatase structure.[93] This high bandgap impedes their use to only a fraction of the sun's emission spectrum. In practice, less than 10% of solar radiation has sufficient energy to participate directly in photocatalysis. Defect engineering has been a prominent research focus for tailoring the electronic, magnetic, optical, mechanical, and quantum properties and is crucial for activation of heterogeneous photocatalytic processes.[89,98] In an effort to utilize more of the sun's visible spectrum, increased attention has been invested in the synthesis of titania materials containing large numbers of defect sites, including black TiO_2 and the Magnéli phase.[94,98–110]

The introduction of defects produces structural distortions in the local symmetry of metal centers, thus influencing both charge transport and recombination during the photocatalytic process.[89,99,109,111,112] Black TiO_2 contains point defects that enable it to absorb a large section of the visible spectrum enabling an increased photocatalytic behavior compared to pristine TiO_2.[89,108] The point defects in black TiO_2 have been shown to produce localized states below the conduction band, valence band upshifts, and both conduction band and valence band tails.[89] These defects not only lower the bandgap relative to pristine TiO_2 but reduces charge carrier recombination by acting as trap sites.[113] Magnéli phase refers to ordered O-deficient TiO_2, i.e. Ti_nO_{2n-1} where $n = 4-9$,

with Ti_4O_7 being the most reduced.[98,107] In contrast to disordered defect sites, the Magnéli phase is an ordered form of reduced titania and is characterized by planar defects.[114] Magnéli phases are desirable as they exhibit a high electrical conductivity that is comparable to carbon.[114] Both black TiO_2 and Magnéli phase materials contain large fractions of O defect sites (and related Ti^{3+} sites) which act as the active sites for catalytic activity.[115] Despite the increased absorption of reduced titania in the visible region, a precise understanding of the structural and electronic nature of these catalytically active sites remains elusive. The number and signature of spin active Ti^{3+} sites surrounding O defects are thought to be the dominant contributing factor responsible for the different catalytic performance of reduced titania.[89,102,116] O vacancies lead to localized electrons near the defect site and the degree of localization directly depends on the bonding strength versus the possibility of crystal lattice distortion to a different bonding environment.[117]

The energetic, geometric, and charge carrier effects caused by O vacancies dramatically change the photoabsorptive and photocatalytic properties of TiO_2. Therefore, a thorough understanding of the effect of O vacancies on the behavior of excitons, polarons, and free charge carriers (electrons and holes) in titania is needed. The localization and stabilization of 3d electron character on reduced Ti remain elusive and are critical for understanding the role of defects in transport phenomena. Moreover, it is not clear if the excess electron density fully localizes on a single Ti ion or if it is delocalized over several sites. Gas-phase clusters can be employed as models for the point defects in bulk systems to reveal how local changes in geometric structure influence

dynamics and charge transport. The atomic precision of clusters provides specific information on what factors enable polaron formation, which is known to lower electron transport of TiO_2 nanotubes, nanofilms, nanoparticles, and bulk materials.[94,102]

Furthermore, clusters have been used as models for reactivity including water splitting and hydrolysis.[118,119] Work within this thesis has used both stoichiometric (Ti_nO_{2n}) and sub-stoichiometric (Ti_nO_{2n-x}) clusters as models for characterizing excited state properties and the effect of oxygen vacancies in bulk materials. The work herein presents the experimentally determined excited state lifetimes and relevant descriptors of excited state properties for explaining cluster behavior.

5.2 Methods

Neutral clusters were produced by the ablation of a Ti rod using the second harmonic of a Nd:YAG laser while synchronized to a pulsed beam of 1% O_2 seeded in He. The neutral cluster distribution was subsequently measured using a home-built Wiley−McLaren[15] type time-of-flight mass spectrometer coupled to a fs laser (<35 fs) for ionization. Detailed information on the experimental setup is found in Chapter 2. Briefly, the ionic clusters produced through laser ablation are deflected from the fs laser pulse interaction area through the use of electrostatic fields. Neutral clusters are ionized using temporally overlapped 400 nm (3.1 eV) and 800 nm (1.55 eV) pulses from a Ti:Sapphire laser at intensities of 9.9×10^{14} and 3.1×10^{15} W/ cm^2, respectively. In the absence of specific cross section information, the cross sections of the clusters are assumed to be similar. Thus, although cations are ultimately measured from this interaction, the signal intensity of the ions in the mass spectra is representative of the population of the neutral

cluster distribution. Titanium oxide cluster (Ti_nO_{2n}, Ti_nO_{2n-1}, and Ti_nO_{2n-2}) geometries were optimized at the density functional theory (DFT) level within the Gaussian 16 software suite[74] using the CAM-B3LYP36 functional and 6-311G++(3d2f, 3p2d) [(15s11p6d/10s7p4d) for Ti and (12s6p/5s4p) for O] basis set (Figure 5.1). The excited state properties were calculated within the Tamm−Dancoff approximation[26] to time dependent DFT (TD-DFT). The lowest energy spin configurations of neutral stoichiometric clusters are all singlets; however, the majority of Ti_nO_{2n-1} compounds are triplets and Ti_nO_{2n-2} compounds form quintet spin states. Topological descriptors for the first excited state were calculated for the ground state and first excited state geometries and compared against the same analysis of the stoichiometric clusters.[127] We employed topological descriptors, such as d_{eh} (distance between centroid of the electron and hole densities),[34,35] σ (degree of delocalization of the RMS density of the electron and the hole), and Λ (percent overlap of the electron and hole wave functions) as analytical tools. Finally, the binding energy of each oxygen atom with respect to the original cluster was determined. The exact methodology for these calculations is described in detail in Chapter 3.

5.3 Results and Discussion of Stoichiometric clusters

All clusters contain two terminal O atoms bound to a tetrahedral Ti atom, in agreement with literature assignments for the global minimum structures of $(TiO_2)_n$.[27,128–135] The stable conformations of clusters n > 4 possess all tetra-coordinated Ti atoms (Figure 5.1). Odd numbered clusters adopt C_s symmetry and even clusters adopt C_{2v} or C_{2h} symmetry. Stoichiometric $(TiO_2)_n$ are characterized as closed shell systems, where

each O atom withdrawals two d-electrons from the Ti atoms, leaving the cluster void of d-electrons. Photoexcitation moves an electron from the occupied O 2p orbitals back to the unoccupied Ti 3d orbitals, analogous to the band structure of bulk TiO_2 (Figure 5.1). The cluster's ionization potentials (IPs) and optical gaps have not been experimentally measured but were calculated to be ~10.0 ± 0.5 eV[129] and ~4.5 eV,[27] respectively. These results are consistent with photoexcitation by two pump photons (6.3 eV).

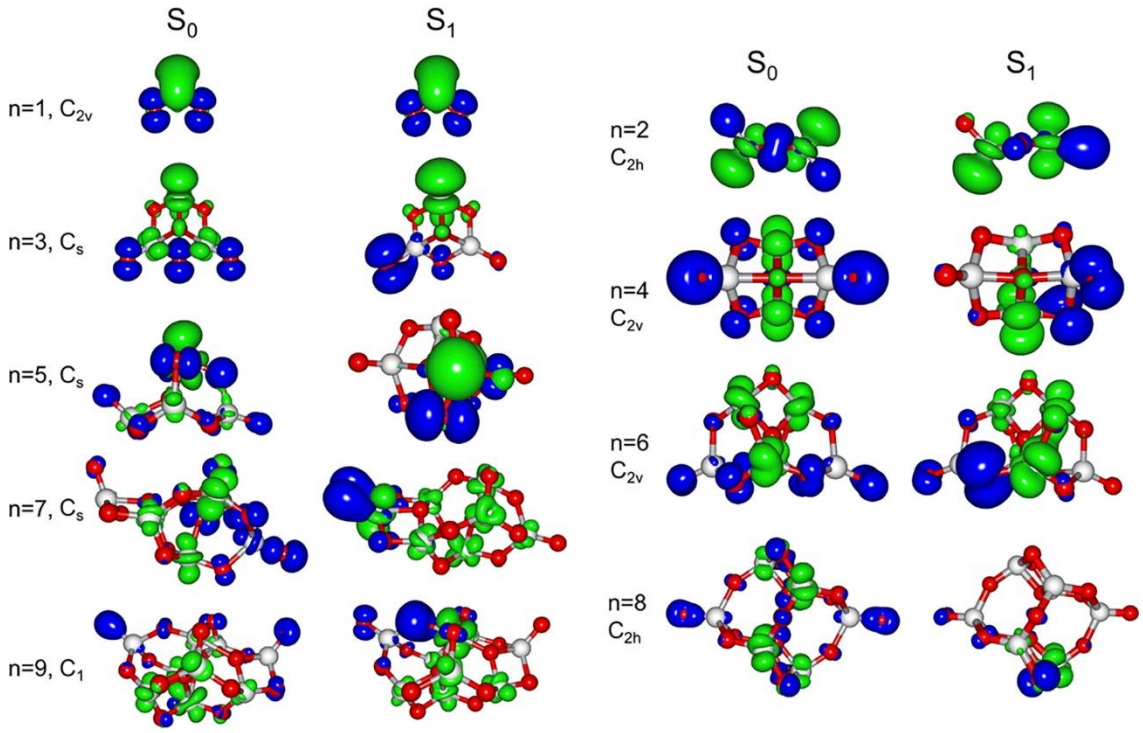

Figure 5.1 TD-CAM-B3LYP S_0 and S_1 Transition Densities for $(TiO_2)_n$, (n = 1–9), Presented at an Isodensity of 0.002/Å^3. The Electrons are Shown in Green, the Hole is in Blue, Titanium Atoms are White, and Oxygen Atoms are Red.

The probe beam is maintained at threshold intensities to ensure the excess energy in the cations is less than a single probe photon (1.55 eV) and below the cation fragmentation energy.[129,136] Excited state lifetimes are governed by electron-hole interactions, the magnitude of the transition energy, and nuclear motion. TD-DFT

calculations were performed to explore the excited states at the ground state (S_0) and adiabatically optimized excited state geometry (S_1). For simplicity, we limit analysis to the S_1 state as a general description of photoexcitation. The S_1 state is the final state along the relaxation pathway and contains the biggest energy gap, suggesting it is the rate limiting step in relaxation. The large density of states and vibrational modes enables rapid internal conversion to the S_1 state in accordance with Kasha's rule which assumes the lowest excited state defines the photocatalytic activity of the system.[137]

To interpret the role of the electron-hole interactions on excited state lifetimes, several topological descriptors were calculated at both vertical excitation (S_0) and upon adiabatic relaxation to the S_1 minimum energy. Photoexcitation involves several molecular orbitals, making transition densities an efficient representation of the location and distribution of holes and electrons. The Λ index quantifies the charge-transfer character of excited states (Λ_1) as the spatial overlap of electron and hole wavefunctions,[32,138,139] and ranges between 0 and 1 to describe wavefunctions that share no common space or complete overlap, respectively. Low Λ values suggest that the exciton obtains a strong charge-transfer character upon excitation and further increases on the S_1 landscape. The distance between electron and hole density centroids ($d_{e\text{-}h}$) is a complementary approach to measuring the charge-transfer length.[140] Although Λ and $d_{e\text{-}h}$ are traditionally thought to relate to recombination lifetimes, neither parameter reconciles with the experimental lifetimes, shown in Table 5.1. Both values are small, revealing that charges often localize on neighboring atoms without overlapping, thus demonstrating a

large ionic character. These parameters are not reliable for such ionic systems and are poor predictors of excited state lifetimes for $(TiO_2)_n$ clusters.

Upon photoexcitation, subtle changes in both the local geometry and electronic structure enable carrier localization and polaron formation which accounts for the measured lifetime oscillation. Theory shows the electronic structures of $(TiO_2)_n$ clusters exhibit an even/odd oscillation with additional TiO_2 units.[130,141,142] Clusters with an even number of TiO_2 units have larger HOMO-LUMO gaps, IPs, optical excitation energies, and exciton binding energies (E_x). Larger energy spacings are indicative of more stable and rigid structures. The delocalization of each charge carrier is quantified by the total-root-mean-square density (σ_e or σ_h). The charge carriers are all delocalized upon vertical excitation, but in all cases, they separate (increasing $d_{e\text{-}h}$) and localize (decreasing σ) on the S_1 potential. Pivotal energies and topological parameters with lifetimes are shown in Table 5.1. During adiabatic relaxation, both charge carriers show preference to localize on the least coordinated atoms. The under-coordinated Ti atom, typically found in the center of the cluster adjacent to a highly coordinated O atom, serves as the localization center for the electron density. If the hole overcomes the exciton binding energy, it migrates to a terminal O atom. The relaxation energy (E_R) is the final difference in vertical ionization potential and adiabatic relaxation energy.

Table 5.1 Experimental Excited State Lifetimes (τ) and Calculated Properties for $(TiO_2)_n$ Clusters.

$(TiO_2)_n$	τ (fs)	Λ	d (Å)	σ_{av} (Å^3)	E_X (eV)	E_R (eV)
1	256 ± 16	0.26	1.73	3.31	5.33	0.11
2	364 ± 56	0.22	2.89	3.54	5.49	0.89
3	281 ± 66	0.14	4.16	2.83	2.69	1.29

4	669 ± 227	0.25	2.45	3.20	3.87	0.99
5	494 ± 102	0.24	1.81	3.11	3.75	0.86
6	567 ± 160	0.30	2.40	3.95	4.30	1.00
7	568 ± 167	0.25	3.90	4.40	4.08	1.00
8	491 ± 104	0.30	1.82	4.28	4.59	0.84
9	598 ± 164	0.35	2.50	4.31	3.89	1.10

Structural rearrangement accompanies charge localization as the clusters relax through a Jahn-Teller (J-T) type distortion on S_1, similar to polaron formation in bulk structures. Due to the tetrahedral coordination of the Ti atoms, this results in a Ti-O bond elongation ($\Delta r_{Ti\text{-}O}$) that is more pronounced in even numbered clusters (Figure 5.2). Although polarons are a bulk concept, the language is appropriate even for molecular-scale clusters due to the local structure deformation and localization of charge carriers. The polaron couples to the vibrational motion of the cluster and facilitates rapid depopulation by a radiationless transition through a conical intersection on the femtosecond timescale. Dangling bonds are known to facilitate internal conversion.[143]

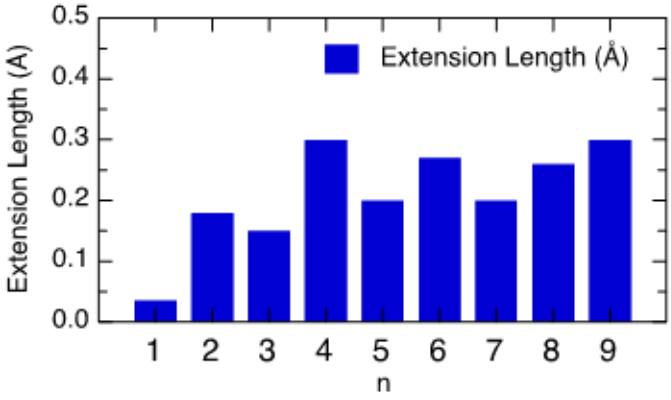

Figure 5.2 The Longest Bond Extension as Calculated for $(TiO_2)_n$ Clusters.

Variation in clusters provides a range of geometric configuration that mimic the active sites of bulk surfaces and can be utilized to understand the coupling between

polaron formation and related lifetime changes. The formation of localized charge carriers and Coulomb attraction between the electron and hole drives relaxation. The averaged distribution of the electron and hole ($\sigma_{e\text{-}h}$) correlates with the measured lifetime of TiO_2 clusters (Figure 5.3). In general, the odd-numbered clusters are more planar in nature and exhibit shorter lifetimes than the even-numbered clusters. The higher symmetry and rigidity of even-numbered clusters presents a more delocalized energy landscape where the S_0 transition density is distributed across all atomic centers, except those directly bound to the terminal O. Upon relaxation, the even-numbered clusters show larger carrier delocalization (σ) that inhibits nonradiative decay pathways leading to longer lifetimes.

The smallest three clusters are planar, feature under-coordinated Ti atoms, and exhibit the shortest lifetimes. TiO_2 and $(TiO_2)_2$ are too small to enable separation and therefore have large E_X. Following excitation, $(TiO_2)_2$ adopts a more planar geometry as the hole localizes on a terminal O atom. $(TiO_2)_3$ is unique in that it contains a three-fold coordinated Ti and O. The electron density moves onto the 3d orbital of the under-coordinated Ti atom and the hole localizes on the opposite side of the cluster. $(TiO_2)_3$ has the smallest S_1 energy gap, and the largest E_R, which are both strong drivers for recombination. Relaxation on the S_1 landscape localizes the hole to one terminal O and has the smallest bond extension of all clusters.

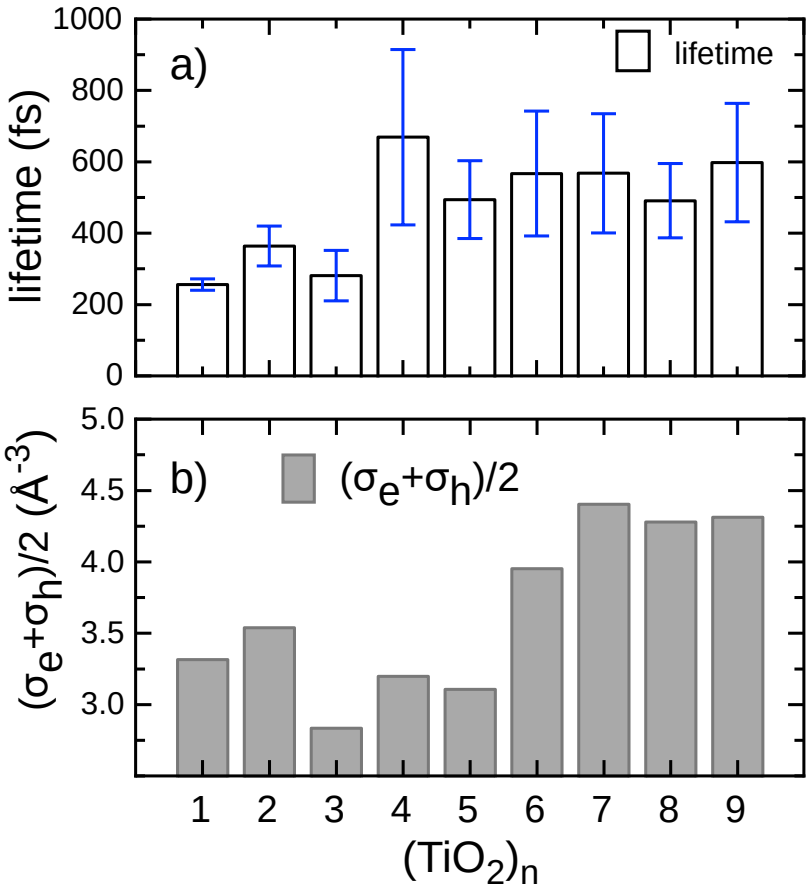

Figure 5.3 Comparison Between a) the Lifetime of $(TiO_2)_n$ Clusters and b) the Average Delocalization Between the Electron and Hole of Each Cluster.

An increase in lifetime occurs as the clusters move to a 3D structure and feature Ti atoms that are all tetracoordinated. Both $(TiO_2)_4$ and $(TiO_2)_5$ structures contain a tetra-coordinated O atom with ionic character which provides rigidity.[129] Upon adiabatic relaxation, the electron of $(TiO_2)_4$ localizes on one Ti, but the hole behaves as a multi-site polaron distributed about two O atoms causing a large local bond elongation. On the S_0 landscape of $(TiO_2)_5$, the electron resides on the Ti furthest from the terminal O, the hole arises from the three adjacent O atoms, while the majority of the cluster is inactive. Upon

adiabatic relaxation on S_1, the hole localizes to one O forming an exciton pair that reduces the excited state lifetime.

As the cluster size increases above $(TiO_2)_6$, the oscillation is less apparent, and lifetimes approach a similar value. $(TiO_2)_6$ exhibits a low number of vibrational bands,[144] highlighting a rigid structure that contains a tetra-coordinated O in its center. Despite having hole and electron density on adjacent atoms following relaxation, the distortion appears localized to one bond elongation, while the remaining cluster is rigid, hindering localization. Similar to the n = 4, $(TiO_2)_6$ does not drive electron localization. Furthermore, $(TiO_2)_4$ and $(TiO_2)_6$ have large local bond elongations of 0.30 Å and 0.27 Å, respectively, prolonging the lifetime.

Both $(TiO_2)_5$ and $(TiO_2)_8$ exhibit relatively low E_R, resulting in a strong localization of both carriers into a bound exciton (Ti^{3+}-O^-) pair, which facilitates internal conversion. The centrosymmetric S_0 state of $(TiO_2)_8$ contains delocalized charge carriers spread over the entire cluster. $(TiO_2)_8$ has the largest E_X, where the S_1 structure migrates the electron and hole to adjacent atoms in the middle of the cluster and contains a large Λ_1, supporting a shortened lifetime. Both of these clusters have a ‘‘glassy’’ energy landscape and exhibit a large number of low-energy isomers.[145] Their flexible structures enable charge localization and rapid relaxation.

In $(TiO_2)_7$ and $(TiO_2)_9$, the hole migrates to a trapped site, leaving a delocalized electron in the core of the cluster due to a small E_{ex}. In $(TiO_2)_7$, both charge carriers are delocalized, but on opposite ends of the cluster. The S_1 relaxation mechanism is similar to $(TiO_2)_2$, where the hole localizes on the terminal O and becomes more planar. The

remaining cluster is unperturbed, inhibiting electron polaron formation (σ_e= 5.86 Å). This separation reduces the electron-hole overlap (Λ_1 = 0.25) and slows recombination to break the oscillating trend, showing a similar lifetime to $(TiO_2)_6$. The breakdown in oscillation occurs at similar size regime as the onset of bulk-like energy gaps.[146] $(TiO_2)_9$ contains a highly coordinated center (six-fold coordinated Ti and several tri-coordinated O atoms) that attracts both charge carriers on S_1. The electron does not localize, but the hole forms a multicenter polaron with similar lifetime.

The excited-state lifetimes of $(TiO_2)_n$ clusters reach a steady value as they approach the ~1 nm size regime, with similar values (τ~550 fs) recorded for clusters of n $\geq$ 7. The tightly bound electron-hole pairs are consistent with the sub-nanometer exciton binding radius found in bulk structures. The oscillation in lifetimes as clusters grow is attributed to structural differences between the clusters that control charge localization and polaron formation. Time-dependent density functional calculations show the increased lifetime for even clusters is associated with a more rigid structure, lower electron-hole pair localization, and extended bond lengths. Polaron formation is highly dependent on local structure and shortens excited state lifetimes. Therefore, the utilization of rigid structures accompanied by bond elongation and delocalized polarons is essential for the production of titanium oxide materials with longer excited state lifetimes.

5.4 Results and Discussion for Sub-Stoichiometric Clusters

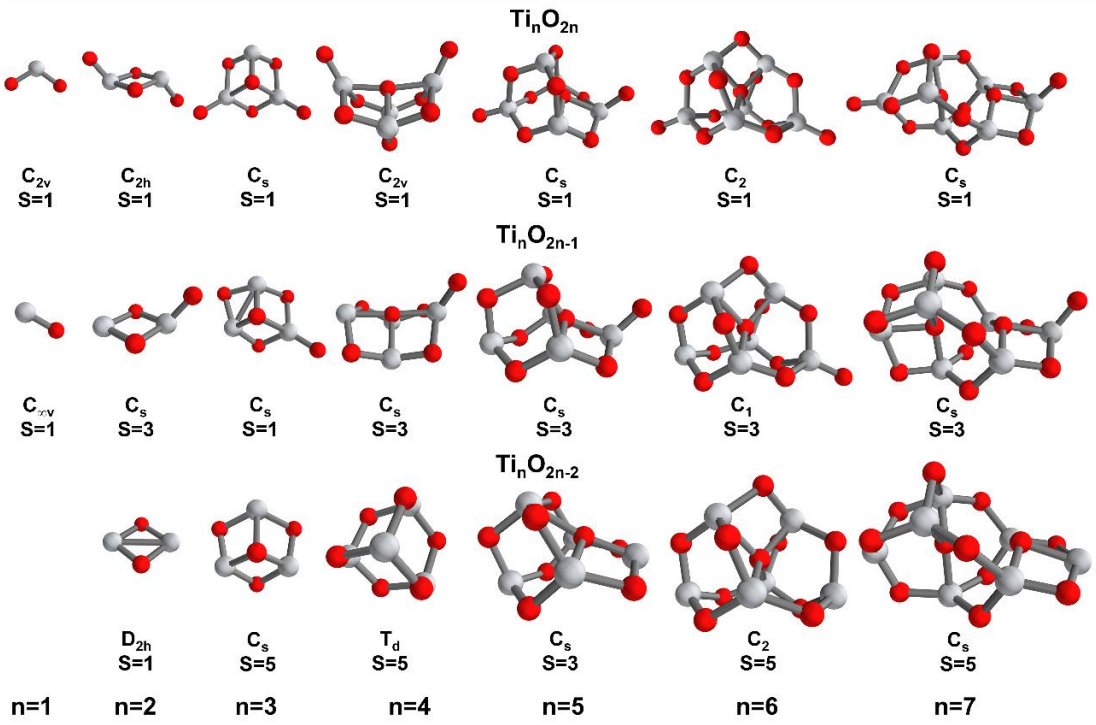

Figure 5.4 Optimized Ground State Structures of Ti_nO_{2n-x} Clusters n = 1−7 and x = 0−2. The Gray and Red Spheres Represent the Ti and O Atoms, Respectively. Ti−Ti Bonds are Drawn if Their Distances are Less Than 2.72 Å, and Bond Order is Not Illustrated.

Although sub-nanometer clusters form geometric structures that are far from the crystalline lattice of the bulk, their electronic structure mimics the band structure of bulk materials except that their atomic orbitals form discrete energy levels instead of continuum bands. Formally, each O atom removes two electrons from the d-orbitals of the Ti atoms resulting in closed electronic shells. For example, the Ti_nO_{2n} clusters contain no d electrons, making the HOMO composed of O-2p orbitals and the LUMO composed of Ti-3d orbitals, mimicking the valence and conduction bands of the bulk band structure. Instead of octahedral metal centers, the Ti atoms in subnanometer titanium oxide clusters are typically tetracoordinated, and the O atoms serve as either terminal or bridging atoms.

The minimum energy Ti_nO_{2n} structures are in agreement with previously reported structures using numerous computational methods.[119,121,125,126,147–152] Each Ti_nO_{2n} cluster contains two dangling O atoms. They are closed shell species, where all of the Ti-d electrons are transferred to the O atoms and, therefore, serve as models for the electronic structure of defect-free bulk titania. Similarly, suboxide clusters act as models for the distortions caused by O vacancies in TiO_2 materials.

Far less work has been performed on the suboxide clusters, with only a few calculations previously reported.[152,153] The initial choices for the atomic coordinates for the geometrical optimization of the suboxide clusters were considered and obtained from previously published studies but optimized using the functional and basis set described in section 5.2. For instances where multiple cluster geometries were examined, we report the lowest energy geometry (Figure 5.4). The lowest energy structures for the suboxide clusters contain a similar cage structure as the stoichiometric series, except they are missing either one or both terminal O. However, unlike the stoichiometric clusters, the suboxide clusters are open shell systems and their spin states were assigned according to the lowest energy structures following optimization to all possible spin configurations (Table 5.2). The formation of O vacancies is accompanied by a local distortion and compression of the Ti atoms nearest the vacancy.

Table 5.2 The Relative Energies of the Suboxides in Different Spin Multiplicities.

	Singlet eV	**Triplet eV**	**Quintet eV**
TiO	1.18	0.00	--
--	--	--	--
Ti_2O_3	0.53	0.00	--
Ti_2O_2	0.00	0.17	0.084
Ti_3O_5	0.00	0.72	--
Ti_3O_4	1.04	0.23	0.00

Ti_4O_7 Ti_4O_6	0.67 0.96	0.00 0.30	-- 0.00
Ti_5O_9 Ti_5O_8	0.63 1.32	0.00 0.00	-- 0.17
Ti_6O_{11} Ti_6O_{10}	1.25 1.87	0.00 0.46	-- 0.00
Ti_7O_{13} Ti_7O_{12}	1.33 2.01	0.00 1.42	-- 0.00

In suboxide clusters with singlet spin ground states, a strong compression is found between Ti atoms leading to Ti−Ti bonds. In systems with triplet and quintet ground states, this compression is compensated by the electron−electron spin repulsion and, therefore, maintains similar structure to the Ti_2O_{2n} clusters. The exception to this trend is Ti_4O_6, where substantial rearrangement occurs leading to a more stable tetrahedral geometry. The C_s symmetry group of odd-numbered Ti_nO_{2n} clusters ensures that the two terminal O are not equivalent, and the O with the weaker bond is absent in the Ti_2O_{2n-1} series. For example, for Ti_5O_9, removal of one terminal O atom results in an isomer that is 0.61 eV higher in energy than removal of the other. In the Ti_nO_{2n-2} series, both terminal O atoms are absent resulting in all remaining O atoms being bridged between two Ti atoms. The variation in local cluster geometries provides a variety of configurations that mimic the active sites of bulk surfaces and can be employed to understand which factors drive polaron formation and related charge carrier localization.

In bulk, the average Ti−O bond length is 1.95 Å.[97] The stoichiometric clusters offer similar bond lengths, with an average of 1.9 Å for bridging O atoms. However, the terminal O bonds are 1.6 Å, indicating the presence of double bonds.[154] In O deficient clusters, the bridging Ti−O bonds stretch, especially near the reduced Ti atom as a means

of compensating for the compression of the Ti atoms. For example, in the Ti_4O_7 cluster, the Ti−O bonds near the O vacancy stretch by ~0.05 Å while the Ti−Ti distance compresses by 0.05 Å and causes the Ti−O−Ti angle to go from 102.5° in the stoichiometric cluster to 98.8°. Although the average metal-to-metal distance in stoichiometric clusters is >2.8 Å, the distances decrease with removal of O atoms.[155] We utilized the covalent radius of Ti atoms (1.36 Å) to assign the formation of Ti−Ti bonds when their distance is < 2.72 Å.[156] In the singlet suboxide structures Ti_2O_2 and Ti_3O_5, Ti−Ti bonds formed with distances of 2.70 and 2.41 Å, respectively.

5.4.1 Structure and Stability

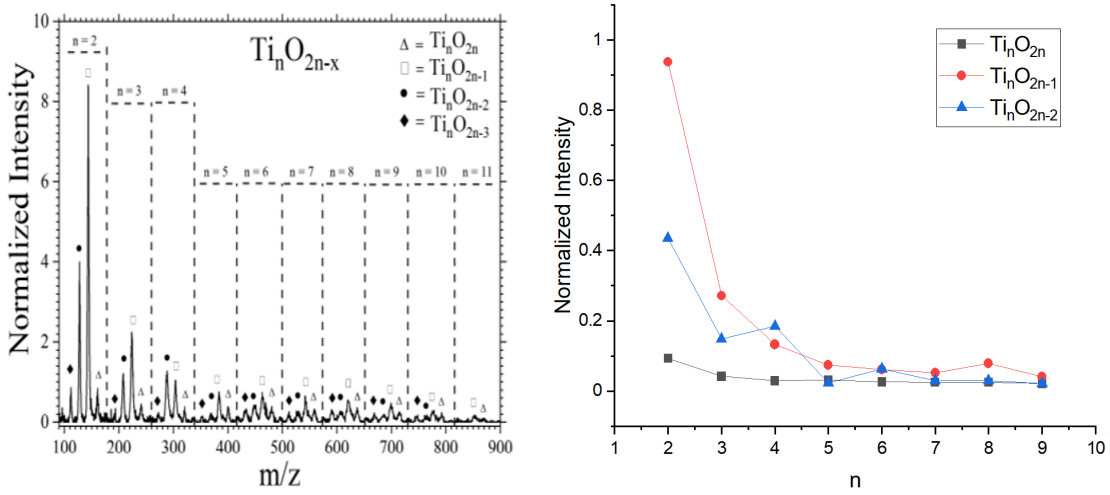

Figure 5.5 Left) Ionized Neutral Titanium Oxide Cluster Distribution at Temporal Overlap. Right) Normalized Intensity of the Static Mass Spectra Peaks of the Ti_nO_{2n-x} Clusters Generated via Laser Ablation.

The experimental cluster distribution obtained through the femtosecond laser ionization of neutral clusters was published previously[157] and reveals the presence of neutral clusters containing several stoichiometries, with the Ti_nO_{2n-1} series generally being the most prominent. The Ti_nO_{2n} series is the least intense cluster series in the distribution. The relative intensities are in agreement with previous results where VUV

light was employed for ionization.[158] The relative signal intensities of the clusters in the experimental mass spectrum (Figure 5.5) show several outliers that have increased signal relative to their neighboring peaks and suggest they contain an enhanced stability. Specifically, Ti_2O_2, Ti_4O_6, and Ti_6O_{10} exhibit increased experimental signal relative to the other clusters in the Ti_nO_{2n-2} series as well as their Ti_nO_{2n} and Ti_nO_{2n-1} counterparts.

Our calculations reveal that the symmetry groups of Ti_2O_2 (D_{2h}), Ti_4O_6 (T_d), and Ti_6O_{10} (C_2) are higher than the C_s of the other Ti_nO_{2n-2} clusters which accounts for their increased signal intensity in the mass spectrum. All clusters in the Ti_nO_{2n-1} series, except Ti_6O_{11} (C_1 symmetry group), contain a mirror plane. Higher symmetry is well-known to be correlated to increased stability. Therefore, the lower symmetry accounts for the relative fragility of Ti_6O_{11} and explains its low formation and signal intensity compared to Ti_6O_{10} in the cluster distribution prepared through laser ablation. Additionally, the relative E_b of the terminal O atoms (Figure 5.6) provides insight into the relative stability of the clusters. In general, the E_b for each cluster is between 3 and 7 eV. Ti_2O_3 is the most stable peak in the cluster distribution reflecting the highest calculated binding energy. Ti_4O_7 has the lowest E_b, making it particularly susceptible to O dissociation and may account for Ti_4O_6 being particularly prominent.

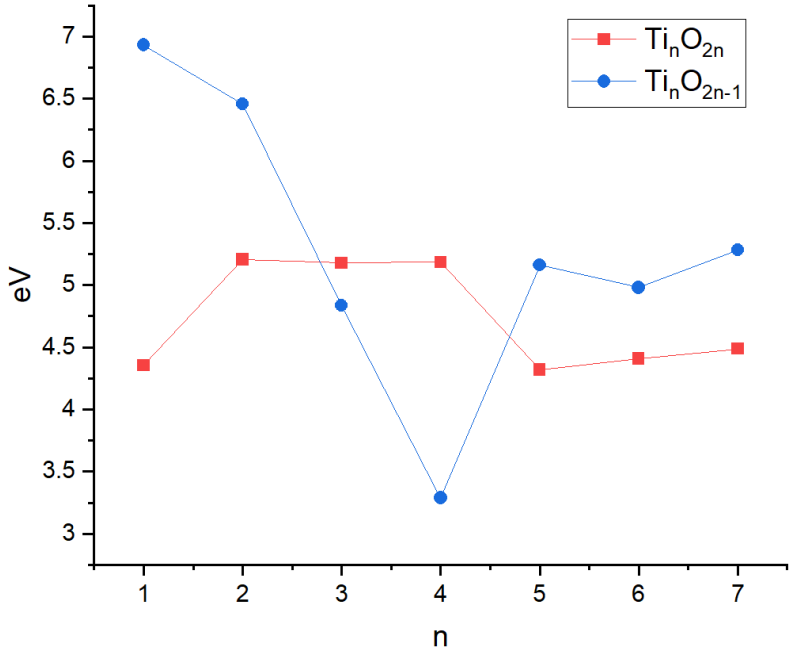

Figure 5.6 Binding Energy of O Atoms from Ti_nO_{2n} and Ti_nO_{2n-1}.

5.4.2 Electronic Properties

Table 5.3 Energetic Information for the Ground States of the Stoichiometric, Missing One O, and Missing Two O Clusters. All Energies are Reported in eV.

	I_P	E_a	E_x[a]	α-HOMO-α-LUMO	O_{gap}	F_{gap}
TiO_2	10.02	1.74	5.43	6.50	2.85	8.28
TiO	7.12	1.16	5.96	5.42	1.02	5.96
	--	--	--	--	--	--
Ti_2O_4	11.05	1.60	5.50	7.75	3.95	9.45
Ti_2O_3	7.07	1.34	5.37	4.97	0.36	5.73
Ti_2O_2	5.37	0.79	4.45	4.33	0.13	4.58
Ti_3O_6	10.33	2.99	3.38	6.49	3.96	7.34
Ti_3O_5	7.87	1.24	5.28	5.19	1.36	6.64
Ti_3O_4	6.38	0.67	5.50	4.66	0.22	5.71
Ti_4O_8	11.29	1.60	5.56	8.02	4.13	9.69
Ti_4O_7	7.54	1.50	5.80	5.22	0.24	6.04
Ti_4O_6	8.95	0.48	7.73	6.18	0.74	8.47
Ti_5O_{10}	11.21	2.40	4.79	7.70	4.02	8.81
Ti_5O_9	8.18	0.92	6.61	5.72	0.65	7.26
Ti_5O_8	7.22	1.05	8.01	3.95	1.84	6.17
Ti_6O_{12}	11.42	2.43	4.49	7.65	4.50	8.99
Ti_6O_{11}	8.18	1.28	6.40	5.84	0.50	6.90
Ti_6O_{10}	7.14	1.66	5.04	5.34	0.43	5.48
Ti_7O_{14}	11.23	2.74	4.04	7.88	4.45	8.49
Ti_7O_{13}	7.92	1.82	5.94	5.61	0.15	6.10
Ti_7O_{12}	7.44	1.28	5.82	4.49	0.35	6.17

The density of states (DOS) accessible by the solar spectrum increases with d electrons. The energetic parameters of IP, E_a, E_x, HOMO-LUMO gap, and O_{gap} are presented in Table 5.3. In general, with increased number of O vacancies, the IP, HOMO−LUMO gap, and O_{gap} all decrease by several eV. E_a is smallest for the Ti_nO_{2n-2} series. The E_a values calculated for Ti_2O_{2n} clusters range between 1.6 and 3 eV and are in general agreement with experimental measurements.[159] Experimental IP values for Ti_nO_{2n} clusters are not available for comparison, but our values align with prior calculations,[121] showing they have large (>10.0 eV) values. In contrast, our calculations show the suboxide clusters have a smaller IP by several eV. These values have not been previously reported either experimentally or computationally for suboxide clusters. The F_{gap} of the stoichiometric clusters is largest for all sizes given its closed shell nature. The F_{gap} decreases with removal of O atom with the exception of Ti_4O_6; the high symmetry of this cluster leads to a high fundamental gap as well as high E_x. Our results show suboxides have higher E_x for the ground state geometry than Ti_nO_{2n} clusters with the exception of Ti_3O_x cluster series. The increase in E_x suggests a stabilization of electron−hole pairs with O deficiencies. The E_x is anomalously low in Ti_3O_6, and the charge carriers separate to opposite ends of the cluster.

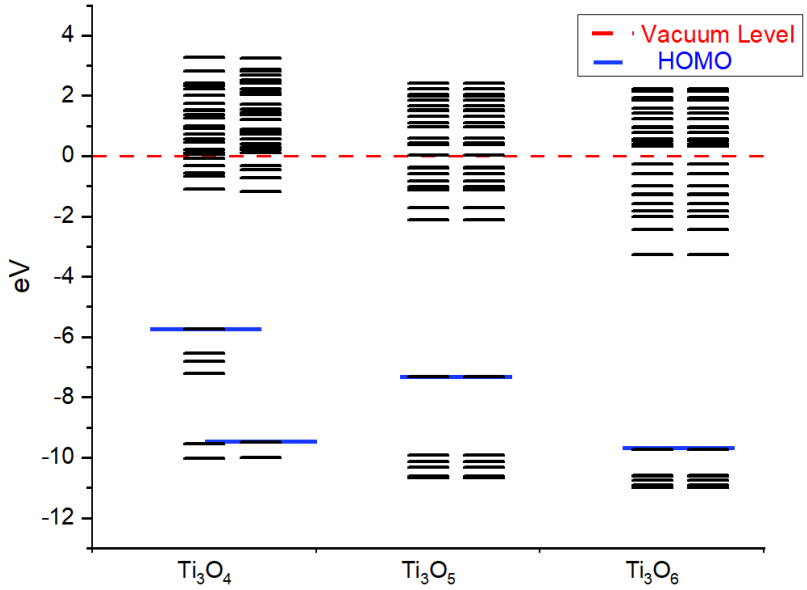

Figure 5.7 Density of States of Ti_3O_4, Ti_3O_5, and Ti_3O_6 in Relation to the Vacuum Level (α Orbitals are Plotted on the Left and β Orbitals are Plotted on the Right for Each Cluster). The Blue Line Represents the HOMO for Each Cluster. Note That for Closed Shell Systems the α and β Orbitals are Equivalent.

The HOMO−LUMO gap for the open shell systems is reported as the gap between the highest singly occupied α orbital and the lowest unoccupied α orbital. For all open shell clusters, the α gap is smaller than the gap between the highest singly occupied β orbital and the lowest unoccupied β orbital. The HOMO−LUMO gap decreases by multiple eV upon the absence of an O atom. The dominant effect of O vacancies in these clusters is an upshift in the valence states leading to a smaller HOMO−LUMO gap compared to stoichiometric clusters (Figure 5.7). The increase in HOMOs leaves fewer orbitals below the vacuum level, and the LUMOs become closer in energy. The O_{gap} of the stoichiometric clusters is near 4.0 eV, which is slightly larger than that of bulk anatase (3.2 eV). In contrast, suboxide clusters exhibit a much smaller O_{gap} of < 1 eV due to the partially filled d orbitals and, therefore, contain a continuum of states that are accessible within the visible region. A quantum confinement effect is not observed

because the energy spacing between the triplet and singlet in the stoichiometric clusters is small.[150,160] The O_{gap} is nearly uniform for a given cluster series (Table 5.3) and is significantly smaller than the HOMO−LUMO gap as the excited state is a combination of molecular orbitals that incorporates the attraction between the charge carriers. The reduction in the HOMO−LUMO gap and O_{gap} occurs for all suboxide clusters and is consistent with changes in reduced bulk which have shown valence band shifts near O vacancies.[89] These results show that the O_{gap} and HOMO−LUMO gap can be tuned by changing the size and structures of clusters, providing a way to further tune their electronic and optical characteristics.

The values of the energetic parameters for the first excited state of both stoichiometric and sub-stoichiometric clusters were also calculated and reported in Table 5.4. The trends for the excited state values are consistent with the trends reported for the ground state structures.

Table 5.4 The Ionization Potentials (IP), electron affinity (E_a). Optical Gap (O_{gap}), Fundamental Gap (F_{gap}), Exciton Binding Energy (E_x), and the Fluorescence Energy of the first excited states (denoted with an asterisk) of Ti_nO_{2n-x} (x = 0, 1, 2) clusters. All values are eV.

	I_P^* (eV)	E_a^* (eV)	O_{gap}^* (eV)	F_{gap}^* (eV)	E_x^* (eV)	Fluorescence Energy (eV)
Ti_1O_2	9.84	1.84	2.67	8.00	5.33	0.18
Ti_1O_1	7.12	1.16	0.0026	5.96	5.96	1.02
--						
Ti_2O_4	10.28	2.41	2.38	7.87	5.49	1.57
Ti_2O_3	7.11	1.31	0.35	5.80	5.44	0.01
Ti_2O_2	5.37	0.79	0.13	4.58	4.45	0.00
Ti_3O_6	8.85	4.18	1.98	4.67	2.69	1.98
Ti_3O_5	6.20	2.85	0.15	3.36	3.21	1.21
Ti_3O_4	6.44	0.57	0.12	5.87	5.75	0.09
Ti_4O_8	10.01	3.64	2.50	6.37	3.87	1.63
Ti_4O_7	7.50	1.28	0.24	6.22	5.98	0.00
Ti_4O_6	7.58	0.96	0.68	6.63	5.94	0.06

Ti_5O_{10}	9.86	3.56	2.55	6.30	3.75	1.47
Ti_5O_9	7.63	1.45	0.40	6.18	5.78	0.26
Ti_5O_8	8.08	0.23	0.14	7.85	7.71	1.70
Ti_6O_{12}	10.76	3.55	2.91	7.21	4.30	1.59
Ti_6O_{11}	7.77	2.48	0.28	5.29	5.01	0.21
Ti_6O_{10}	10.61	0.07	0.12	10.55	10.42	0.31
Ti_7O_{14}	9.74	2.96	2.71	6.79	4.08	1.75
Ti_7O_{13}	7.60	2.11	0.25	5.49	5.25	-0.10
Ti_7O_{12}	7.31	1.75	0.17	5.56	5.39	0.18

5.4.3 Excited State Topology

The subtle balance between on-site electrostatic potential and the electrostatic coupling between electron and hole drives the charge carrier localization and charge transport. Topological parameters of the ground and excited states provide insight into the nature of the lowest energy excited states and the degree to which different sites stabilize excited electron and hole components by structural deformation. In the Ti_nO_{2n} clusters, the hole is located on the O atoms but moves onto Ti atoms in all suboxides. The presence of the O vacancy causes the Ti atoms to compress to stabilize the 3d electron density. The stoichiometric clusters exhibit an elongation of terminal O bonds upon photoexcitation which localizes the hole on an O atom. In contrast, the low energy of the first excited state of the suboxides and the lack of involvement of any O atoms reduce the geometry distortion caused by photoexcitation where the dominant effect is a slight elongation of Ti−O bonds near the hole, leaving the majority of the cluster unperturbed (Figure 5.8 and Figure 5.9).

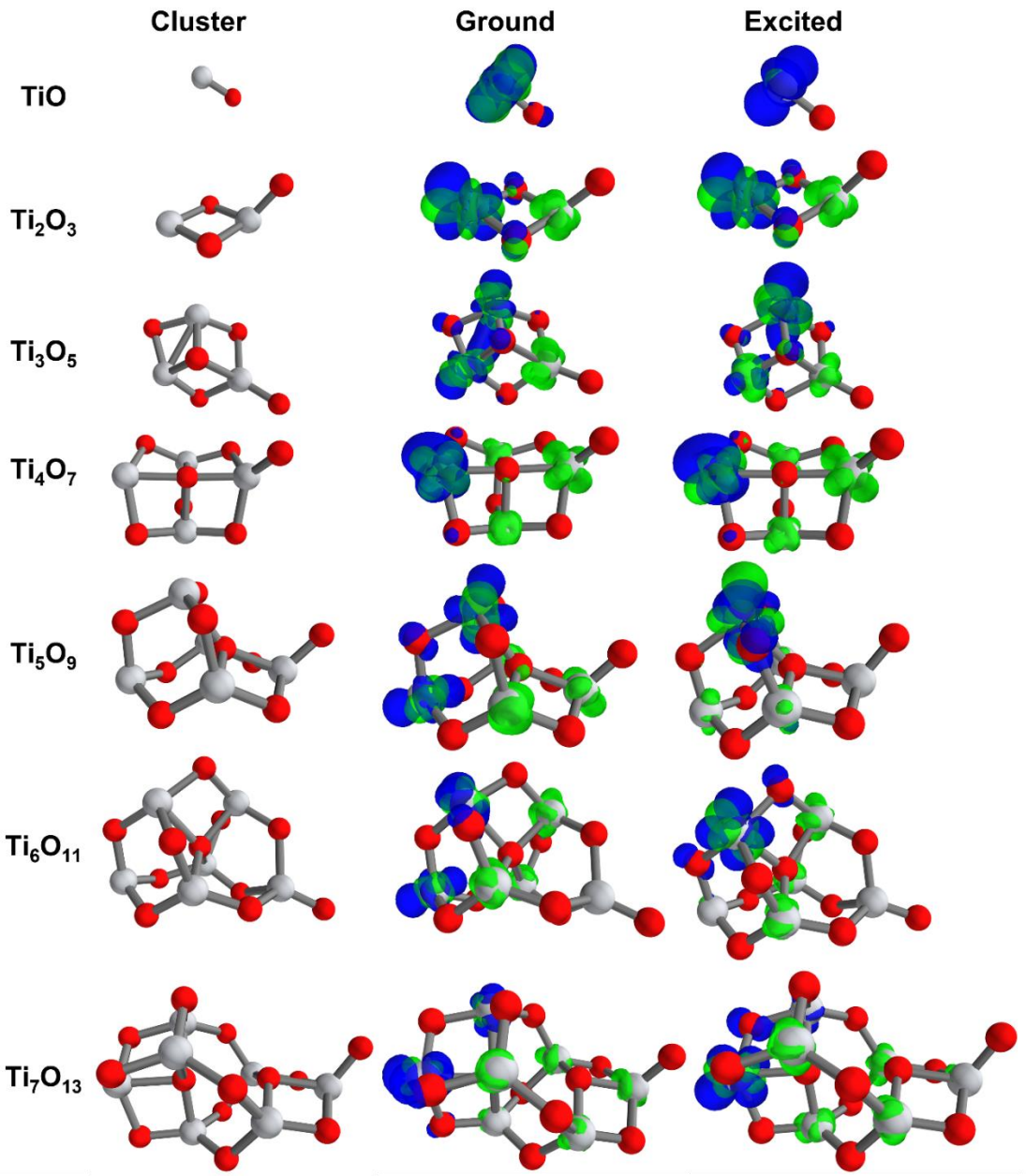

Figure 5.8 TD-CAM-B3LYP Transition Densities for the First Excited State at the Ground State Geometry (Center) and Adiabatically Relaxed First Excited State Geometry (Right) for Ti_nO_{2n-1}. The Hole is in Blue and the Electron is in Green.

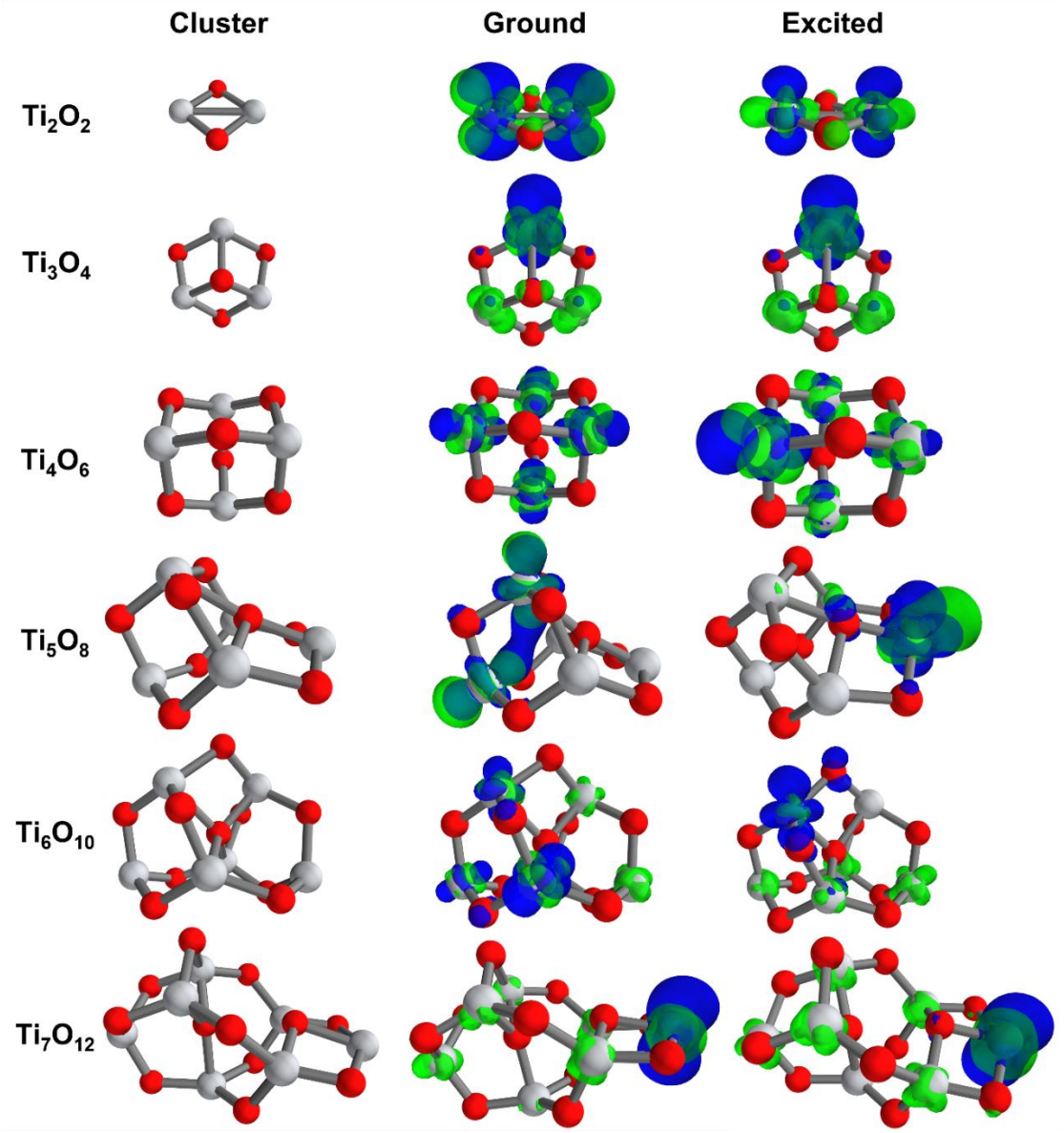

Figure 5.9 TD-CAM-B3LYP Transition Densities for the First Excited State at the Ground State Geometry (Center) and Adiabatically Relaxed First Excited State Geometry (Right) for Ti_nO_{2n-2}. The Hole is in Blue and the Electron is in Green.

This is demonstrated in the changes in the topological parameters of the first excited state before and after adiabatic relaxation (Table 5.5). In general, the stoichiometric clusters show a localization upon relaxation of both the hole and the electron ($\Delta\sigma_h$, $\Delta\sigma_e < 0$), and a separation of charge carriers ($\Delta d_{eh} > 0$). Comparatively, the

suboxides have significantly smaller changes in topological parameters and little rearrangement of the atoms upon adiabatic relaxation.

Table 5.5 The Topological Descriptors for Ti_nO_{2n-x} (x = 0, 1, 2) are Used to Quantify the Distribution and Spatial Interaction of the Electron and Hole in the Ground and Excited State According to TD-DFT CAM-B3LYP.

	Λ	σ_{hole} ($Å^3$)	$\sigma_{electron}$ ($Å^3$)	$\sigma_{average}$ ($Å^3$)	d_{eh} (Å)	Λ^*	σ_{hole}^* ($Å^3$)	$\sigma_{electron}^*$ ($Å^3$)	$\sigma_{average}^*$ ($Å^3$)	d_{eh}^* (Å)
Ti_1O_2	0.26	3.05	3.60	3.33	1.68	0.26	3.04	3.59	3.31	1.73
Ti_1O_1	0.63	2.17	2.17	2.17	0.00	0.63	2.15	2.15	2.15	0.00
--										
Ti_2O_4	0.30	4.28	4.87	4.58	0.00	0.22	2.85	4.23	3.54	2.89
Ti_2O_3	0.53	2.57	5.02	3.79	0.51	0.53	2.57	4.97	3.77	0.47
Ti_2O_2	0.70	3.50	5.67	4.59	0.20	0.60	4.02	5.19	4.60	0.17
Ti_3O_6	0.18	4.35	4.49	4.42	2.83	0.14	2.91	2.76	2.83	4.16
Ti_3O_5	0.53	3.82	4.19	4.01	0.65	0.55	3.14	4.65	3.90	0.70
Ti_3O_4	0.46	3.18	5.00	4.09	1.46	0.43	3.50	5.58	4.54	1.55
Ti_4O_8	0.28	5.42	3.54	4.48	1.37	0.25	3.91	2.49	3.20	2.45
Ti_4O_7	0.44	2.73	5.02	3.87	1.77	0.43	2.75	4.92	3.84	1.76
Ti_4O_6	0.59	4.79	4.73	4.76	0.12	0.57	4.37	4.60	4.49	0.69
Ti_5O_{10}	0.23	5.14	3.67	4.40	0.95	0.24	3.08	3.14	3.11	1.81
Ti_5O_9	0.46	3.85	4.88	4.36	1.40	0.55	2.86	4.22	3.54	0.26
Ti_5O_8	0.86	4.02	5.11	4.57	0.38	0.52	3.12	4.90	4.01	0.13
Ti_6O_{12}	0.31	6.16	4.65	5.41	1.59	0.3	3.73	4.18	3.95	2.40
Ti_6O_{11}	0.47	4.00	5.24	4.62	1.49	0.47	2.83	4.84	3.83	1.50
Ti_6O_{10}	0.48	4.02	6.14	5.08	1.40	0.32	3.33	7.43	5.38	2.16
Ti_7O_{14}	0.31	5.67	4.70	5.18	1.82	0.25	2.94	5.87	4.40	3.90
Ti_7O_{13}	0.39	3.35	6.05	4.70	2.70	0.41	3.00	5.72	4.50	2.34
Ti_7O_{12}	0.38	3.18	6.56	4.87	2.55	0.38	4.01	6.05	5.03	1.82

Both the Λ and d_{eh} values calculated for stoichiometric clusters are small, revealing a highly ionic character where charges localize on neighboring atoms without overlapping. The Ti_nO_{2n} clusters are void of d electrons and the excited states are strictly ligand-to- metal charge-transfer (LMCT) in character between the O-2p and Ti-3d orbitals. However, the partially filled d-orbitals of the suboxides profoundly affect the photoexcitation energies and properties by enabling a large density of d−d transitions at

low energy. Analysis of the atomic contribution of the lowest 100 optically allowed excited states of the suboxides shows that although there are many more states below the bandgap of bulk TiO_2, the energy required to access LMCT remains consistent around 6 eV for larger clusters (Figure 5.10). For the first excited state, the suboxide clusters show metal-to-metal charge transfer (MMCT). The larger Λ values calculated for the suboxides demonstrate that the photoexcitation mechanism transitions from an ionic LMCT character transition for Ti_nO_{2n} clusters ($\Lambda < 0.3$) to a covalent MMCT character transition for the substoichiometric series ($\Lambda \sim 0.5$). In many suboxides, the hole and the electron coexist on the Ti^{3+} atom.

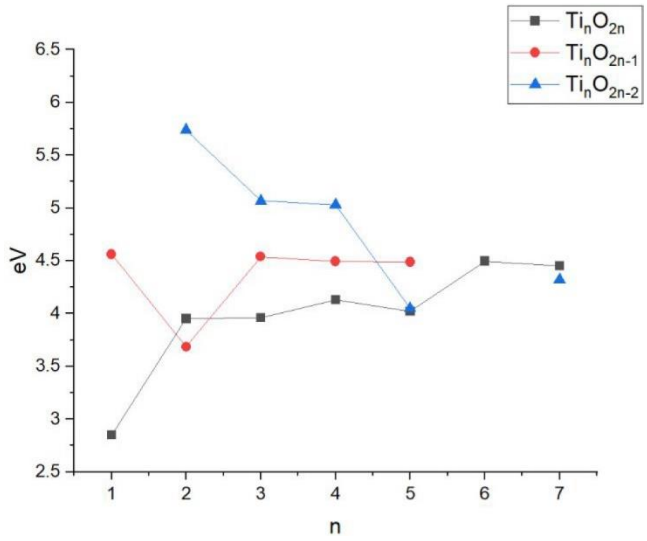

Figure 5.10 Energy Required to Access at Least 50% LMCT. For the Ti_nO_{2n} Series, the Energy of the S_1 State is Plotted. Ti_6O_{10}, Ti_6O_{11}, and Ti_7O_{13} Do Not Contain LMCT Transitions.

Bulk titania exhibits a subnanometer exciton binding radius[161,162] that is consistent with the small d_{eh} calculated for the clusters. In all clusters, d_{eh} remains small after adiabatic relaxation (less than half the cluster diameter) (Table 5.5), reflecting a strong E_x. The d_{eh} values demonstrate that the charge carriers separate by either one or two Ti−O

bonds in stoichiometric clusters. However, the d_{eh} values for most suboxide clusters are substantially smaller than their stoichiometric counterparts (Figure 5.11) and are separated by only a single Ti−O bond or less. In particular, the d_{eh} values for several Ti_2O_{2n-2} clusters (particularly those with lower spin configurations) are < 1.0 Å, aligning with a high E_x.

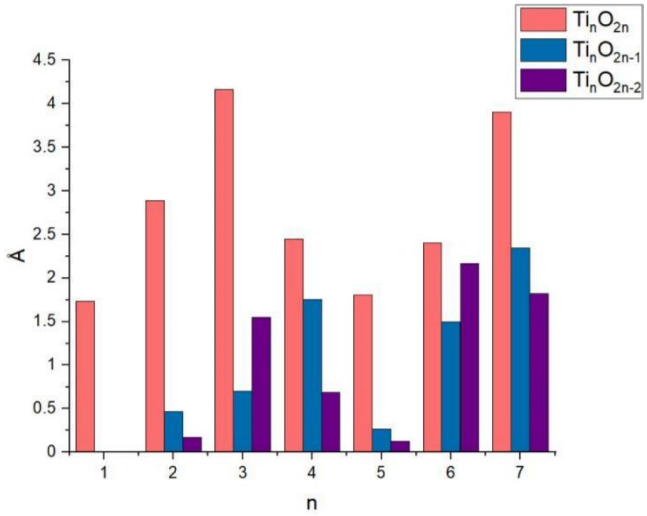

Figure 5.11 Distance Between the Hole and Electron in the First Excited State Geometries.

In the Ti_nO_{2n} clusters, the hole is typically confined primarily to the terminal O atoms, but photoexcitation in the suboxide clusters generally does not involve any O atoms. In suboxides, the partially filled 3d orbitals participate in photoexcitation, leaving behind a hole that adopts their characteristics and is localized on the tricoordinated Ti^{3+} sites, which is typically adjacent an O vacancy site in Ti_nO_{2n-1} and Ti_nO_{2n-2} clusters. The reduced Ti^{3+} sites corresponding to O vacancies are precursors for polaron formation. These suboxide clusters show hole−polaron formation on one Ti atom. In contrast, the excited d-electron density of suboxides is typically delocalized across many, if not all, of the Ti atoms in the system. Interestingly, this behavior is starkly different from both the

stoichiometric clusters[157] and extended surfaces,[163] where excess electrons are typically pinned to one Ti^{3+} site.

Our calculations reveal that clusters with stronger hole localization generally exhibit smaller O_{gap}, which is similar to the shallower gap state found in bulk states upon localization. For example, the O_{gap} for Ti_4O_7 is 0.24 eV (σ_h = 2.73 Å^3), and that for Ti_5O_8 is 1.84 eV (σ_h = 4.02 Å^3). It is clear that the geometric configurations surrounding the O-vacancy generally facilitates hole−polaron formation upon low energy excitations. In contrast, the electron trap sites arise from undercoordinated Ti atoms that appear in closed shell clusters, such as in Ti_5O_{10} and Ti_3O_6. The electron density shows a preference for tricoordinated Ti sites but does not localize in any of the suboxides under low energy excitation. Therefore, hole trapping is more common than electron trapping and aligns with the mobilities suggested for bulk titania, where the electrons behave according to the band model and holes migrate through a hopping mechanism.[89]

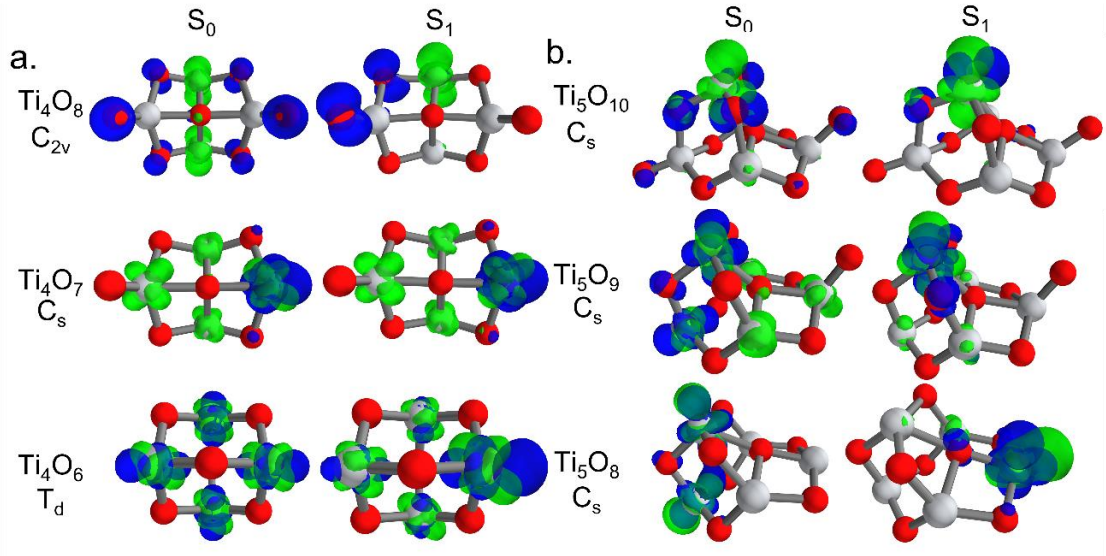

Figure 5.12 TD-CAM-B3LYP Transition Densities for the First Excited State at the Ground State Geometry (Left) and Adiabatically Relaxed First Excited State Geometry

(Right) of the (a) Ti_4O_8, Ti_4O_7, and Ti_4O_6 and (b) Ti_5O_{10}, Ti_5O_9, and Ti_5O_8 Clusters at an Isodensity of 0.005/Å^3. Electron Density is Green, the Hole is Blue, Ti Atoms are Gray, and O Atoms are Red.

The charge distributions for the ground state and first excited state structures of the Ti_4O_{8-x} and Ti_5O_{10-x} ($x \leq 2$) clusters serve as examples to highlight the extreme variation in excited state character that occurs within subnanometer titanium oxide clusters (Figure 5.12). Topological parameters for the first excited state (Λ^*, σ_h^*, σ_e^*, σ_{ave}^*, and d_{eh}^*) are presented in Table 5.5 and are used to demonstrate changes in excited state character. Similar analysis for the remaining clusters is presented in Table 5.6 and Figure 5.8 and Figure 5.9.

Table 5.6 Changes in the Topological Parameters for all Titanium Oxide Clusters Following Adiabatic Relaxation.

	($\Lambda^* - \Lambda$)	**($\sigma_h^* - \sigma_h$) (Å^3)**	**($\sigma_e^* - \sigma_e$) (Å^3)**	**($\sigma_{ave}^* - \sigma_{ave}$) (Å^3)**	**($d_{eh}^* - d_{eh}$) (Å)**
Ti_1O_2	0.00	-0.01	-0.01	-0.01	0.05
Ti_1O_1	0.00	-0.02	-0.02	-0.02	0.00
--					
Ti_2O_4	-0.08	-1.43	-0.64	-1.04	2.89
Ti_2O_3	0.00	0.00	-0.05	-0.02	-0.05
Ti_2O_2	-0.13	0.51	-0.49	0.01	-0.04
Ti_3O_6	-0.04	-1.44	-1.73	-1.59	1.33
Ti_3O_5	0.02	-0.68	0.46	-0.11	1.11
Ti_3O_4	-0.03	0.32	0.58	0.45	0.09
Ti_4O_8	-0.03	-1.51	-1.05	-1.28	1.08
Ti_4O_7	0.00	0.02	-0.09	-0.04	-0.01
Ti_4O_6	0.01	-0.42	-0.13	-0.27	0.57
Ti_5O_{10}	0.01	-2.06	-0.53	-1.30	0.86
Ti_5O_9	0.09	-0.99	-0.66	-0.82	-1.13
Ti_5O_8	-0.34	-0.91	-0.21	-0.56	-0.26
Ti_6O_{12}	-0.01	-2.43	-0.47	-1.45	0.81
Ti_6O_{11}	-0.01	-1.17	-0.40	-0.78	0.01
Ti_6O_{10}	-0.16	-0.69	1.30	0.30	0.76
Ti_7O_{14}	-0.06	-2.73	1.17	-0.78	2.08
Ti_7O_{13}	0.02	-0.35	-0.33	-0.34	-0.36
Ti_7O_{12}	0.00	0.83	-0.52	0.16	-0.73

Upon adiabatic relaxation, both Ti_4O_8 and Ti_5O_{10} exhibit exciton formation, whereas the suboxides demonstrate electron density delocalization. Ti_4O_8 excitation involves all O atoms but only the Ti furthest from the terminal O. The charge carriers for this cluster form a two-center hole polaron and exciton pair ($\Lambda^* = 0.25$ and $d_{eh}^* = 2.45$ Å). The partially filled d orbitals of Ti_4O_7 exhibits a highly localized hole, centered on the Ti^{3+} site adjacent the O vacancy and a delocalized electron, spread over the remaining Ti atoms. However, there is a preference for both the electron and hole to localize on the tricoordinated Ti in Ti_4O_7 ($\Lambda^* = 0.43$, $d_{eh}^* = 1.76$ Å). This strongly localized hole density that overlaps the dominant portion of electron density is found in many suboxides and is expected to inhibit the formation of long-lived excited states by facilitating the photogenerated charge carrier recombination and ultimately reducing catalytic performance. The T_d symmetry of the Ti_4O_6 cluster creates a unique phenomenon in which the electron and hole are distributed across the entire cluster ($\Lambda^* = 0.57$, $d_{eh}^* = 0.69$ Å).

Each Ti_4O_x cluster exhibits a different symmetry group and demonstrates unique charge carrier behavior upon photoexcitation. In contrast, the Ti_5O_x clusters all belong to the C_s symmetry group yet reveal a similar range of effects. The closed shell Ti_5O_{10} cluster contains a unique tricoordinated Ti that serves as an electron localization site. Similar to Ti_4O_8, the hole distributes on neighboring O atoms in an exciton pair ($\Lambda^* = 0.24$, $d_{eh}^* = 1.81$ Å). However, in Ti_5O_9, both the hole and the electron are delocalized away from the terminal O. After adiabatic relaxation, the electron and hole localize and overlap ($\Lambda^* = 0.55$, $d_{eh}^* = 0.26$ Å) far from the terminal O. The Ti_5O_8 cluster contains a

pseudoplanar tricoordinated Ti^{3+} site which acts as a trap site upon adiabatic relaxation for both the electron and the hole ($\Lambda^* = 0.52$, $d_{eh}{}^* = 0.13$ Å). This variation and range in topological properties demonstrate that neither symmetry nor oxygen content is the dominant factor in charge localization, but it is instead determined by subtle changes to the local bonding configurations within the clusters.

5.5 Conclusion

A description of excited states of neutral, subnanometer Ti_nO_{2n}, Ti_nO_{2n-1}, and Ti_nO_{2n-2} clusters is presented using TDDFT calculations. O deficient clusters contain higher spin states that stabilize the increased d electron density and maintain similar cluster geometries as their stoichiometric counterparts. Both Ti_2O_2 and Ti_4O_6 form higher symmetry geometries that distribute the charge carriers and account for their relatively intense signals in experimental cluster distributions. Our calculations reveal that the introduction of O vacancies in subnanometer titania improves IR and visible light absorption and is accompanied by partially filled d orbitals that influence the excited state properties of the clusters. In suboxide clusters, the low-lying excited states are metal-to-metal charge transfer in contrast to the stoichiometric clusters that exhibit ligand-to-metal charge transfer. The localization of d-electrons on Ti sites generally produces a compression of nearby Ti atoms. Although the d-electrons tend to localize in the vicinity of the O defect, they often occupy multiple Ti sites. The electron does not localize on a single Ti site unless bound to a hole in an exciton pair. The reduced Ti^{3+} atoms act as exciton trapping sites in these subnanometer materials, analogous to the electron trapping in undercoordinated Ti^{3+} centers that accompany O defect sites in bulk and surface sites.

Our results demonstrate that these suboxide clusters capture the important features of oxygen vacancy sites in bulk titania. Further, the variation in local bonding environment and relative charge density distributions of these subnanometer clusters highlight structural patterns that can be applied for designing new materials containing long-lived excited states and low absorption energy.

CHAPTER 6

CONCLUSIONS AND FUTURE DIRECTIONS

6.1 Conclusions

The work in this thesis used femtosecond time-of-flight mass spectrometry paired with computational modeling to explore the excited state dynamics of molecules and clusters. Excited state dynamics are shown to be highly dependent on subtle changes in the structure and composition of the species. Pairing femtosecond TOF-MS with computational modeling of excited states allows for investigation of the effect of structure on excited state dynamics.

Studying both molecules, such as alkyl halides, as well as clusters, such as titanium oxides, provides two unique investigations. The excited state dynamics of alkyl halides, such as was shown with n-butyl bromide, are heavily dependent on the vibrational stretching of the C-X bond. Similarly, the excited state dynamics of titanium oxide clusters are heavily dependent on the structural deformation of the cluster upon photoexcitation. In these clusters, the structure shifts in order to stabilize the electron-hole pair (polaron formation), and the degree of shift has a direct impact on the lifetime of the cluster excited state.

The excited state dynamics of n-butyl bromide demonstrated the significance of intramolecular vibrational energy redistribution (IVR) in alkyl halides and the role it plays in photodissociation. The photodissociation of n-butyl bromide is characterized by three types of bond scission: 1) C-Br, 2) C-C, and 3) C-H. Each of these dissociations occurs with different lifetimes and energies. The rate at which energy is redistributed

after being deposited via photoexcitation can be observed in the transients of the fragments of the parent species. Redistribution of energy from the photon, to bond scission and vibrational motion is a fundamental component of photochemistry.

Theoretical and experimental investigation of titanium oxide clusters demonstrates the significant dependence of the cluster properties on the degree of oxidation. Stoichiometric $(TiO_2)_n$ clusters possess ligand-to-metal charge transfer excited states at high energies (~6 eV). The excited state lifetimes of the stoichiometric clusters are reflective of the degree of polaron formation occurring within the excited cluster. In contrast, sub-oxide Ti_nO_{2n-x} clusters have much smaller optical gaps and possess predominantly metal-to-metal charge transfer excited states. The removal of an oxygen atom from a stoichiometric cluster adds a large density of states below the traditional band-gap of the bulk materials. Furthermore, the characteristics of the excited states of sub-oxides show a much larger degree of delocalization of the electron and hole. These changes in properties are due to the increased d-electron character of the sub-oxide clusters. Knowledge of the effects of oxidation on titanium oxide clusters provides insight into the effects of oxygen vacancies in bulk materials and can be used to develop new, more favorable bulk materials.

Ultimately, the work has demonstrated the role of geometry, oxidation, bond strength, and electron density on the lifetimes and properties of excited states. Through femtosecond resolved spectroscopy and computation analysis of excited states, the presented research provided an in-depth look at the real time dynamics of molecules and clusters.

6.2 Future Directions

The work in this dissertation focused on the properties of excited states in molecules and clusters. The knowledge gathered provides new insights into the methods with which energy deposited into a species is either redistributed into chemical mechanisms such as dissociation or vibrational energy or stabilized via geometry distortion leading to localization of electrons and holes. When comparing the behavior of excited states in molecules and metal-oxide clusters, information on fundamental chemistry can be explored.

The dynamics of n-butyl bromide were found to be largely dependent on the vibrational motion of the covalent C-Br bond of the molecule. Small changes in the C-Br separation leads to significant changes in the potential energy surfaces of the Rydberg states of the molecule. Predissociation into smaller fragments occurs from the Rydberg manifold and relaxation within the manifold disrupts the dissociation pathway of C-C and C-H fragmentation. Ultimately, the dynamics of this molecule are directly dependent on the degree to which vibrational motion and energy redistribution into vibrational motion occurs. The linear aspect of n-butyl bromide allowed for significant activation of the carbon chain. Future work in this vane focused on investigating the effect of both chain length and structure by expanding into a variety of carbon back-bone lengths and isomers will demonstrate the relationship between degrees of freedom, symmetry, and saturation with dissociation dynamics. The greater the length of the carbon chain, the more delocalized the excited states, which will allow for more fragmentation pathways and a higher degree of IVR. However, branched carbon chains will limit the activation of the

carbon chain given the non-linear structure. Furthermore, given the significance of the C-Br bond in determining relaxation pathways, alkyl group with different substituents groups ought to be used to investigate the roll of bond strength in unimolecular reactions.

Metal-oxide clusters, which contain ionic metal-non-metal bonds, have excited states which are characterized by the degree of electron and hole stabilization via adiabatic relaxation. Small changes in the cluster geometry, induced by photoexcitation, leads to dramatic changes in the localization and separation of the electron and hole densities. This affect is analogous to exciton and polaron formation in bulk materials which define the reactive behavior of the material. Changes in the oxidation of the molecule leads to a more covalent nature of the cluster and allows for metal-to-metal charge transfer in photoexcited states. Analogous studies on metal-carbides could provide insight into the role of oxygen and carbon in semiconducting materials. Carbide compounds are often ceramics with low conductivity, implying the nature of charge carriers would be dramatically different than those of metal oxides. Changes in the ligand properties will likely have a profound effect on the geometry, behavior, and lifetimes of excited states given the difference in bonding environment.

The work of this thesis opens the door to understand how bond types (i.e., covalent or ionic) determine the excited state nature of a species. In purely ionic species, such as stoichiometric titanium oxide clusters, there is a clear electron donor and a clear electron acceptor. However, in species with a more covalent nature, the excited electron is more delocalized across the bond in the species instead of isolated to individual atoms. Comparison between substituents on carbon chains as well as comparison between metal-

ligand bonds of different levels of covalency will show the impact of charge separation versus delocalization as an influence on excited state stability. The more covalent nature of the C-Br bond (relative to other C-X bonds) in n-butyl bromide showed a low barrier for dissociation while it is likely C-Cl would not dissociate as readily. Similarly, the ionic nature of Ti-O bonds in titanium oxide clusters showed the significance of charge separation, a feature that will likely not be as influential in more covalent bonds such as Ti-C.

Future work looking to further investigate how the degree of ionic or covalent nature of a species affects the excited state dynamics will improve on the understanding of excited states and molecular stabilization or dissociation as it relates to bonding types. Varying the substituents and ligands in molecules and cluster and analyzing their excited state dynamics can provide a range of information relating to molecular and cluster composition.

.

BIBLIOGRAPHY

(1) Baker, S.; Robinson, J. S.; Haworth, C. A.; Chirila, C. C.; Lein, M.; Tisch, J. W. G.; Marangos, J. P. Probing Fast Nuclear Wavepackets in Light Molecules: Monitoring Structural Rearrangement on an Attosecond Timescale. *J. Mod. Opt.* **2007**, *54*, 1011–1017.

(2) Zewail, A. H. Laser Femtochemistry. *Nature* **2009**, *462*, 824–824.

(3) Zewail, A. H. Femtochemistry: Atomic-Scale Dynamics of the Chemical Bond. *J. Phys. Chem. A* **2000**, *104*, 5660–5694.

(4) Condon, E. U. The Franck-Condon Principle and Related Topics. *Am. J. Phys.* **1947**, *15*, 365–374.

(5) Keldysh, L. V. Ionization in the Field of a Strong Electromagnetic Wave. *J. Exp. Theor. Phys.* **1964**, *47*, 1945–1957.

(6) Perelomov, A. M.; Popov, V. S.; Terent'ev, M. V. Ionization of Atoms in an Alternating Electrical Field. *Sov. Phys. JETP* **1966**, *23*, 924.

(7) Ammosov, M. V.; Delone, N. B.; Krainov, V. P. Tunneling Ionization of Complex Atoms and of Atomic Ions in an Alternating Electromagnetic Field. *Robotica* **2004**, *22*, 319–327.

(8) Tong, X. M.; Zhao, Z. X.; Lin, C. D. Theory of Molecular Tunneling Ionization. *Phys. Rev. A - At. Mol. Opt. Phys.* **2002**, *66*, 11.

(9) Jena, P.; Castleman, A. W. Clusters: A Bridge across the Disciplines of Physics and Chemistry. *Proc. Natl. Acad. Sci. U. S. A.* **2006**, *103*, 10560–10569.

(10) Strickland, D.; Mourou, G. Compression of Amplified Chirped Optical Pulses. *Opt. Commun.* **1985**, *56*, 219–221.

(11) Maine, P.; Strickland, D.; Bado, P.; Pessot, M.; Mourou, G. Generation of Ultrahigh Peak Power Pulses by Chirped Pulse Amplification. *IEEE J. Quantum Electron.* **1988**, *24*, 398–403.

(12) Poletto, L. Grazing-Incidence Flat-Field Spectrometer for High-Order Harmonic Diagnostics. *Opt. Eng.* **2001**, *40*, 178.

(13) Corkum, P. B. Plasma Perspective on Strong Field Multiphoton Ionization. *Phys. Rev. Lett.* **1993**, *71*, 1994–1997.

(14) Henke, B. L.; Gullikson, E. M.; Davis, J. C. X-Ray Interactions: Photoabsorption, Scattering, Transmission, and Reflection at E=50-30000 EV, Z=1-92. *At. Data*

Nucl. Data Tables **1993**, *54*, 131–342.

(15) W. C. Wiley and I. H. McLaren. Time-of-Flight Mass Spectrometer with Improved Resolution. *Rev. Sci. Instrum.* **1955**, *26*.

(16) Garcia, J. M.; Shaffer, R. E.; Sayres, S. G. Ultrafast Pump-Probe Spectroscopy of Neutral Fe_nO_m Clusters (n, m < 16). *Phys. Chem. Chem. Phys.* **2020**, *22*, 24624–24632.

(17) Pederson, S.; Zewail, A. H. Femtosecond Real Time Probing of Reactions XXII Kinetic Description of Probe Absorption Fluorescence Depletion and Mass Spectrometry. *Mol. Phys.* **1996**, *89*, 1455–1502.

(18) Dermota, T. E.; Hydutsky, D. P.; Bianco, N. J.; Castleman, A. W. Excited-State Dynamics of $(SO2)_m$ Clusters. *J. Phys. Chem. A* **2005**, *109*, 8259–8267.

(19) Dermota, T. E.; Hydutsky, D. P.; Bianco, N. J.; Castleman, A. W. Photoinduced Ion-Pair Formation in the $(HI)_m$ $(H_2O)_n$ Cluster System. *J. Chem. Phys.* **2005**, *123*.

(20) Ramachandran, K. I.; Deepa, G.; Namboori, K. *Computational Chemistry and Molecular Modeling: Principles and Applications*; Springer-Verlag: Berlin, Germany, 2008.

(21) Jensen, F. *Introduction to Computational Chemistry*, Second Edi.; John Wiley and Sons Inc.: New York, New York, 2007.

(22) Cramer, C. J. *Essentials of Computational Chemistry : Theories and Models*, Second Edi.; John Wiley and Sons Inc.: West Sussex, England, 2004.

(23) Hohenberg, P.; Kohn, W. Inhomogeneous Electron Gas. *Phys. Rev. B* **1964**, *136*.

(24) Kohn, W.; Sham, L. J. Self-Consistent Equations Including Exchange and Correlation Effects. *Phys. Rev. A* **1965**, *140*.

(25) Runge, E.; Gross, E. K. . Density-Functional Theory for Time-Dependent Systems. *Phys. Rev. Lett.* **1984**, *52*.

(26) Hirata, S.; Head-Gordon, M. Time-Dependent Density Functional Theory within the Tamm-Dancoff Approximation. *Chem. Phys. Lett.* **1999**, *314*, 291–299.

(27) Berardo, E.; Hu, H. S.; Shevlin, S. A.; Woodley, S. M.; Kowalski, K.; Zwijnenburg, M. A. Modeling Excited States in TiO_2 Nanoparticles: On the Accuracy of a TD-DFT Based Description. *J. Chem. Theory Comput.* **2014**, *10*, 1189–1199.

(28) Becke, A. D. Density-Functional Exchange-Energy Approximation with Correct

Asymptotic Behavior. *Phys. Rev. A* **1988**, *38*.

(29) Lee, C.; Yang, W.; Parr, R. G. Development of the Colle-Salvetti Correlation-Energy Formula into a Functional of the Electron Density. *Phys. Rev. B* **1988**, *37*.

(30) Burke, K. Perspective on Density Functional Theory. *J. Chem. Phys.* **2012**, *136*.

(31) Yanai, T.; Tew, D. P.; Handy, N. C. A New Hybrid Exchange-Correlation Functional Using the Coulomb-Attenuating Method (CAM-B3LYP). *Chem. Phys. Lett.* **2004**, *393*, 51–57.

(32) Berardo, E.; Hu, H. S.; Van Dam, H. J. J.; Shevlin, S. A.; Woodley, S. M.; Kowalski, K.; Zwijnenburg, M. A. Describing Excited State Relaxation and Localization in TiO_2 Nanoparticles Using TD-DFT. *J. Chem. Theory Comput.* **2014**, *10*, 5538–5548.

(33) Hu, C.; Sugino, O.; Watanabe, K. Performance of Tamm-Dancoff Approximation on Nonadiabatic Couplings by Time-Dependent Density Functional Theory. **2020**, *054106*.

(34) Mewes, S. A.; Plasser, F.; Krylov, A.; Dreuw, A. Benchmarking Excited-State Calculations Using Exciton Properties. *J. Chem. Theory Comput.* **2018**, *14*, 710–725.

(35) Bäppler, S. A.; Plasser, F.; Wormit, M.; Dreuw, A. Exciton Analysis of Many-Body Wave Functions: Bridging the Gap between the Quasiparticle and Molecular Orbital Pictures. *Phys. Rev. A - At. Mol. Opt. Phys.* **2014**, *90*, 45–48.

(36) Valero, R.; Morales-Garciá, Á.; Illas, F. Investigating the Character of Excited States in TiO2 Nanoparticles from Topological Descriptors: Implications for Photocatalysis. *Phys. Chem. Chem. Phys.* **2020**, *22*, 3017–3029.

(37) Peach, M. J. G.; Benfield, P.; Helgaker, T.; Tozer, D. J. Excitation Energies in Density Functional Theory: An Evaluation and a Diagnostic Test. *J. Chem. Phys.* **2008**, *128*.

(38) Eppink, A. T. J. B.; Parker, D. H. Energy Partitioning Following Photodissociation of Methyl Iodide in the A Band: A Velocity Mapping Study. *J. Chem. Phys.* **1999**, *110*, 832–844.

(39) Zhang, Q.; Marvet, U.; Dantus, M. Femtosecond Dynamics of Photoinduced Molecular Detachment from Halogenated Alkanes. II. Asynchronous Concerted Elimination of I_2 from CH_2I_2. *J. Chem. Phys.* **1998**, *109*, 4428–4442.

(40) Marvet, U.; Zhang, Q.; Brown, E. J.; Dantus, M. Femtosecond Dynamics of Photoinduced Molecular Detachment from Halogenated Alkanes. I. Transition

State Dynamics and Product Channel Coherence. *J. Chem. Phys.* **1998**, *109*, 4415–4427.

(41) Dzvonik, M.; Yang, S.; Bersohn, R. Photodissociation of Molecular Beams of Aryl Halides. *J. Chem. Phys.* **1974**, *61*, 4408–4421.

(42) Fan, H.; Pratt, S. T. Photodissociation of Propargyl Bromide and Photoionization of the Propargyl Radical. *J. Chem. Phys.* **2006**, *124*.

(43) Freedman, A.; Yang, S. C.; Kawasaki, M.; Bersohn, R. Photodissociation of Aryl and Aryl-Alkyl Halides at 193 Nm: Fragment Translational Energy Distributions. *J. Chem. Phys.* **1980**, *72*, 1028–1033.

(44) Kadi, M.; Davidsson, J.; Tarnovsky, A. N.; Rasmusson, M.; Åkesson, E. Photodissociation of Aryl Halides in the Gas Phase Studied with Femtosecond Pump-Probe Spectroscopy. *Chem. Phys. Lett.* **2001**, *350*, 93–98.

(45) Kadi, M.; Davidsson, J. The Photodissociation Dynamics of Dibromobenzenes and Tribromobenzene in the Gas Phase Studied with Femtosecond Pump-Probe Spectroscopy. *Chem. Phys. Lett.* **2003**, *378*, 172–177.

(46) Kötting, C.; Diau, E. W. G.; Søiling, T. I.; Zewail, A. H. Coherent Dynamics in Complex Elimination Reactions: Experimental and Theoretical Femtochemistry of 1,3-Dibromopropane and Related Systems. *J. Phys. Chem. A* **2002**, *106*, 7530–7546.

(47) Kötting, C.; Diau, E. W. G.; Baldwin, J. E.; Zewail, A. H. Direct Observation of Resonance Motion in Complex Elimination Reactions: Femtosecond Coherent Dynamics in Reduced Space. *J. Phys. Chem. A* **2001**, *105*, 1680–1682.

(48) Butler, J. H. Better Budgets for Methyl Halides? *Nature* **2000**, *403*, 260–261.

(49) Simpson, W. R.; Von Glasow, R.; Riedel, K.; Anderson, P.; Ariya, P.; Bottenheim, J.; Burrows, J.; Carpenter, L. J.; Frieß, U.; Goodsite, M. E.; et al. Halogens and Their Role in Polar Boundary-Layer Ozone Depletion. *Atmos. Chem. Phys.* **2007**, *7*, 4375–4418.

(50) Blanchet, V.; Samartzis, P. C.; Wodtke, A. M. UV Photodissociation of Methyl Bromide and Methyl Bromide Cation Studied by Velocity Map Imaging. *J. Chem. Phys.* **2009**, *130*.

(51) De Nalda, R.; Durá, J.; García-Vela, A.; Izquierdo, J. G.; González-Vázquez, J.; Bañares, L. A Detailed Experimental and Theoretical Study of the Femtosecond A-Band Photodissociation of CH_3I. *J. Chem. Phys.* **2008**, *128*, 244309.

(52) Escure, C.; Leininger, T.; Lepetit, B. Ab Initio Study of Valence and Rydberg

States of CH_3Br. *J. Chem. Phys.* **2009**, *130*, 1–8.

(53) Escure, C.; Leininger, T.; Lepetit, B. Ab Initio Study of Methyl-Bromide Photodissociation in the Ã Band. *J. Chem. Phys.* **2009**, *130*.

(54) Kvaran, Á.; Wang, H.; Matthíasson, K.; Bodi, A. Two-Dimensional (2+ n) REMPI of CH_3Br: Photodissociation Channels via Rydberg States. *J. Phys. Chem. A* **2010**, *114*, 9991–9998.

(55) Corrales, M. E.; Loriot, V.; Balerdi, G.; González-Vázquez, J.; De Nalda, R.; Bañares, L.; Zewail, A. H. Structural Dynamics Effects on the Ultrafast Chemical Bond Cleavage of a Photodissociation Reaction. *Phys. Chem. Chem. Phys.* **2014**, *16*, 8812–8818.

(56) Murillo-Sánchez, M. L.; Zanchet, A.; Marggi Poullain, S.; González-Vázquez, J.; Bañares, L. Structural Dynamics Effects on the Electronic Predissociation of Alkyl Iodides. *Sci. Rep.* **2020**, *10*, 1–11.

(57) Alekseyev, A. B.; Liebermann, H. P.; Buenker, R. J. Ab Initio Configuration Interaction Study of the B- and C-Band Photodissociation of Methyl Iodide. *J. Chem. Phys.* **2011**, *134*.

(58) Hafliason, A.; Glodic, P.; Koumarianou, G.; Samartzis, P. C.; Kvaran, Á. Multiphoton Rydberg and Valence Dynamics of CH_3Br Probed by Mass Spectrometry and Slice Imaging. *Phys. Chem. Chem. Phys.* **2018**, *20*, 17423–17433.

(59) Shaw, D. A.; Holland, D. M. P.; Walker, I. C. Ion-Pair Formation Mechanisms in Chloromethane, Bromomethane and Dichlorodifluoromethane. *J. Phys. B At. Mol. Opt. Phys.* **2006**, *39*, 3549–3560.

(60) Hafliason, A.; Glodic, P.; Koumarianou, G.; Samartzis, P. C.; Kvaran, Á. Two-Color Studies of CH_3Br Excitation Dynamics with MPI and Slice Imaging. *Phys. Chem. Chem. Phys.* **2019**, *21*, 10391–10401.

(61) Thiré, N.; Cireasa, R.; Staedter, D.; Blanchet, V.; Pratt, S. T. Time-Resolved Predissociation of the Vibrationless Level of the B State of CH_3I. *Phys. Chem. Chem. Phys.* **2011**, *13*, 18485–18496.

(62) Wang, Y.; Shen, H.; Hua, L.; Hu, C.; Zhang, B. Predissociation Dynamics of the B State of CH_3I by Femtosecond Pump-Probe Technique. *Opt. Express* **2009**, *17*, 10506.

(63) Xu, D.; Huang, J.; Price, R. J.; Jackson, W. M. Velocity Imaging Studies on Ion-Pair Dissociation of $CH_3Br + Hv\ VUV \rightarrow CH_3^+ + Br^-$ as a Function of Wavelength. *J. Phys. Chem. A* **2004**, *108*, 9916–9923.

(64) Suto, K.; Sato, Y.; Reed, C. L.; Skorokhodov, V.; Matsumi, Y. Ion Fragment Imaging of the Ion-Pair Photodissociation of CH_3Cl, CH_3Br, C_2H_5Cl, and C_2H_5Br at 118 Nm. **1997**, *5*, 1222–1226.

(65) Ridley, T.; Hennessy, J. T.; Donovan, R. J.; Lawley, K. P.; Wang, S.; Brint, P.; Lane, E. Evidence for Rydberg Doorway States in Photoion Pair Formation in Bromomethane. *J. Phys. Chem. A* **2008**, *112*, 7170–7176.

(66) Hurley, S. M.; Zhong, Q.; Castleman, A. W. Dynamics of the E State of HBr and DBr: Evidence for the Role of Tunneling. *J. Chem. Phys.* **2000**, *112*, 4644–4647.

(67) Kim, H.; Tarakeshwar, P.; Fujikado, N. M.; Evraets, K.; Jones, A. K.; Meneghetti, M.; Buseck, P. R.; Sayres, S. G. Pseudocarbynes: Linear Carbon Chains Stabilized by Metal Clusters. *J. Phys. Chem. C* **2020**, *124*, 19355–19361.

(68) Sato, Y.; Kodama, T.; Shiromaru, H.; Sanderson, J. H.; Fujino, T.; Wada, Y.; Wakabayashi, T.; Achiba, Y. Synthesis of Polyyne Molecules from Hexane by Irradiation of Intense Femtosecond Laser Pulses. *Carbon N. Y.* **2010**, *48*, 1673–1676.

(69) Zaidi, A. A.; Hu, A.; Henneke, D. E.; Duley, W. W. Femtosecond Laser Irradiation of Liquid Alkanes: Mechanism of Polyyne Formation. *Chem. Phys. Lett.* **2019**, *723*, 151–154.

(70) Zaidi, A. A.; Hu, A.; Wesolowski, M. J.; Fu, X.; Sanderson, J. H.; Zhou, Y.; Duley, W. W. Time of Flight Mass Spectrometry of Polyyne Formation in the Irradiation of Liquid Alkanes with Femtosecond Laser Pulses. *Carbon N. Y.* **2010**, *48*, 2517–2520.

(71) Wesolowski, M. J.; Kuzmin, S.; Moores, B.; Wales, B.; Karimi, R.; Zaidi, A. A.; Leonenko, Z.; Sanderson, J. H.; Duley, W. W. Polyyne Synthesis and Amorphous Carbon Nano-Particle Formation by Femtosecond Irradiation of Benzene. *Carbon N. Y.* **2011**, *49*, 625–630.

(72) Garcia, J. M.; Shaffer, R. E.; Sayres, S. G. Ultrafast Pump-Probe Spectroscopy of Neutral Fe: NOmclusters (n, m < 16). *Phys. Chem. Chem. Phys.* **2020**, *22*, 24624–24632.

(73) W. C. Wiley and I. H. McLaren. Time-of-Flight Mass Spectrometer with Improved Resolution. *Rev. Sci. Instrum.* **1955**, *26*, 1150–1157.

(74) Frisch, M. J.; Trucks, G. W.; Schlegel, H. B.; Scuseria, G. E.; Robb, M. A.; Cheeseman, J. R.; Scalmani, G.; Barone, V.; Mennucci, B.; Petersson, G. A.; et al. Gaussian16 (Revision A.03), Gaussian Inc. Wallingford CT. *Gaussian16 (Revision A.03)*. 2016.

(75) Center, N. M. S. D. Mass Spectra. In *NIST Chemistry WebBook, NIST Standard Reference Database Number 69*; Linstrom, P. J., Mallard, W. G., Eds.; National Institute of Standards and Technology, Gaithersburg MD, 20899, 2022.

(76) Shastri, A.; Singh, P. J.; Krishnakumar, S.; Das, A. K.; Raja Sekhar, B. N. Electronic Spectroscopy of Ethyl Bromide Probed by VUV Photoabsorption and Quantum Chemical Calculations. *Phys. Chem. Chem. Phys.* **2017**, *19*, 6454–6469.

(77) Felps, W. S.; Scott, J. D.; Findley, G. L.; McGlynn, S. P. Molecular Rydberg Transitions. XX. Vibronic Doubling in Alkyl Bromides. *J. Chem. Phys.* **1981**, *74*, 4832–4838.

(78) Alekseyev, A. B.; Liebermann, H. P.; Vázquez, G. J.; Lefebvre-Brion, H. Coupled-Channel Study of the Rydberg-Valence Interaction in HBr. *J. Chem. Phys.* **2018**, *148*, 0–6.

(79) Hurley, S. M.; Dermota, T. E.; Hydutsky, D. P.; Castleman, A. W. The Ultrafast Dynamics of HBr-Water Clusters: Influences on Ion-Pair Formation. *J. Chem. Phys.* **2003**, *118*, 9272–9277.

(80) Su, S.; Dorenkamp, Y.; Yu, S.; Wodtke, A. M.; Dai, D.; Yuan, K.; Yang, X. Vacuum Ultraviolet Photodissociation of Hydrogen Bromide. *Phys. Chem. Chem. Phys.* **2016**, *18*, 15399–15405.

(81) Romanescu, C.; Loock, H. P. Photoelectron Imaging Following 2 + 1 Multiphoton Excitation of HBr. *Phys. Chem. Chem. Phys.* **2006**, *8*, 2940–2949.

(82) Gardiner, S. H.; Karsili, T. N. V.; Lipciuc, M. L.; Wilman, E.; Ashfold, M. N. R.; Vallance, C. Fragmentation Dynamics of the Ethyl Bromide and Ethyl Iodide Cations: A Velocity-Map Imaging Study. *Phys. Chem. Chem. Phys.* **2014**, *16*, 2167–2178.

(83) Glodic, P.; Zaouris, D.; Samartzis, P. C.; Haflidason, A.; Kvaran, Á. Effect of a Triplet to Singlet State Interaction on Photofragmentation Dynamics: Highly Excited States of HBr Probed by VMI and REMPI as a Case Study. *Phys. Chem. Chem. Phys.* **2016**, *18*, 26291–26299.

(84) Vaida, M. E.; Leone, S. R. Tracing Dissociation Dynamics of CH_3Br in the $^3Q_0$ State with Femtosecond Extreme Ultraviolet Ionization. *Chem. Phys.* **2014**, *442*, 41–47.

(85) Callaghan, R.; Gordon, R. J.; Callaghan, R.; Gordon, R. J. The Multiphoton Ionization Spectrum Of. **1998**, *4624*.

(86) Aliç, T. Y.; Kiliç, H. Ş.; Durmuş, H.; Doğan, M.; Ledingham, K. W. D. A Mass Spectrometric Investigation of Isomers of Butane. *Rapid Commun. Mass*

Spectrom. **2012**, *26*, 893–905.

(87) Chin, C. H.; Lee, S. H. Comparison of Two-Body and Three-Body Decomposition of Ethanedial, Propanal, Propenal, n-Butane, 1-Butene, and 1,3-Butadiene. *J. Chem. Phys.* **2012**, *136*.

(88) Chen, X.; Mao, S. S. Titanium Dioxide Nanomaterials: Synthesis, Properties, Modifications and Applications. *Chem. Rev.* **2007**, *107*, 2891–2959.

(89) Rajaraman, T. S.; Parikh, S. P.; Gandhi, V. G. Black TiO_2: A Review of Its Properties and Conflicting Trends. *Chem. Eng. J.* **2020**, *389*, 123918.

(90) Hagfeldt, A.; Grätzel, M. Molecular Photovoltaics. *Acc. Chem. Res.* **2000**, *33*, 269–277.

(91) Thompson, T. L.; Yates, J. T. Surface Science Studies of the Photoactivation of TiO_2 New Photochemical Processes. *Chem. Rev.* **2006**, *106*, 4428–4453.

(92) Zhao, W.-N.; Liu, Z.-P. Mechanism and Active Site of Photocatalytic Water Splitting on Titania in Aqueous Surroundings. *Chem. Sci.* **2014**, *5*, 2256–2264.

(93) Guo, Y.; Li, J.-F.; Niu, X.; Markovits, A.; Zhang, R.-Q. Composition Dependent Reactivity of Titanium Oxide Clusters. *Phys. Chem. Chem. Phys.* **2016**, *18*, 10594–10599.

(94) Richter, C.; Schmuttenmaer, C. A. Exciton-like Trap States Limit Electron Mobility in TiO_2 Nanotubes. *Nat. Nanotechnol.* **2010**, *5*, 769–772.

(95) Gallart, M.; Cottineau, T.; Hönerlage, B.; Keller, V.; Keller, N.; Gilliot, P. Temperature Dependent Photoluminescence of Anatase and Rutile TiO_2 Single Crystals: Polaron and Self-Trapped Exciton Formation. *J. Appl. Phys.* **2018**, *124*.

(96) Carey, J. J.; McKenna, K. P. Does Polaronic Self-Trapping Occur at Anatase TiO_2 Surfaces? *J. Phys. Chem. C* **2018**, *122*, 27540–27553.

(97) Rahimi, N.; Pax, R. A.; Gray, E. M. A. Review of Functional Titanium Oxides. I: TiO_2 and Its Modifications. *Prog. Solid State Chem.* **2016**, *44*, 86–105.

(98) Niu, M.; Tan, H.; Cheng, D.; Sun, Z.; Cao, D. Bandgap Engineering of Magnéli Phase Ti_nO_{2n-1}: Electron-Hole Self-Compensation. *J. Chem. Phys.* **2015**, *143*, 054701.

(99) Ho, Y. C.; Hoque, M. N. F.; Stoneham, E.; Warzywoda, J.; Dallas, T.; Fan, Z. Reduction of Oxygen Vacancy Related Traps in TiO_2 and the Impacts on Hybrid Perovskite Solar Cells. *J. Phys. Chem. C* **2017**, *121*, 23939–23946.

(100) Li, T.; Hong, F.; Yang, K.; Yue, B.; Tamura, N.; Wu, H.; Cheng, Z.; Wang, C. Metastable Oxygen Vacancy Ordering State and Improved Memristive Behavior in TiO_2 Crystals. *Sci. Bull.* **2020**, *65*, 631–639.

(101) Naldoni, A.; Allieta, M.; Santangelo, S.; Marelli, M.; Fabbri, F.; Cappelli, S.; Bianchi, C. L.; Psaro, R.; Dal Santo, V. Effect of Nature and Location of Defects on Bandgap Narrowing in Black TiO_2 Nanoparticles. *J. Am. Chem. Soc.* **2012**, *134*, 7600–7603.

(102) Nam, Y.; Li, L.; Lee, J. Y.; Prezhdo, O. V. Strong Influence of Oxygen Vacancy Location on Charge Carrier Losses in Reduced TiO_2 Nanoparticles. *J. Phys. Chem. Lett.* **2019**, *10*, 2676–2683.

(103) Sheng, X.; Chen, L.; Xu, T.; Zhu, K.; Feng, X. Understanding and Removing Surface States Limiting Charge Transport in TiO_2 Nanowire Arrays for Enhanced Optoelectronic Device Performance. *Chem. Sci.* **2016**, *7*, 1910–1913.

(104) Smith, J. R.; Walsh, F. C.; Clarke, R. L. Electrodes Based on Magnéli Phase Titanium Oxides: The Properties and Applications of Ebonex® Materials. *J. Appl. Electrochem.* **1998**, *28*, 1021–1033.

(105) Walsh, F. C.; Wills, R. G. A. The Continuing Development of Magnéli Phase Titanium Sub-Oxides and Ebonex® Electrodes. *Electrochim. Acta* **2010**, *55*, 6342–6351.

(106) Yan, J.; Wu, G.; Guan, N.; Li, L.; Li, Z.; Cao, X. Understanding the Effect of Surface/Bulk Defects on the Photocatalytic Activity of TiO_2: Anatase versus Rutile. *Phys. Chem. Chem. Phys.* **2013**, *15*, 10978–10988.

(107) Arif, A. F.; Balgis, R.; Ogi, T.; Iskandar, F.; Kinoshita, A.; Nakamura, K.; Okuyama, K. Highly Conductive Nano-Sized Magnéli Phases Titanium Oxide (TiO_X). *Sci. Rep.* **2017**, *7*, 1–9.

(108) Chen, X.; Liu, L.; Yu, P. Y.; Mao, S. S. Increasing Solar Absorption for Photocatalysis with Black Hydrogenated Titanium Dioxide Nanocrystals. *Science (80-.).* **2011**, *331*, 746–750.

(109) Elbanna, O.; Fujitsuka, M.; Kim, S.; Majima, T. Charge Carrier Dynamics in TiO_2 Mesocrystals with Oxygen Vacancies for Photocatalytic Hydrogen Generation under Solar Light Irradiation. *J. Phys. Chem. C* **2018**, *122*, 15163–15170.

(110) Han, W. Q.; Zhang, Y. Magńli Phases Ti_nO_{2n-1} Nanowires: Formation, Optical, and Transport Properties. *Appl. Phys. Lett.* **2008**, *92*, 1–4.

(111) Su, J.; Zou, X.; Chen, J.-S. Self-Modification of Titanium Dioxide Materials by Ti^{3+} and/or Oxygen Vacancies: New Insights into Defect Chemistry of Metal

Oxides. *RSC Adv.* **2014**, *4*, 13979–13988.

(112) Deák, P.; Aradi, B.; Frauenheim, T. Quantitative Theory of the Oxygen Vacancy and Carrier Self-Trapping in Bulk TiO_2. *Phys. Rev. B - Condens. Matter Mater. Phys.* **2012**, *86*, 1–8.

(113) Choudhury, B.; Bayan, S.; Choudhury, A.; Chakraborty, P. Narrowing of Band Gap and Effective Charge Carrier Separation in Oxygen Deficient TiO_2 Nanotubes with Improved Visible Light Photocatalytic Activity. *J. Colloid Interface Sci.* **2016**, *465*, 1–10.

(114) Harada, S.; Tanaka, K.; Inui, H. Thermoelectric Properties and Crystallographic Shear Structures in Titanium Oxides of the Magnèli Phases. *J. Appl. Phys.* **2010**, *108*, 083703.

(115) Roh, B.; Macdonald, D. D. Effect of Oxygen Vacancies in Anodic Titanium Oxide Films on the Kinetics of the Oxygen Electrode Reaction. *Russ. J. Electrochem.* **2007**, *43*, 125–135.

(116) Kim, S.; Ko, K. C.; Lee, J. Y.; Illas, F. Single Oxygen Vacancies of $(TiO_2)_{35}$ as a Prototype Reduced Nanoparticle: Implication for Photocatalytic Activity. *Phys. Chem. Chem. Phys.* **2016**, *18*, 23755–23762.

(117) Lettieri, S.; Pavone, M.; Fioravanti, A.; Amato, L. S.; Maddalena, P. Charge Carrier Processes and Optical Properties in TiO_2 and TiO_2-Based Heterojunction Photocatalysts: A Review. *Materials (Basel).* **2021**, *14*.

(118) Chen, M.; Straatsma, T. P.; Dixon, D. A. Molecular and Dissociative Adsorption of Water on $(TiO2)_n$ Clusters, n = 1-4. *J. Phys. Chem. A* **2015**, *119*, 11406–11421.

(119) Wang, T.-H.; Fang, Z.; Gist, N. W.; Li, S.; Dixon, D. A.; Gole, J. L. Computational Study of the Hydrolysis Reactions of the Ground and First Excited Triplet States of Small TiO_2 Nanoclusters. *J. Phys. Chem. C* **2011**, *115*, 9344–9360.

(120) Harb, M.; Rabilloud, F.; Simon, D.; Rydlo, A.; Lecoultre, S.; Conus, F.; Rodrigues, V.; Félix, C. Optical Absorption of Small Silver Clusters: Ag_n, (N=4-22). *J. Chem. Phys.* **2008**, *129*.

(121) Berardo, E.; Kaplan, F.; Bhaskaran-Nair, K.; Shelton, W. A.; Van Setten, M. J.; Kowalski, K.; Zwijnenburg, M. A. Benchmarking the Fundamental Electronic Properties of Small TiO_2 Nanoclusters by GW and Coupled Cluster Theory Calculations. *J. Chem. Theory Comput.* **2017**, *13*, 3814–3828.

(122) Dai, B.; Deng, K.; Yang, J.; Zhu, Q. Excited States of the 3d Transition Metal Monoxides. *J. Chem. Phys.* **2003**, *118*, 9608–9613.

(123) Taylor, D. J.; Paterson, M. J. Calculations of the Low-Lying Excited States of the TiO_2 Molecule. *J. Chem. Phys.* **2010**, *133*.

(124) Fang, Z.; Both, J.; Li, S.; Yue, S.; Aprà, E.; Keçeli, M.; Wagner, A. F.; Dixon, D. A. Benchmark Calculations of Energetic Properties of Groups 4 and 6 Transition Metal Oxide Nanoclusters Including Comparison to Density Functional Theory. *J. Chem. Theory Comput.* **2016**, *12*, 3689–3710.

(125) Berardo, E.; Hu, H.-S.; Shevlin, S. A.; Woodley, S. M.; Kowalski, K.; Zwijnenburg, M. A. Modeling Excited States in TiO_2 Nanoparticles: On the Accuracy of a TD-DFT Based Description. *J. Chem. Theory Comput.* **2014**, *10*, 1189–1199.

(126) Chen, M.; Dixon, D. A. Modeling the Formation of TiO_2 Ultra-Small Nanoparticles. *Nanoscale* **2017**, *9*, 7143–7162.

(127) Garcia, J. M.; Heald, L. F.; Shaffer, R. E.; Sayres, S. G. Oscillation in Excited State Lifetimes with Size of Sub-Nanometer Neutral $(TiO_2)_n$ Clusters Observed with Ultrafast Pump-Probe Spectroscopy. *J. Phys. Chem. Lett.* **2021**, *12*, 4098–4103.

(128) Çakir, D.; Gülseren, O. Ab Initio Study of Neutral $(TiO_2)_n$ Clusters and Their Interactions with Water and Transition Metal Atoms. *J. Phys. Condens. Matter* **2012**, *24*, 13.

(129) Qu, Z. W.; Kroes, G. J. Theoretical Study of the Electronic Structure and Stability of Titanium Dioxide Clusters $(TiO_2)_n$ with n = 1-9. *J. Phys. Chem. B* **2006**, *110*, 8998–9007.

(130) Ganguly Neogi, S.; Chaudhury, P. Structural, Spectroscopic Aspects, and Electronic Properties of $(TiO_2)_n$ Clusters: A Study Based on the Use of Natural Algorithms in Association with Quantum Chemical Methods. *J. Comput. Chem.* **2014**, *35*, 51–61.

(131) Marom, N.; Kim, M.; Chelikowsky, J. R. Structure Selection Based on High Vertical Electron Affinity for TiO_2 Clusters. *Phys. Rev. Lett.* **2012**, *108*, 106801.

(132) Li, S.; Dixon, D. A. Molecular Structures and Energetics of the $(TiO_2)_n$ (n = 1-4) Clusters and Their Anions. *J. Phys. Chem. A* **2008**, *112*, 6646–6666.

(133) Lamiel-Garcia, O.; Cuko, A.; Calatayud, M.; Illas, F.; Bromley, S. T. Predicting Size-Dependent Emergence of Crystallinity in Nanomaterials: Titania Nanoclusters: Versus Nanocrystals. *Nanoscale* **2017**, *9*, 1049–1058.

(134) Calatayud, M.; Maldonado, L.; Minot, C. Reactivity of $(TiO_2)_n$ Clusters (n = 1-10): Probing Gas-Phase Acidity and Basicity Properties. *J. Phys. Chem. C* **2008**, *112*,

16087–16095.

(135) Weichman, M. L.; Song, X.; Fagiani, M. R.; Debnath, S.; Gewinner, S.; Schöllkopf, W.; Neumark, D. M.; Asmis, K. R. Gas Phase Vibrational Spectroscopy of Cold $(TiO_2)_n^-$ (n = 3-8) Clusters. *J. Chem. Phys.* **2016**, *144*, 124308.

(136) Jeong, K. S.; Chang, C.; Sedlmayr, E.; Sülzle, D. *Electronic Structure Investigation of Neutral Titanium Oxide Molecules Ti_xO_Y*; 2000; Vol. 33.

(137) Kasha, M. Characterization of Electronic Transitions in Complex Molecules. *Discuss. Faraday Soc.* **1950**, *9*, 14–19.

(138) Peach, M. J. G.; Benfield, P.; Helgaker, T.; Tozer, D. J. Excitation Energies in Density Functional Theory: An Evaluation and a Diagnostic Test. *J. Chem. Phys.* **2008**, *128*.

(139) Valero, R.; Morales-Garciá, Á.; Illas, F. Investigating the Character of Excited States in TiO_2 Nanoparticles from Topological Descriptors: Implications for Photocatalysis. *Phys. Chem. Chem. Phys.* **2020**, *22*, 3017–3029.

(140) Mewes, S. A.; Plasser, F.; Krylov, A.; Dreuw, A. Benchmarking Excited-State Calculations Using Exciton Properties. *J. Chem. Theory Comput.* **2018**, *14*, 710–725.

(141) Rana, T. H.; Kumar, P.; Solanki, A. K.; Skomski, R.; Kashyap, A. Ab-Initio Study of Free Standing TiO_2 Clusters: Stability and Magnetism. In *Journal of Applied Physics*; 2013; Vol. 113, pp 17–526.

(142) Çakir, D.; Gülseren, O. Ab Initio Study of Neutral $(TiO_2)_n$ Clusters and Their Interactions with Water and Transition Metal Atoms. *J. Phys. Condens. Matter* **2012**, *24*, 305301.

(143) Peng, W. T.; Fales, B. S.; Shu, Y.; Levine, B. G. Dynamics of Recombination: Via Conical Intersection in a Semiconductor Nanocrystal. *Chem. Sci.* **2018**, *9*, 681–687.

(144) Weichman, M. L.; Song, X.; Fagiani, M. R.; Debnath, S.; Gewinner, S.; Schöllkopf, W.; Neumark, D. M.; Asmis, K. R. Gas Phase Vibrational Spectroscopy of Cold $(TiO_2)_n^-$ (n = 3-8) Clusters. *J. Chem. Phys.* **2016**, *144*, 124308.

(145) Marom, N.; Kim, M.; Chelikowsky, J. R. Structure Selection Based on High Vertical Electron Affinity for TiO_2 Clusters. *Phys. Rev. Lett.* **2012**, *108*.

(146) Zhai, H. J.; Wang, L. S. Probing the Electronic Structure and Band Gap Evolution

of Titanium Oxide Clusters $(TiO_2)_n^-$ (n = 1-10) Using Photoelectron Spectroscopy. *J. Am. Chem. Soc.* **2007**, *129*, 3022–3026.

(147) Ganguly Neogi, S.; Chaudhury, P. Structural, Spectroscopic Aspects, and Electronic Properties of $(TiO_2)_n$ Clusters: A Study Based on the Use of Natural Algorithms in Association with Quantum Chemical Methods. *J. Comput. Chem.* **2014**, *35*, 51–61.

(148) Berardo, E.; Hu, H. S.; Van Dam, H. J. J.; Shevlin, S. A.; Woodley, S. M.; Kowalski, K.; Zwijnenburg, M. A. Describing Excited State Relaxation and Localization in TiO_2 Nanoparticles Using TD-DFT. *J. Chem. Theory Comput.* **2014**, *10*, 5538–5548.

(149) Li, S.; Dixon, D. A. Molecular Structures and Energetics of the $(ZrO_2)_n$ and $(HfO_2)_n$ (n = 1-4) Clusters and Their Anions. *J. Phys. Chem. A* **2010**, *114*, 2665–2683.

(150) Qu, Z.-W.; Kroes, G.-J. Theoretical Study of the Electronic Structure and Stability of Titanium Dioxide Clusters $(TiO_2)_n$ with n = 1-9. *J. Phys. Chem. B* **2006**, *110*, 8998–9007.

(151) Rana, T. H.; Kumar, P.; Solanki, A. K.; Skomski, R.; Kashyap, A. Ab-Initio Study of Free Standing TiO_2 Clusters: Stability and Magnetism. *J. Appl. Phys.* **2013**, *113*.

(152) Xiao, Y.; Jin, P.; Wang, G.; Zhang, L. New Insights into the Structural Evolution of TiO2-Ti_3O_5-Ti_2O_3-TiO-$Ti_xO_yC_z$-TiC Systems at the Nanoscale during the Reduction Process. *Phys. Chem. Chem. Phys.* **2021**, *23*, 4796–4804.

(153) Du, H.; Jia, Y.; Niu, C.; Hu, K.; Li, H.; Yu, L. The Ratio Law of the Structure Evolution and Stability for Ti_nO_m (n = 3–18, m = 1–2n) Clusters. *Chem. Phys. Lett.* **2019**, *731*, 136574.

(154) Dargouthi, S.; Boughdiri, S.; Tangour, B. Stabilizing of the Transitory Species $(TiO_2)_2$ by Encapsulation into Carbon Nanotubes. *Acta Chim. Slov.* **2015**, *62*, 445–451.

(155) Hao, Y. N.; Chen, T.; Zhang, X.; Zhou, H.; Ma, Y. Ti-Ti σ Bond at Oxygen Vacancy Inducing the Deep Defect Level in Anatase TiO_2 (101) Surface. *J. Chem. Phys.* **2019**, *150*, 1–9.

(156) Pyykkö, P.; Atsumi, M. Molecular Single-Bond Covalent Radii for Elements 1-118. *Chem. - A Eur. J.* **2009**, *15*, 186–197.

(157) Garcia, J. M.; Heald, L. F.; Shaffer, R. E.; Sayres, S. G. Oscillation in Excited State Lifetimes with Size of Sub-Nanometer Neutral $(TiO_2)_n$Clusters Observed with Ultrafast Pump-Probe Spectroscopy. *J. Phys. Chem. Lett.* **2021**, *12*, 4098–

4103.

(158) Foltin, M.; Stueber, G. J.; Bernstein, E. R. On the Growth Dynamics of Neutral Vanadium Oxide and Titanium Oxide Clusters. *J. Chem. Phys.* **1999**, *111*, 9577–9586.

(159) Wu, H.; Wang, L. S. Electronic Structure of Titanium Oxide Clusters: TiO_y (Y=1-3) and $(TiO_2)_n$ (N=1-4). *J. Chem. Phys.* **1997**, *107*, 8221–8228.

(160) Zhai, H.-J.; Wang, L.-S. Probing the Electronic Structure and Band Gap Evolution of Titanium Oxide Clusters $(TiO_2)_n$-(n = 1-10) Using Photoelectron Spectroscopy. **2007**.

(161) Serpone, N.; Lawless, D.; Khairutdinov, R. Size Effects on the Photophysical Properties of Colloidal Anatase TiO_2 Particles: Size Quantization or Direct Transitions in This Indirect Semiconductor? *J. Phys. Chem.* **1995**, *99*, 16646–16654.

(162) Monticone, S.; Tufeu, R.; Kanaev, A. .; Scolan, E.; Sanchez, C. Quantum Size Effect in TiO_2 Nanoparticles: Does It Exist? *Appl. Surf. Sci.* **2000**, *162–163*, 565–570.

(163) Setvin, M.; Franchini, C.; Hao, X.; Schmid, M.; Janotti, A.; Kaltak, M.; Van De Walle, C. G.; Kresse, G.; Diebold, U. Direct View at Excess Electrons in TiO_2 Rutile and Anatase. *Phys. Rev. Lett.* **2014**, *113*.

APPENDIX A

PERMISSION TO REPRODUCE PORTIONS OF CHAPTER 5

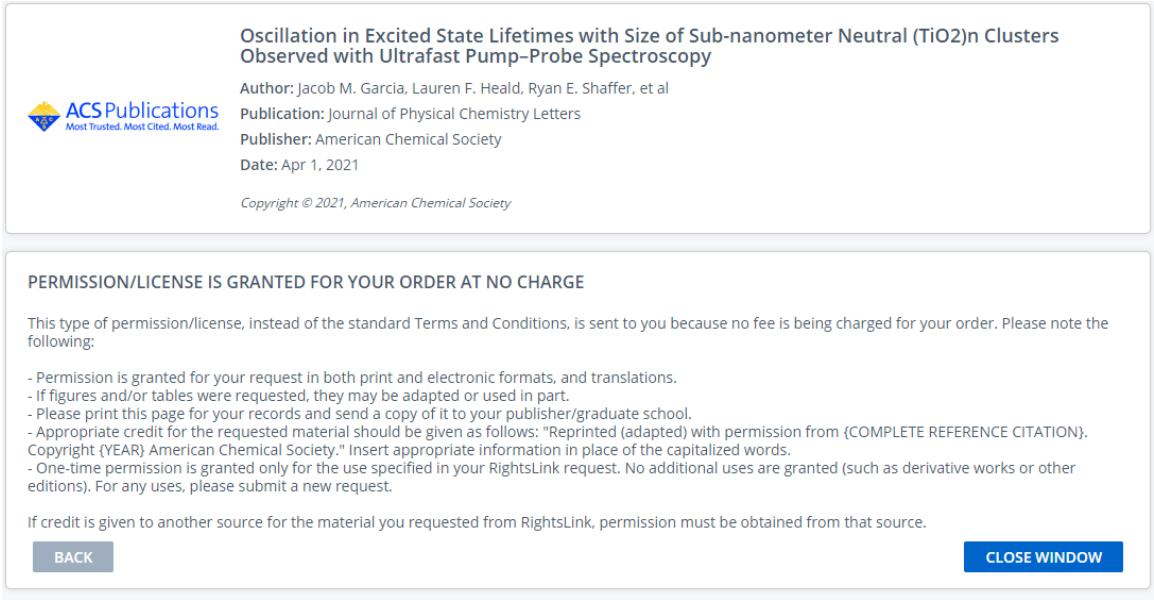

Authors do **not** need permission from AIP Publishing to:

- quote from a publication (please include the material in quotation marks and provide the customary acknowledgment of the source)
- reuse any materials that are licensed under a Creative Commons CC BY license (please format your credit line: “Author names, Journal Titles, Vol.#, Article ID#, Year of Publication; licensed under a Creative Commons Attribution (CC BY) license.”)
- reuse your own AIP Publishing article in your thesis or dissertation (please format your credit line: “Reproduced from [FULL CITATION], with the permission of AIP Publishing”)

American Chemical Society's Policy on Theses and Dissertations

This policy addresses permission to include **your article**(s) or portions of text from **your article**(s) in your thesis.

Reuse/Republication of the Entire Work in Theses or Collections: Authors may reuse all or part of the Submitted, Accepted or Published Work in a thesis or dissertation that the author writes and is required to submit to satisfy the criteria of degree-granting institutions. Such reuse is permitted subject to the ACS' "Ethical Guidelines to Publication of Chemical Research". Appropriate citation of the Published Work must be made as follows

"Reprinted with permission from [COMPLETE REFERENCE CITATION]. Copyright [YEAR] American Chemical Society." Insert the appropriate wording in place of the capitalized words. Citation information may be found after the "Cite this:" heading below the title of the online version and at the bottom of **the first page of the pdf or print version of your ACS journal article**.

If the thesis or dissertation to be published is in electronic format, a direct link to the Published Work must also be included using the ACS Articles on Request author-directed link.

All corresponding authors of previously published works in Chapter 5 have authorized publication in this dissertation.